Title

Developing Computational Optical Imaging Systems with Artificial Intelligence

Author

Du, Xiaoxi

Publication Date

2024

Peer reviewed|Thesis/dissertation

UNIVERSITY OF CALIFORNIA

Los Angeles

Developing Computational Optical Imaging Systems with Artificial Intelligence

A dissertation submitted in partial satisfaction of the

requirements for the degree Doctor of Philosophy

in Bioengineering

by

Xiaoxi Du

2024

ABSTRACT OF THE DISSERTATION

Developing Computational Optical Imaging

Systems with Artificial Intelligence

by

Xiaoxi Du

Doctor of Philosophy in Bioengineering

University of California, Los Angeles, 2024

Professor Liang Gao, Chair

Alzheimer's disease (AD) is a major risk for the aging population. The pathological hallmarks of AD—an abnormal deposition of amyloid β-protein (Aβ) and phosphorylated tau (pTau)—have been demonstrated in the retinas of AD patients, including in prodromal patients with mild cognitive impairment (MCI). Aβ pathology, especially the accumulation of the amyloidogenic 42-residue long alloform ($A\beta_{42}$), is considered an early and specific sign of AD, and together with tauopathy, confirms AD diagnosis. To visualize retinal Aβ and pTau, state-of-the-art methods use fluorescence. However, administering contrast agents complicates the imaging procedure. To address this problem from fundamentals, this dissertation performed ex vivo studies to develop a

label-free hyperspectral imaging method to detect the spectral signatures of $A\beta_{42}$ and pS396-Tau. A deep learning framework was developed to predict their abundance in retinal cross-sections and transform a label-free HSI image to either a DAB or an immunofluorescent stained image in high accuracy. For the first time, we reported the spectral signature of pTau and provided a direct validation through immunostaining.

For small incision in vivo imaging, optical endoscopes are mostly limited by two-dimensional views or very small number of three-dimensional (3D) views of pathological sites, and are intrinsically low in resolution caused by the limited fiber cores. The dissertation demonstrated a flexible light field endoscopy (Flex- LFE) imaging system capable of capturing depth information in a single shot. To address the resolution challenges inherent in endoscopic imaging, an AI-powered super-resolution pipeline is developed to enhance the quality of reconstructed images.

Additionally, this work explored the utilization of tunable image-mapping optical coherence tomography (TIM-OCT) to further advance in imaging of the retina. While most current OCT devices require extensive scanning, by combining phase-only spatial light modulators with spectral domain OCT, TIM-OCT achieves tailored imaging performance and enables “eye motion freeze” snapshot imaging. Computational spectroscopic analysis is discussed to extract spectral signatures.

This dissertation demonstrates the potential of AI-driven optical imaging systems in addressing critical challenges in biomedical imaging, with a particular focus on the early detection of AD. The findings are expected to lay the groundwork for label-free detection of AD.

The dissertation of Xiaoxi Du is approved.

Jun Chen

Debiao Li

Tzung Hsiai

Liang Gao, Committee Chair

University of California, Los Angeles

2024

In loving memory of my grandfather

Table of Contents

List of Tables

List of Figures

List of Appendices

Acknowledgements

First and foremost, I would like to express my deepest appreciation to my supervisor, Professor Liang Gao, for his exceptional mentorship and unwavering support throughout my academic journey. I have been fortunate to be among his very first graduate students, work alongside him from UIUC to UCLA. When I first joined the iOptics Lab, I had little experience in the field of optics, but I was drawn to it by the precision and rigor inherent in optical systems. I'm deeply touched by Liang's enthusiasm for pursuing meaningful research and his passion for teaching in class. He has always been a constant source of inspiration to me.

I extend my sincere appreciation to the insightful guidance and feedback of my committee members, Professor Tzung Hsiai, Professor Debiao Li, and Professor Jun Chen, whose expertise greatly shaped the direction of this thesis. I am also deeply grateful to my collaborators Professor Maya Koronyo-Hamaou and Yosef Koronyo, whose contributions were crucial to the work presented in Chapter 2. I am also grateful for the opportunity to work with my incredibly talented lab mates. I would also like to thank my undergraduate supervisor, Dr. Chunhui Li, for her encouragement and advice during the early stages of my research.

I'm deeply grateful to Haoyu, Shuyan, and Haiwen, who were my roommates when I first moved to Los Angeles during the challenging pandemic period back in 2020. At a time when I knew no one in the city, they provided not only companionship but also a sense of warmth and belonging. Living together in that apartment created a truly memorable and supportive chapter of my life, for which I will always be thankful.

To my grandparents, who raised me with endless love and shaped my values, I owe a debt of gratitude. Their roles as professors made them my first teachers and the ones who sparked my

academic curiosity. To my parents, I am deeply thankful for granting me the freedom to explore and develop my passions.

To my friends —Zhiwei Wang, Qianhui Ma, Meiqi Liu, Zheng Lu, and Sirui Xie— for your constant encouragement and support for me through the up and downs.

I also wish to acknowledge the strength and resilience I found within myself, particularly in overcoming the physical and emotional pain of an accident injury. This journey has taught me the importance of perseverance and self-belief.

I am grateful for my funding support from the National Institutes of Health (NIH), National Eye Institute, National Science Foundation (NSF), and the USC-ADRC Neuropathology Core and Dr. Carol Miller, MD, for providing access to human donor tissues.

Reflecting on the generosity of inspiration and support I have received throughout this journey, I am reminded that the most meaningful way to repay it is by holding a high standard of integrity and excellence in my work. When my time comes, I aspire to create a nurturing and encouraging environment for the next generation of young minds, just as I have been fortunate enough to experience.

Vita

EDUCATION

Master of Engineering (with Distinction)

University of Melbourne 2017-2018

Melbourne, Australia

Bachelor of Engineering

Northeastern University 2012-2016

Shenyang, China

CURRENT PUBLISHED MATERIALS

- Du X, Park J, Zhao R, Smith RT, Koronyo Y, Koronyo-Hamaoui M, Gao L (2024) Hyperspectral retinal imaging in Alzheimer's disease and age-related macular degeneration: a review. Acta Neuropathol Commun 12:157.
- Lee J, ***Du X**, Park J, Cui Q, Iyer RR, Boppart SA, Gao L (2023) Tunable image-mapping optical coherence tomography. Biomed Opt Express 14:627–638.
- Du X, Koronyo Y, Mirzaei N, Yang C, Fuchs DT, Black KL, Koronyo-Hamaoui M, Gao L (2022) Label-free hyperspectral imaging and deep-learning prediction of retinal amyloid β-protein and phosphorylated tau. PNAS Nexus 1:pgac164.
- Du X, Koronyo Y, Yang C, Koronyo-Hamaoui M, Gao L (2022) Label-Free Hyperspectral Imaging and Deep-Learning Prediction of Retinal Amyloid β-Protein and Phosphorylated Tau. In Computation and Machine Learning. IEEE Photonics Conference (IPC). pp 1–3.

- Du X, Zhu S, Gao L (2021) Super-Resolution Fiber-Bundle Light Field Endoscopy. In Endoscopy and Optical Biopsy (pp. DTh1A-3). Biophotonics Congress. Optica Publishing Group.
- Sun Y, You S, **Du X**, Spaulding A, George Liu Z, Chaney EJ, Spillman DR, Marjanovic M, Tu H, Boppart SA (2020) Real-time three-dimensional histology-like imaging by label-free nonlinear optical microscopy. Quant Imaging Med Surg 10:2177190–2172190.
- Hung ALY, Zheng H, Zhao K, **Du X**, Pang K, Miao Q, Raman SS, Terzopoulos D, Sung K (2024) CSAM: A 2.5D Cross-Slice Attention Module for Anisotropic Volumetric Medical Image Segmentation. 5923–5932.

***Co-first authorship**

Chapter 1 Introduction

Optical imaging offers several distinct advantages over other biomedical imaging techniques, making it a versatile and powerful tool in medical diagnostics and research. One of its foremost strengths lies in its high spatial and temporal resolution, enabling precise visualization of cellular and subcellular structures in real time. Compared to modalities such as X-ray computed tomography or magnetic resonance imaging (MRI), optical imaging uses non-ionizing radiation, is cost-effective in devices and excels in portability. Optical imaging techniques, like fluorescence imaging, provide remarkable molecular specificity, allowing for the non-invasive study of dynamic biological processes at the molecular and cellular levels in vivo. More important, optical imaging complements other imaging modalities, such as MRI or ultrasound, through multimodal approaches, providing a synergistic framework that enhances both functional and structural imaging. Therefore, optical imaging has a transformative role in advancing biomedical modalities and improving diagnostic accuracy.

Despite its profound impact, traditional optical imaging systems have been limited by physical constraints such as resolution and depth of field. However, advancements in computational techniques and the integration of artificial intelligence (AI) have opened up new possibilities, allowing imaging systems to surpass these physical barriers and extract meaningful information from complex imaging data that is not directly observable.

This dissertation focuses on the development of advanced computational optical imaging systems that leverage AI, with the goal of designing next-generation imaging platforms capable of delivering high-sensitivity and high-resolution images in real time. The research work aims to

contribute to the rapid evolving field of computational optical imaging, while laying the foundation for future research.

1.1 Label-free imaging

In many cases, disease markers exhibit a visual appearance that closely resembles that of normal tissue, rendering conventional two-dimensional (2D) imaging techniques insufficient due to limited contrast. Fluorescence imaging provides increased visibility and high molecular specificity through addressing exogenous contrast agents. However, the reliance on such agents raises concerns regarding toxicity and limited biocompatibility, thereby restricting their use in many clinical applications. In response to these limitations, we proposed a hyperspectral imaging (HSI) platform capable of conducting label-free, high-resolution imaging to visualize disease markers with enhanced specificity. This approach offers a safer alternative for clinical and research applications.

Rather than measuring only light intensities at 2D spatial coordinates, HSI captures a wide range of wavelengths across spectrum, from visible light to the near infrared, for each pixel in an image. The acquired 3D hypercube (x, y, λ) containing both spatial and spectral information. The enriched spatio-spectral data enables the detailed analysis and classification of the chemical constituents of tissues without the need for fluorescence labeling. Furthermore, HSI image by virtue mitigates the influence of tissue autofluorescence.

In this dissertation, I focused on utilizing the hyperspectral imaging technique to identify and discover the unique spectral signatures of Aβ and pTau, the two primary hallmarks of Alzheimer's disease (AD). With the global population aging, AD is profoundly impacting millions of individuals and their families [1]. Previous studies have demonstrated that Aβ and pTau manifest

in retina at an early stage, preceding their accumulation in the brain[2], [3]. Noteworthily, this is the first report of the spectral signature of pTau. We expect our findings will lay the foundation for the label-free detection of AD at its the early stages through in vivo retina imaging by the characteristic spectral signatures associated with pathological changes.

Building on the validation of spectral signatures of Aβ and pTau in human retina cross-sections, I proposed another advanced imaging modality in this dissertation, tunable image-mapping optical coherence tomography (TIM-OCT), as a step toward in vivo retinal imaging. OCT, which utilizes low-coherence interferometry, generates high-resolution cross-sectional images of biological tissues in a non-invasive manner and is widely used in ophthalmology due to its depth-resolved imaging abilities. By integrating a phase-only spatial light modulator (SLM) with a full field spectral domain OCT system, TIM-OCT can provide tailored imaging performance for a given application. Its snapshot imaging modes make it particularly advantageous for dynamic assessments, enabling in vivo retinal imaging by effectively "freezing" eye motion. Moreover, by utilizing computational tools, the spectral signatures can be extracted through spectroscopic OCT analysis.

1.2 Artificial intelligence

The interpretation of optical imaging data is complicated by the nonlinear and heterogeneous nature of light-tissue interactions, requiring the use of sophisticated algorithms and computational models for accurate image reconstruction and quantitative analysis. Artificial intelligence has undergone a remarkable transformation over the past decade, revolutionizing numerous engineering processes through automation. This technological evolution has also catalyzed a surge

in its applications across various domains of scientific research, enabling advancements such as data analysis and predictive modeling.

Machine learning algorithms, particularly deep learning, have demonstrated unparalleled effectiveness in enhancing image reconstruction, and extracting features from noisy or incomplete datasets. The concept of AI first emerged in the mid-20th century; however, progress was hindered during its early years due to limitations in computational power and data availability, leading to intermittent periods of stagnation [4]. The resurgence of AI in the late 1990s and early 2000s was fueled by the advent of machine learning techniques and the increased availability of digital data. This progress culminated in the development of deep learning, which harnesses neural networks and advanced algorithms to process vast datasets with unprecedented accuracy.

In the field of medical imaging, traditional image processing algorithms exhibit very limited tolerance for image-to-image variations, usually requiring professionals to manually adjust parameters to achieve optimal results for different input images [5]. However, with the rapid advancements in AI, its application to medical image processing has become increasingly promising. Deep neural networks, in particular, offer the capability to learn complex imaging parameters directly from data, eliminating the need for manual tuning. Once successfully trained, a deep learning model can enable real-time enhancement of imaging results in optical imaging systems, a feature that is crucial for facilitating clinical examinations and supporting devices used in operating rooms.

In this dissertation, I demonstrate the effectiveness of deep learning based AI approach under two advanced optical imaging schemes: hyperspectral imaging and light field imaging. For hyperspectral imaging, I proposed a DL framework that trained to learn the high-dimensional spectral information of the imaged retina samples. This framework classifies pixels based on the

spectral signatures of Aβ and pTau, enabling the inference of the spatial distribution of AD hallmarks, resembling histopathological images in competitive level of detail and accuracy.

On the other hand, dissertation presents the design of a flexible endoscope based on light field imaging, which enables the computation of depth information from a single shot, thereby providing a comprehensive three-dimensional view of tissue lesion structures. Endoscopic imaging inherently faces limitations due to the constraints of its small imaging diameter, which needs a trade-off between the resolution of individual views and the number of views required to compute depth information. To address this challenge, I propose an image super-resolution pipeline powered by deep learning, aimed at enhancing the quality of reconstructed images. By leveraging the capabilities of AI, this super-resolution model seeks to overcome the hardware limitations of endoscopic system design, enabling high-resolution imaging while maintaining the compact and flexible form for clinical applications.

Chapter 2 Hyperspectral Retinal Imaging

We present a quantitative study on HSI of Aβ and pTau deposits in human retinal cross-sections from neuropathologically confirmed AD patients. For the first time, we identified the spectral signature of pTau and demonstrated an accurate prediction of amyloidogenic 42-residue long ($A\beta_{42}$) alloform and pS396-Tau deposits in the retina by utilizing a deep-learning (DL) approach. The $A\beta_{42}$ and pS396-Tau markers were selected due to their recognized role in AD pathogenesis. For validation, we compared HSI prediction results with peroxidase-based immunostaining (also referred to as DAB staining) and immunofluorescent staining on the same imaging sections, which are both gold standards in quantifying Aβ and pTau deposits in retinal tissues [6], [7], [8], [9]. By feeding the spatio-spectral features associated with $A\beta_{42}$ and pS396-Tau into a generative adversarial network (GAN), our method can transform a label-free HSI image to either a DAB or an immunofluorescent stained image with high fidelity. The work presented here is expected to be the foundation for using HSI for noninvasive early AD diagnosis.

2.1 Eye as the site for AD hallmark imaging

Alzheimer's disease (AD) and associated dementia are estimated to afflict 50 million people worldwide, a number projected to triple by 2050. This age-dependent epidemic is a major concern for the aging population, with an incidence that rises sharply after 65 years of age, affecting roughly 50% of individuals aged 85 and older [10]. While currently there is no cure, with early diagnosis, the progression of the disease may be slowed and the patient life style may be changed [11], [12].

Although AD has been historically perceived as a brain disorder, recent studies indicate that AD also manifests in the eye with mounting evidence of abnormalities in the retina, a sensory extension of the brain [2], [6], [13]. Particularly, the hallmark pathological signs of AD, amyloid β-protein (Aβ), and neurofibrillary tangles (NFTs) comprised of hyperphosphorylated (p)Tau protein, which have long been described in the brain, have also been identified in the retina [2], [14]. There is a growing number of reports that Aβ deposits and pTau were discovered in the retinas of AD patients at various stages, in stark contrast to non-AD controls [2], [6], [7], [8], [9], [15], [16], [17], [18], [19], [20]. As the only central nervous system (CNS) tissue not shielded by bone, the retina offers unique access to study pathological changes in the brain, noninvasively and with unprecedented high spatial resolution. The evidence of Aβ accumulation in the retina at early stages of AD [2], [9] and the accumulation of retinal NFT and pTau [6], [7], [8] lends credence to the notion of the eye as a site for presymptomatic stage imaging. Notably, Koronyo-Hamaoui group and other teams revealed that retinal Aβ plaques, Aβ oligomers, and pTau tangles in transgenic AD-model mice appear at the presymptomatic and early stage and prior to detection in the brain [2], [3], [21], [22]. Moreover, a correlation has been found between the severity of cerebral and retinal Aβ burden, in both in-vivo and ex-vivo examinations [6], [17], [23].

It has been reported that in about 30% of aged cognitively normal people there is accumulation of Aβ in the brain, as measured by positron emission tomography (PET)—amyloid imaging [6], [7], [23], [24]. These individuals are considered to be either resilient to disease process or in the preclinical stage of AD. Although some older individuals can show accumulation of Aβ, in mild cognitive impairment (MCI) and AD patients there are significantly higher accumulation, which means increased Aβ levels were specific to AD. Further, it is important to note that per the National Institute on Aging (NIA) and the Alzheimer's Association guidelines [25], the presence of brain

Aβ is a prerequisite for definitive AD diagnosis, which were shown to occur decades before the clinical stage of the disease.

Despite holding great promise for early diagnosis of AD, visualization of retinal Aβ and pTau deposits is nontrivial. Because Aβ and pTau deposits have a similar visual appearance to normal tissue, conventional fundus photography provides little contrast. To increase visibility, state-of-the-art methods use exogenous fluorophores, and they have visualized retinal Aβ and pTau deposits with a high resolution [2], [6], [12], [14], [19], [23], [24], [26], [27], [28], [29], [30], [31]. However, administrating contrast agents in humans complicates the imaging procedure, hindering its scalability for population screening. To date, only curcumin, a natural fluorochrome, has been tested and used in clinical trials to label retinal Aβ [6], [12], [23], [24], [27], whereas fluorophores used to visualize retinal pTau in vivo are more limited. Therefore, there is an unmet need to develop label-free, high-resolution imaging techniques to visualize retinal Aβ and pTau deposits for early AD screening and disease management.

2.2 Label-free hyperspectral imaging

Over the past decade, hyperspectral imaging (HSI) has been increasingly used in various medical applications, and it has shown promising results for detecting various cancers [32], [33], [34], [35], [36], [37], [38], [39], [40], diagnosis of cardiac [41], [42] and retinal diseases [43], [44], [45], and assessment of brain functions and activities [46], [47], [48]. The overall rationale of using HSI for medical imaging is that the tissue's endogenous optical properties, such as absorption and scattering, change during the progression of the disease, and the spectrum of light emitted from tissue carries quantitative diagnostic information about tissue pathology. Rather than measuring

only light intensities at a 2D grid, HSI captures a series of images at different wavelengths and forms a 3D datacube (x, y, λ) (x, y, spatial coordinates; λ, wavelength) also known as a hypercube. The rich spatio-spectral information obtained enables the classification of chemical constituents of the tissue without fluorescence labeling.

Four distinct strategies exist for acquiring this datacube, as illustrated in Figure 1. The first approach, point-scanning HSI, employs a linear detector array to simultaneously record spectral information (λ) while sequentially scanning across all spatial coordinates (x, y) to assemble the complete datacube. The second approach, line-scanning HSI, utilizes a 2D detector array to acquire one slice of the datacube (y, λ) at a time, requiring scanning in only one spatial axis (x) to complete the data acquisition. Both point- and line-scanning HSI imagers involve extensive scanning to capture large datacubes, leading to prolonged acquisition times and increased susceptibility to motion artifacts, particularly when imaging dynamic scenes.

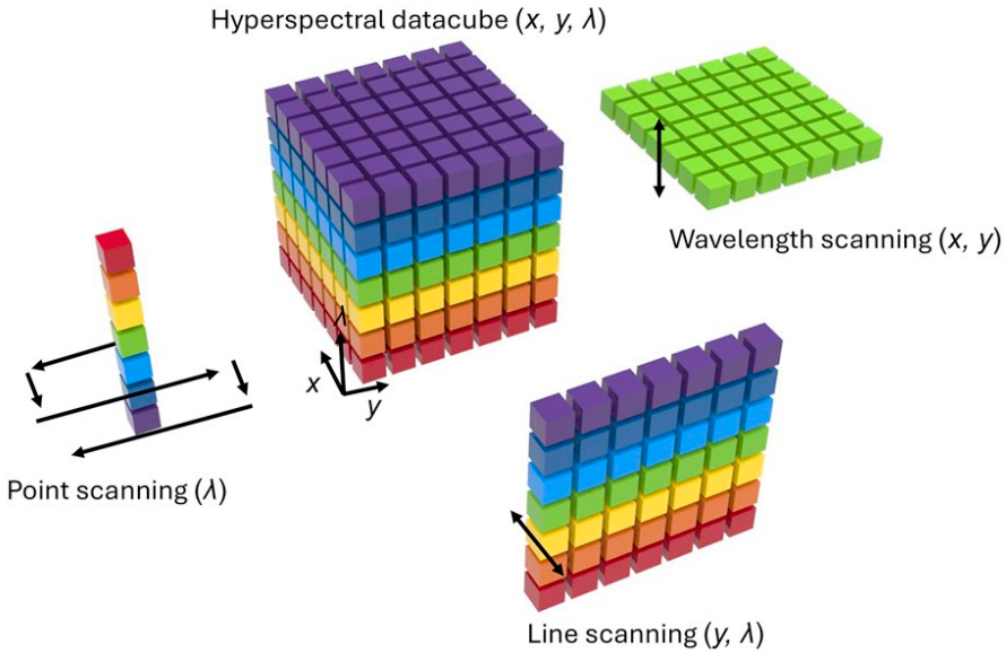

Figure 1. Hyperspectral datacube acquisition strategies.

In contrast, wavelength-scanning HSI, the third approach, captures one slice of the datacube (x, y) and then scans across all wavelengths (λ). This simultaneous acquisition of spatial information results in significantly faster imaging speeds compared to point- or line-scanning methods. Examples of systems using this strategy include acousto-optic or liquid crystal tunable filter- based HSI systems [49]. The fourth strategy, snapshot HSI, captures the entire datacube in a single exposure, offering a means to completely eliminate motion artifacts, especially when combined with flash illumination.

By virtue of its label-free imaging ability, several pioneer groups have explored HSI in examining the optical characteristics of Aβ in paired brain and retina tissues from both transgenic AD mouse models and human AD patients [20], [50], [51], [52], [53], [54], [55], [56]. It has been found that the effect of Aβ can be depicted by a characteristic light reflectance spectrum, and the magnitude of the spectrum varies with the AD development, in stark contrast to non-AD population where no evident differences are detected. However, the HSI experiments performed so far lack validation against fluorescence-staining ground truth images, and their methods are inadequate to reveal the precise locations and types of Aβ deposits on the retina. Moreover, despite being equally important in AD pathology, to our knowledge, the spectral signature of pTau and its label-free detection by HSI have not been reported.

We built an HSI system based on an Olympus IX83 microscope, the optical setup is shown in Figure 2. The sample is illuminated by a broadband halogen lamp, and the transmitted light is collected by a 10x objective lens (Olympus, 0.25 NA). The output image is filtered by a liquid crystal tunable filter (KURIOS-VB1, Thorlabs) in narrow bandwidth setting (10 nm FWHM at λ = 550 nm). The imaged spectral range is from 420 to 720 nm, with a scanning step in wavelength of 2 nm. We collected the image data using a monochrome sCMOS camera (CS2100M, Thorlabs).

In total, 151 spectral images were captured for one FOV. The entire cross-section of the retina superior-temporal strip was scanned with a 1/3 overlap between adjacent FOVs for image stitching. A sample not in imaging was attached to a glass slide without a cover glass and kept in PBS 1× solution. When performing imaging, we placed a cover glass on top of the sample and replenished it with PBS 1× solution to keep the tissue moist. All retinal cross-section samples were kept in PBS 1× solution over 2 weeks and reimaged multiple times. Upon completion of scanning, we stitched all the FOVs at the selected wavelength to a whole strip view of the retina cross-section.

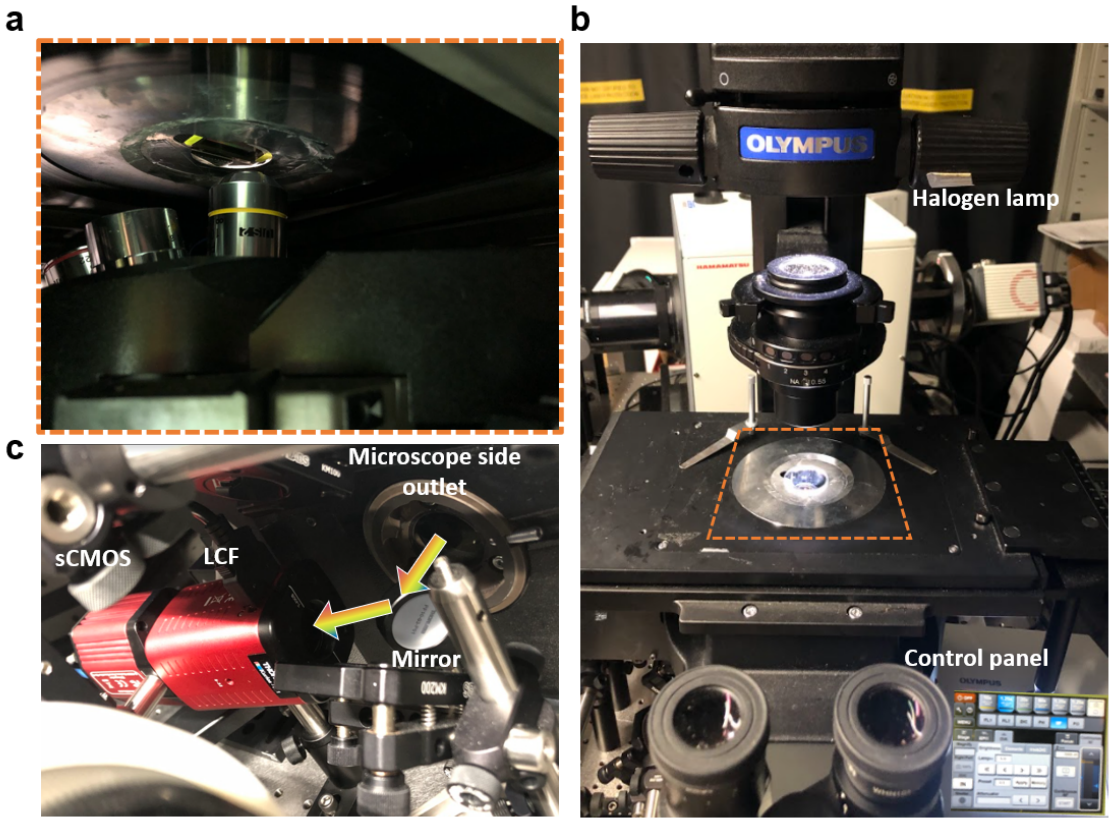

Figure 2. HSI system setup.

(a). Transmission imaging mode by a 10x objective. (b). The hyperspectral microscope sample stage and the control panel. (c). Side view of the outside optics.

Due to the sCMOS camera's varying spectral responses across different wavelengths, the acquired HSI data must be corrected to account for the system response. We used a benchmark fiber spectrometer (STS-VIS-L-25–400-SMA, Ocean Optics) to measure the lamp spectrum at the sample stage and imaged the slides with a blank FOV. The calibration coefficients for all the spectral components were obtained by dividing the average image intensities by measured spectral values. The calibration coefficients were fine-tuned by imaging a color checker (X-Rite Color Checker). The final calibration coefficients were saved and used in the following HSI data processing.

2.3 Spectral signatures of $A\beta_{42}$ and pS396-Tau

Using a custom HSI microscope equipped with a liquid crystal tunable filter, we imaged unstained postmortem retinal cross-sections from neuropathologically confirmed AD patients. The retina cross-sections were prepared undergone tissue isolation, processing, and sectioning from superior-temporal (ST) and inferior-temporal (IT) strips because previous studies show that both retinal Aβ and pTau are primarily distributed in peripheral superior and inferior retinal quadrants [2], [6], [8], [15].

The spectral signature of retinal tissue was examined in an average manner by area, consisting of a minimum of 3 pixels. Each set of raw HSI data contains 151 image slices. All the slices were read in and formed into a 3D datacube for efficient processing. The intensity at each spectral band was averaged over the selected area. Then the intensity values were calibrated using the measured calibration coefficients matrix. The overall intensity of the imaging spectral range was normalized.

To spot the deposit regions on the imaging slide, the most adjacent cross-section slide, (5 μm distance in z-direction) from the imaged one, was stained first as a guidance for HSI imaging. The corresponding marked areas were used for the spectral analysis to reveal the spectral signature of retinal $A\beta_{42}$ and pTau. Control regions were selected as regions from the immunostaining images with neither $A\beta_{42}$ nor pTau deposits and without cellular structures. We also randomly scanned across the retina tissue vertically and horizontally to locate characteristic areas and observed the distribution among all the spectra.

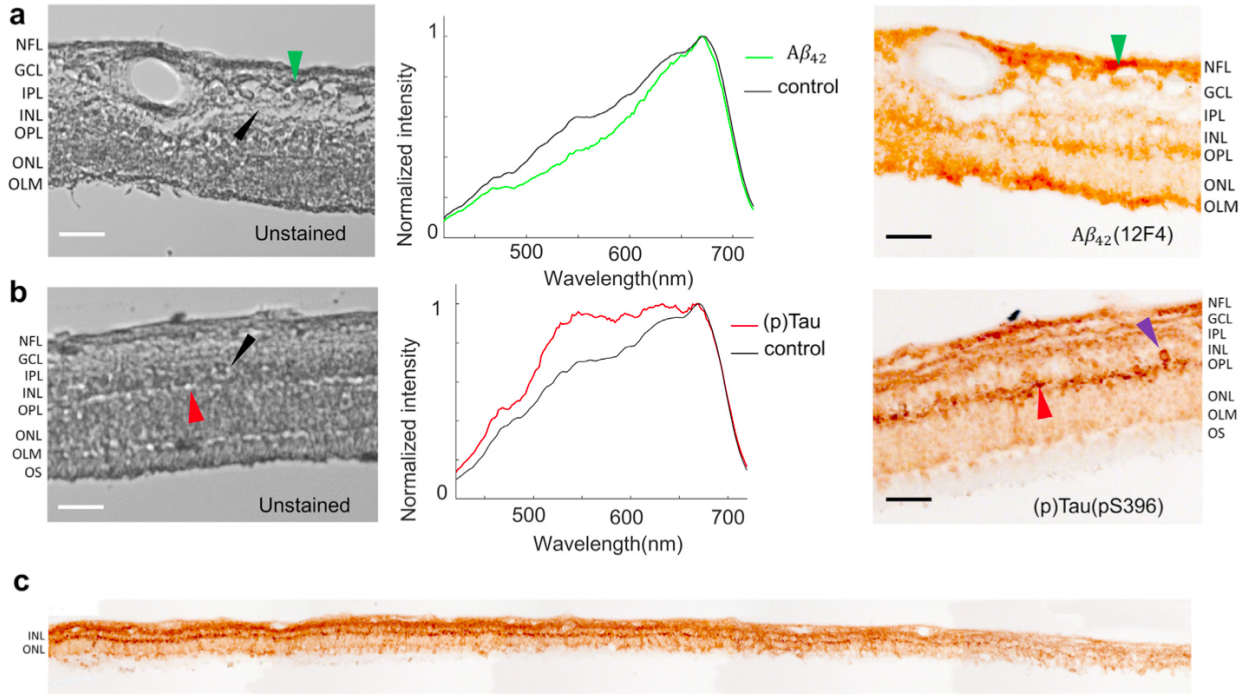

Figure 3. HSI of (a) $A\beta_{42}$ and (b) pS396-Tau deposits on postmortem retinal cross-sections of AD patients. (c). A tile image of a large portion of retinal cross-section strip.

From left to right, unstained hyperspectral intensity images, spectra at arrow-pointed locations (green for $A\beta_{42}$, red for pS396-Tau, and black for control), and DAB labeled images. The purple arrow is indicating an NFT-like or cellular structure (b, right) in the OPL. Scale bar, 50 μm.

The hypercubes obtained contain the spatio-spectral information of endogenous chromophores in the retinal tissues. To guide spectral profiling, we immunostained retinal cross-sections specifically against $A\beta_{42}$ and pS396-Tau and labeled either with peroxidase-based DAB substrate (3,3' diaminobenzidine; brown) or immunofluorescence and reimaged it under a brightfield or fluorescence microscope, respectively (Zeiss Axio Imager Z1). We further registered the unstained hyperspectral images with the immunolabeled DAB or fluorescently stained images and located the enriched areas of $A\beta_{42}$ and pS396-Tau in the hyperspectral images. The spectral signatures of retinal $A\beta_{42}$ and pS396-Tau were identified in those regions (Figures 3 and 4), where $A\beta_{42}$ and pS396-Tau exhibit distinct spectral profiles. In Figure 3, the Braak stages for patients are both V. The AD patient in Figure 3a is a female aged 90 with an Alzheimer's Disease Neuropathologic Change (ADNC) score of A2, B3, and C3 (A: Aβ plaque score, B: NFT stage, C: Neuritic plaque score). The AD patient in Figure 3b is a female aged 85 with an ADNC score of A3, B3, C3. Noteworthily, although the spectrum of $A\beta_{42}$ has been previously reported, this is the first time the spectrum of pS396-Tau is identified.

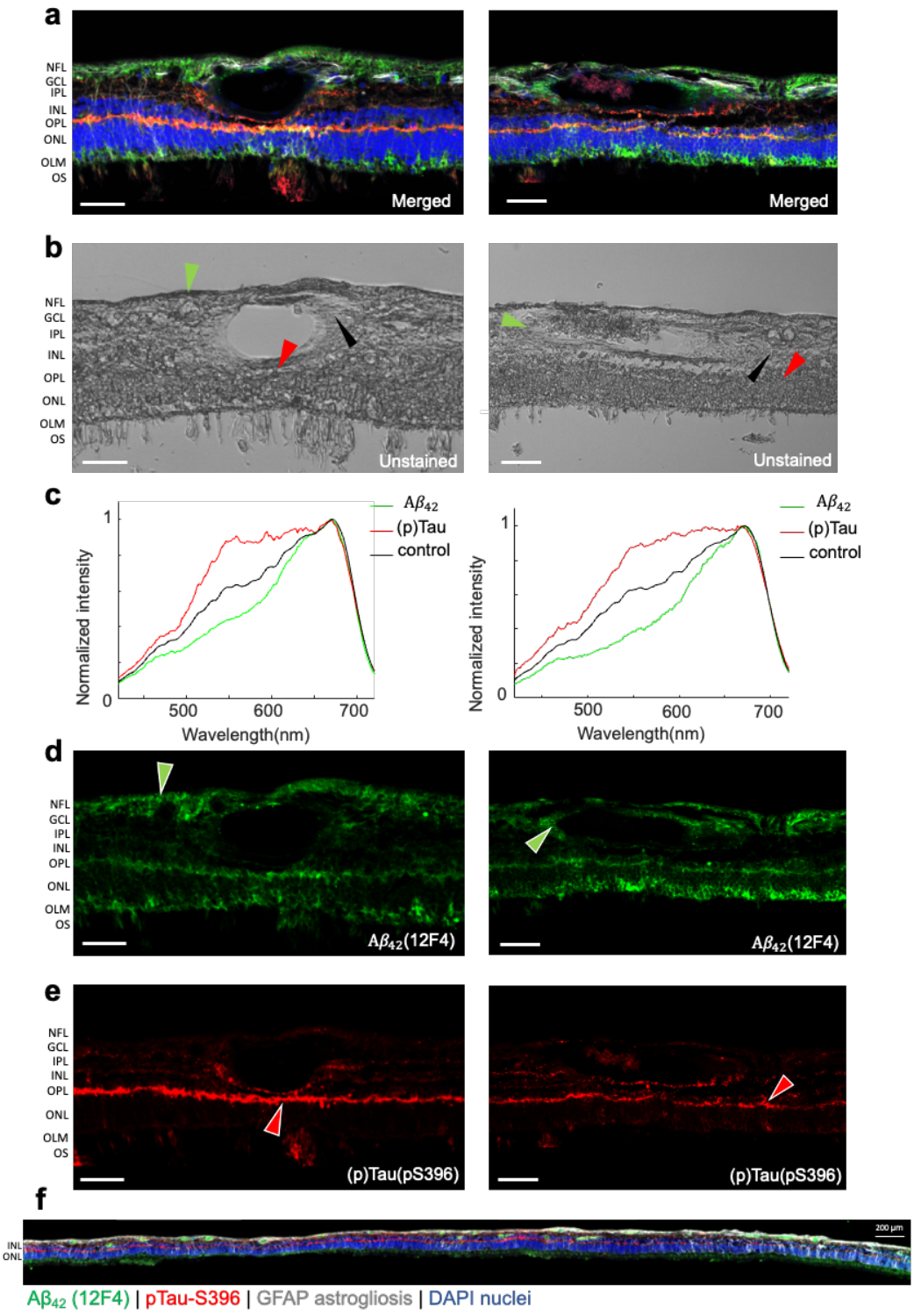

Figure 4. Hyperspectral imaging of Aβ$_{42}$ and pS396-Tau deposits on postmortem retinal cross sections of AD patients guided by immunofluorescence staining.

(a). Merged fluorescence images of four channels. (b). Unstained hyperspectral intensity images. (c). Spectral signatures of $A\beta_{42}$ and pS396-Tau in the human retina confirmed by combined fluorescence staining specific for $12F4^{+}$-$A\beta_{42}$ and pS396-Tau. (d). $A\beta_{42}$ channel. (e). pS396-Tau channel. (f). A tile image of a large portion of retinal cross-section strip from a confirmed AD patient (Female, Age: 90, Braak stage: V) immunolabeled with combination antibodies against $A\beta_{42}$ (green), pS396-Tau (red), and GFAP-astrocytes (white), and nuclei counterstained with DAPI (blue). Scale bar, 50 µm.

Consistent with previous studies [6], [14], the immunolabeling with DAB or immunofluorescence-stained images indicate that pTau mostly aggregates in the retinal outer plexiform layer (OPL), inner plexiform layer (IPL), and ganglion cell layer (GCL), and in structures that resemble NFTs (Figure 3b and 3c). Figure 5 is an illustration of the retina layers and the hallmarks aggregations. We also found pS396-Tau in the innermost retinal layers, along the nerve fiber layer (NFL), though it is variable from patient to patient and generally to a lesser extent (Figure 6).

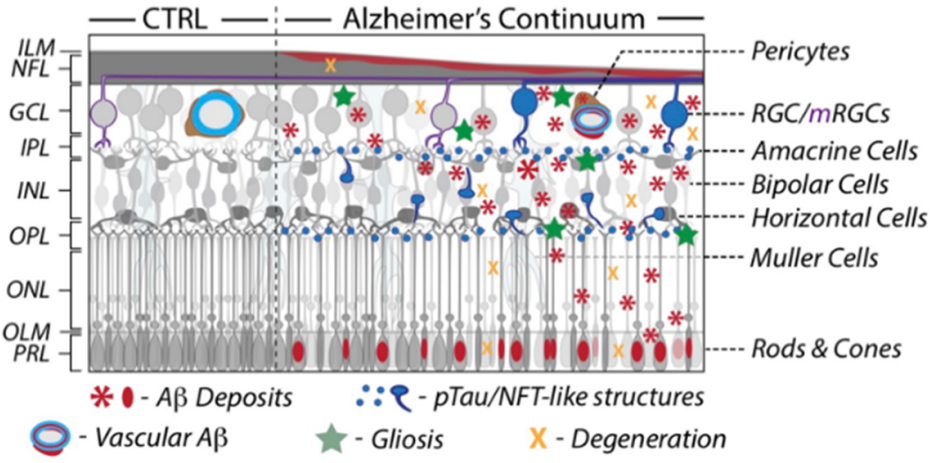

Figure 5. Schematic illustration of Alzheimer's pathology across retinal cell layers in AD patients.

CTRL, control. Adapted from [57]

We examined these locations in the unstained HSI images. Figure 3c shows the distribution of pS396-Tau deposit from the central to peripheral retina. The pS396-Tau clusters exhibit a unique spectral profile that significantly differs from that of "normal" retinal tissues—they have a much higher and uniform transmittance for light in the 550~650 nm range, resembling a "flat hat." This dominating feature indicates that pTau-enriched tissues have a reduced optical density in this spectral range, likely due to a smaller absorption coefficient of constituent chromophores. This prompted us to further examine the HSI images at these wavelengths. We found that the pTau aggregated in the OPL—which appears dark brown with DAB substrate and red in the immunofluorescence-stained images—correlates with higher pixel intensities in the grey-level HSI images (Figure 3b and 4).

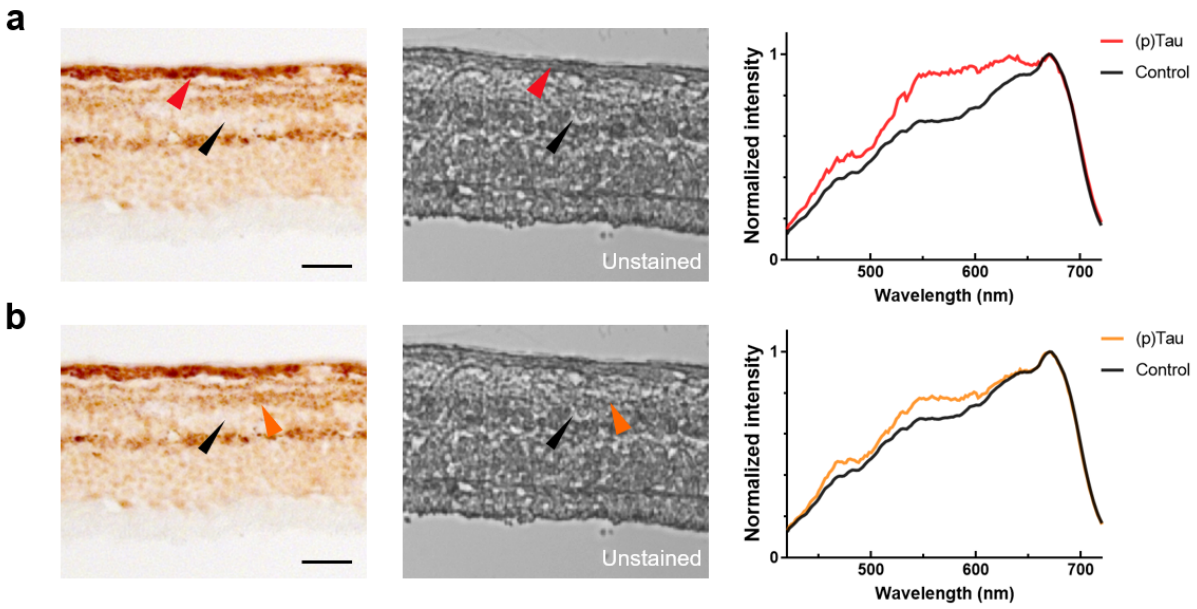

Figure 6. Hyperspectral imaging of various pS396-Tau deposits locations.

(a). pS396-Tau deposits at innermost retinal layers. (b). Diffusive pS396-Tau deposits in inner plexiform layer (IPL), forming three distinct bands. From left to right, DAB labeled pS396-Tau retinal cross-

sections, unstained hyperspectral intensity images, spectra at arrow-pointed locations. Black arrows: Control regions. Red and orange arrows: targeting pS396-Tau regions. Scale bar, 50 μm.

A similar correspondence has also been identified in the pS396-Tau aggregated region in the NFL (Figure 6a), corroborating our finding on the spectral transmission property of pTau. Notably, this is the first demonstration of pS396-Tau in human retina. Diffused pS396-Tau spectrum has the same characteristic with aggregated pS396-Tau but has reduced magnitude.

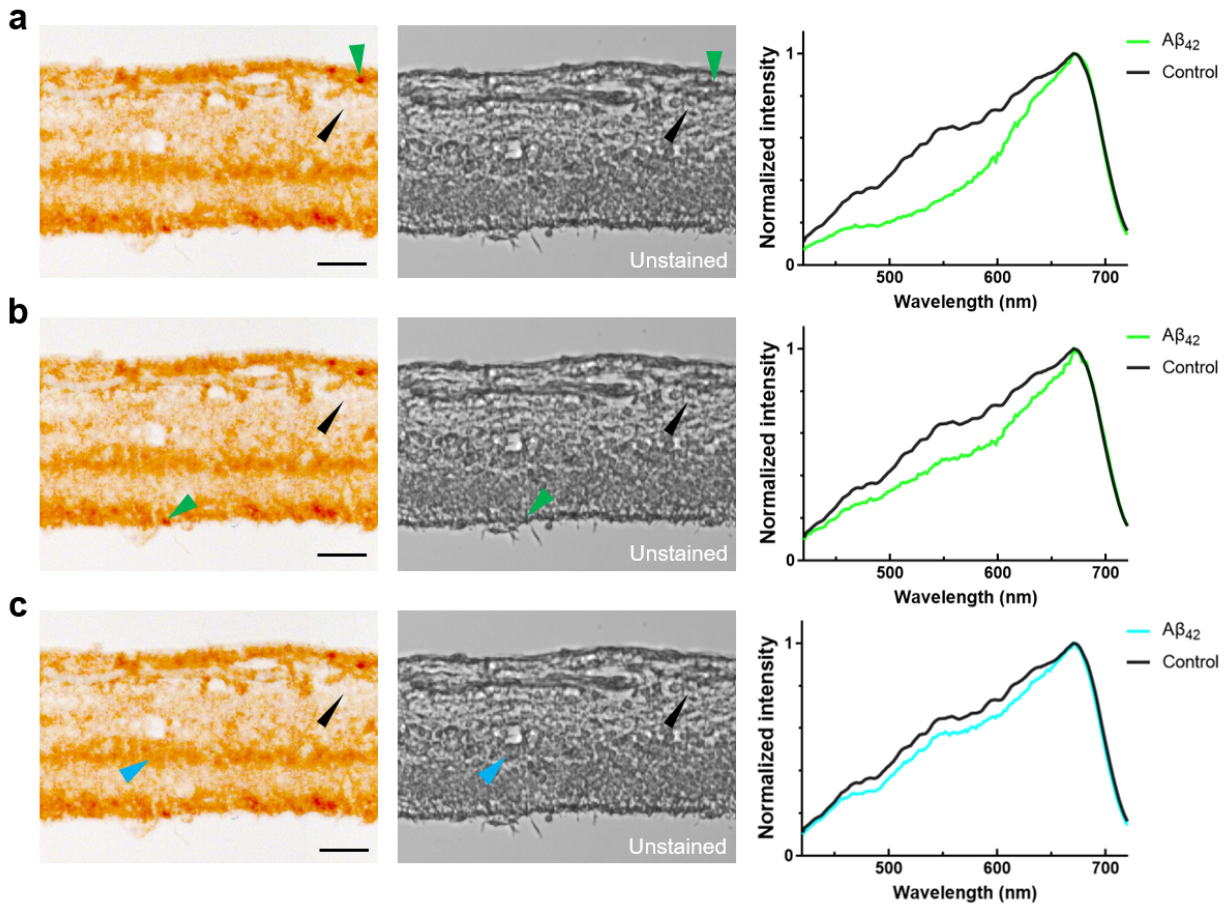

Figure 7. Hyperspectral imaging of various retinal $A\beta_{42}$ deposits and locations.

(a). $12F4^{+}$-$A\beta_{42}$ deposits at ganglion cell layer (GCL). (b). $A\beta_{42}$ deposits in photoreceptors. c. Diffusive $A\beta_{42}$ deposits in retinal OPL. From left to right, DAB-labeled $A\beta_{42}$ retina cross-sections, unstained

hyperspectral intensity images, spectra at arrow-pointed locations. Black arrows: Control regions. Green and Blue arrows: targeting $A\beta_{42}$ regions. Scale bar, 50 μm.

Besides the spectrum of pTau reported above, we also observed the known spectrum of Aβ. The DAB- or immunofluorescent-stained images show that specifically $12F4^{+}$-$A\beta_{42}$ is most abundant in the retinal NFL, GCL, OPL, and the outer nuclear layer (ONL; Figures 3a and 4a to d). Moreover, Figure 4f indicates that the important vascular $A\beta_{42}$ distribution is typical along the retinal cross-section strip. The spectra extracted at these locations in HSI images (Figures 3a and 4b) show a lower transmission in the 450 to 600 nm range, which were hypothesized to be caused by an elevated level of Rayleigh scattering in $A\beta_{42}$ enriched tissues [58]. We validated the consistency of the spectrum of $A\beta_{42}$ in across all retinal layers including within blood vessel walls (Figure 7 and 8). Noteworthily, although the spectral signature of retinal Aβ has been previously reported, this is the first time retinal $A\beta_{42}$ has been reported and quantified at locations verified by both fluorescence and non-fluorescence ground truth.

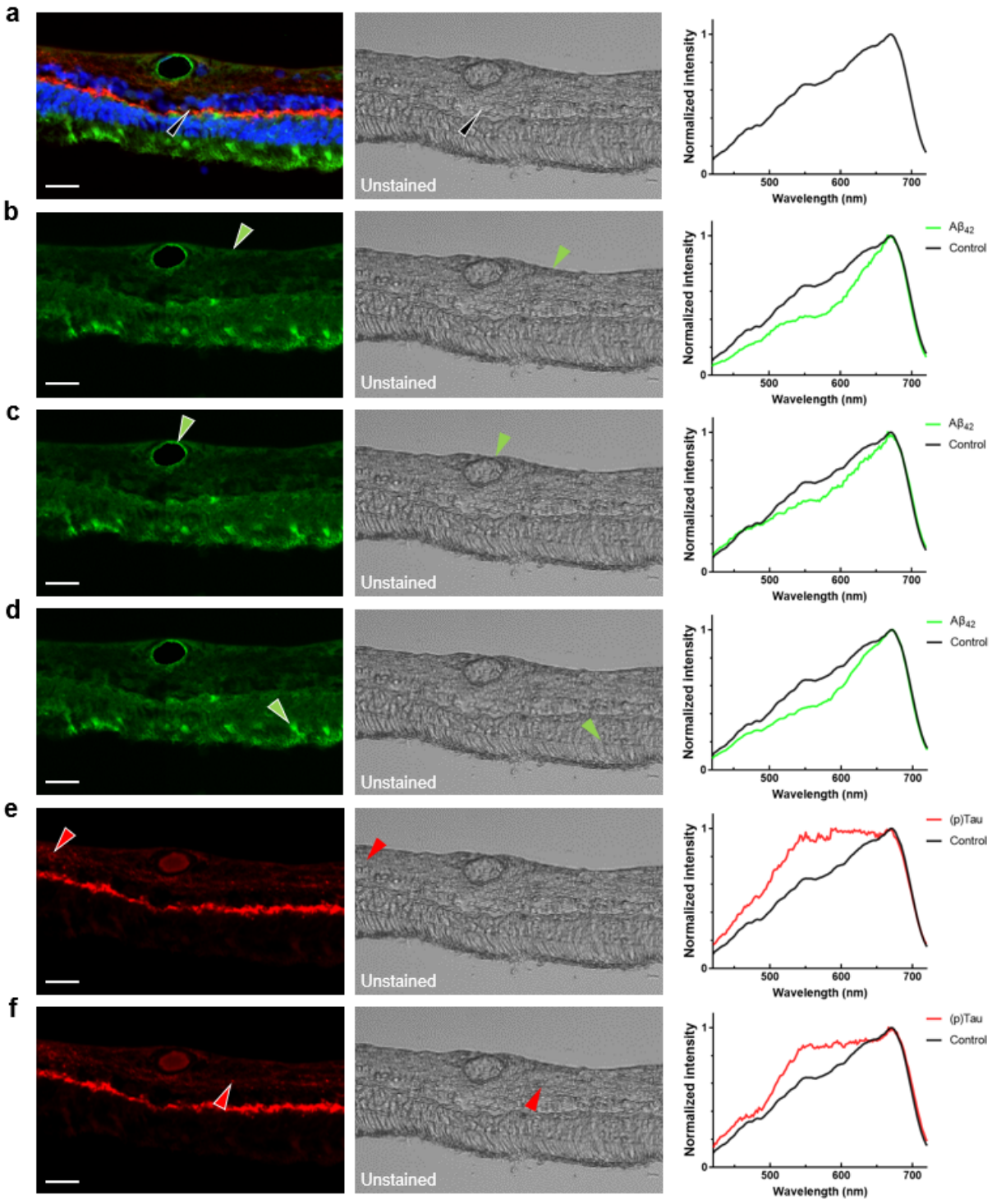

Figure 8. Hyperspectral imaging of various retinal $A\beta_{42}$ and pS396-Tau deposits and locations.

(a). Merged immunofluorescence-stained retinal cross-section image and corresponding HSI retinal image. A normal tissue region was selected as control for other $12F4^{+}$-$A\beta_{42}$ and pS396-Tau deposits analysis. (b). $A\beta_{42}$ channel, with arrow pointed at $A\beta_{42}$ deposits in nerve fiber layer (NFL). (c). $A\beta_{42}$ deposits in the vascular wall. (d). $A\beta_{42}$ deposits in photoreceptors. (e). pS396-Tau channel, with arrow pointed at pS396-Tau deposits in neurofibrillary tangle (NFT)-like structures in GCL. (f). pS396-Tau aggregated in the three distinct bands of IPL. From left to right, immunofluorescence-stained retinal cross-sections, unstained hyperspectral intensity images, spectra at arrow-pointed locations. Black arrows: control. Green and red arrows: targeting $A\beta_{42}$ and pS396-Tau regions, respectively. Scale bar, 50 μm.

The consistence of the HSI data was examined by reimaging the samples in an extended period of time (14 days). Analyzed regions were selected from mixed hypercubes captured on day 1 and day 14, and the averaged data are shown in Figure 9.

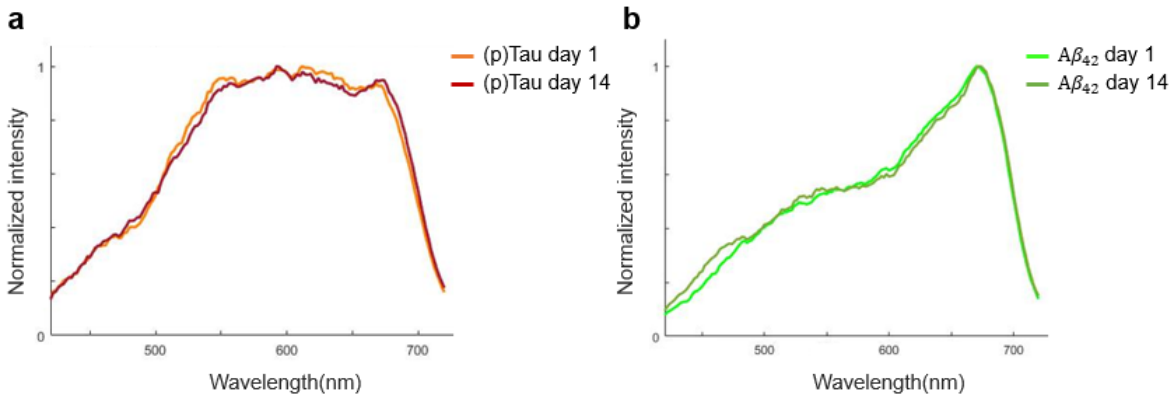

Figure 9. Spectra of (a) $A\beta_{42}$ and (b) pS396-Tau of the same sample measured on day 1 and day 14.

2.4 Image prediction by GAN

Using the spatio-spectral information in hypercubes, we can classify the HSI images and generate abundance maps of constituent components. The images so obtained can be further rendered to

resemble DAB and immunofluorescence staining using a pseudo-colormap. Among the state-of-the-art HSI classification approaches, deep learning is the most attractive option because it is robust against noise [59], [60]. Conventional deep learning methods classify HSI images pixel-wise solely based on the pixel's spectral information [61], [62]. However, this usually leads to unsatisfactory results due to the missing link to the spatial features. Later endeavors improve the model by classifying the images in patches, followed by mosaicking the resultant abundance maps [63], [64]. Nonetheless, the resultant classified images suffer from a low resolution, and it is challenging to form a histopathology-like image.

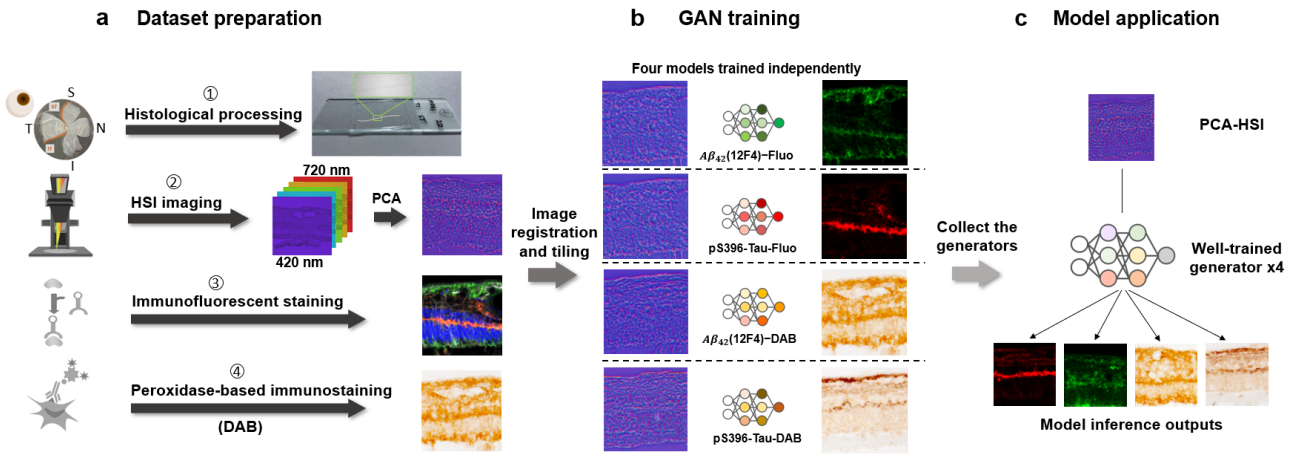

Figure 10. The deep learning workflow of $A\beta_{42}$ and pS396-Tau deposits prediction.

(a). 1. The process of retina cross-sections preparation. 2. The retina cross-sections are imaged by our HSI microscope before immunostaining. Raw data are normalized and go through PCA process to convert to RGB images. 3 and 4 are two different staining techniques used for comparison of the HSI analysis. (b). HSI images are registered with fluorescence and DAB staining images. Corresponding images form training pairs for the generative adversarial network. (c). The ROI patches are fed into the trained model to get the inference patches for $A\beta_{42}$ and pS396-Tau with different immune contrasts.

To solve these problems, we adapted a generative adversarial network (GAN) for HSI classification of Aβ and pTau and image transformation. GAN is a competitive network consisting of a generator and a discriminator. The discriminator network is trained to classify the real inputs and the fake inputs generated by the generator network. This adversarial training increases the generalization capability of the discriminator, and it is particularly effective when the training dataset is limited.

For HSI classification, it is important to combine the complex spectral information of every pixel with the neighboring pixels' information in a considerably efficient way. Most spatio-spectral-based classification methods use only a small neighboring region to construct a spatio-spectral vector [65], [66], [67]. Although this can improve the classification accuracy than extracting only spectral information, the classification accuracy is limited by the size of the selected region. In contrast, the GAN network in our method considers the spatio-spectral features in the entire region imaged to assign a value for each pixel.

We developed a workflow to transform unstained human retinal cross-sections into two types of standard histopathology images, which are immunofluorescence DAB contrast (Figure 10). We first convert an acquired hypercube (x, y, λ) to a three-channel image by principal component analysis (PCA) to represent the significant spectral differences of the imaged pixels. This significantly reduces the data load for training while preserving most of the variability (>85%) in the original hypercube. We then pair this extracted three-channel HSI image patch with the corresponding histopathology image and pass this image pair to the adapted GAN network for training. After training, we have four models for $A\beta_{42}$ and pS396-Tau with two staining contrasts.

The transformed histopathology-like images are output from the models and stitched to form a meaningful ROI.

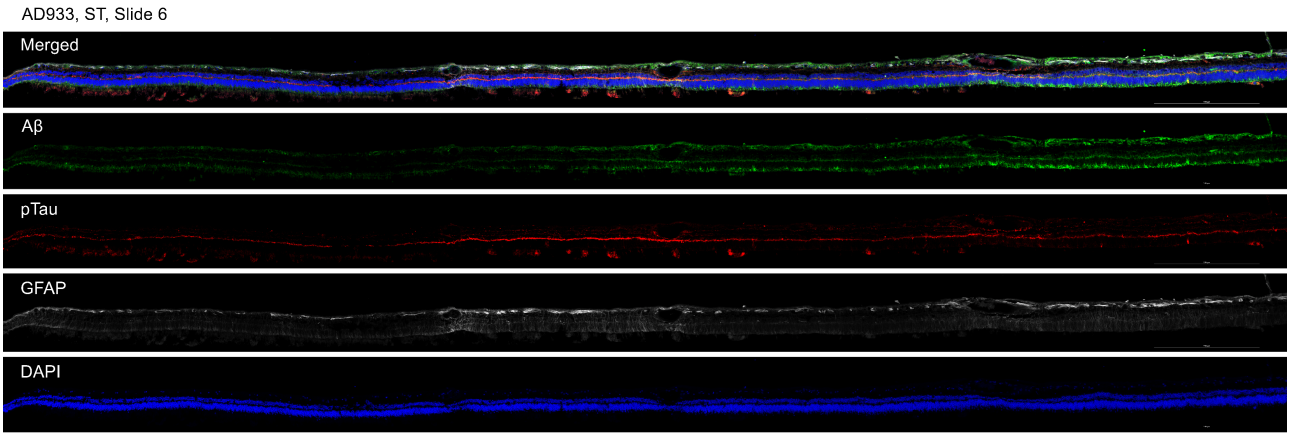

Figure 11. Immunofluorescence channels of stained whole retina cross-section.

In immunofluorescent image transformation, we employed the green and red channels of the merged fluorescent images in Figure 11 as the ground truth for $A\beta_{42}$ and pS396-Tau classification. In $A\beta_{42}$ and pS396-Tau immunofluorescence stained (Cy5, green and Cy3, red pseudo colors, respectively) images, there were distinct signals for each marker and no autofluorescence signal in the lumen of blood vessels. Although, autofluorescence signals were occasionally found at the blood vessel lumen (Figure 4f). Such signals will mislead the network training and prevent the true $A\beta_{42}$ and pS396-Tau signals from forming proper contrast in the analyzed region. To solve this issue, we removed the lumen signals by labeling them as negative and enhanced the contrast of true $A\beta_{42}$ and pS396-Tau signals. The models were trained by feeding green and red fluorescence data separately. The transformed immunofluorescent image patches of $A\beta_{42}$ and pS396-Tau were stitched to a larger field-of-view (FOV) and shown in Figure 12a and 12b, respectively.

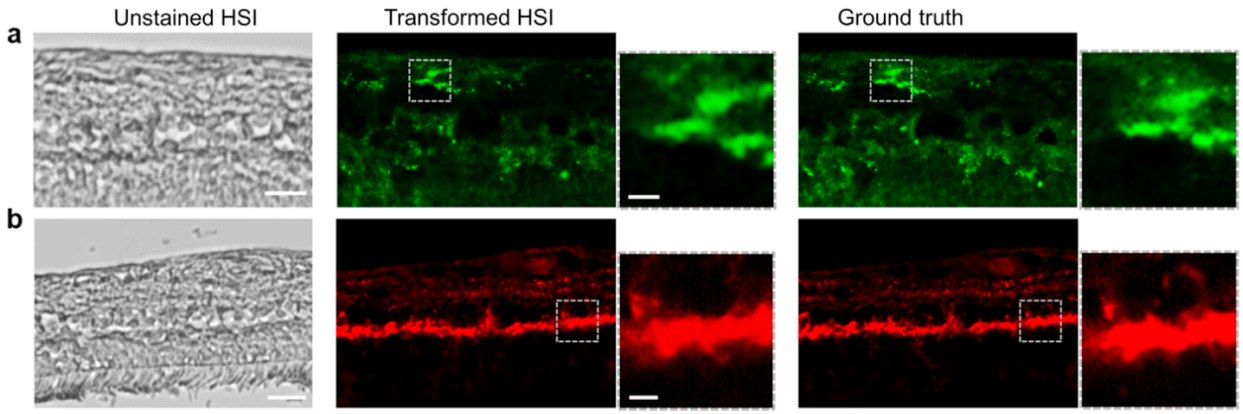

Figure 12. Stitched ROIs of the trained GAN models output.

(a). $A\beta_{42}$ fluorescence model. (b). pS396-Tau fluorescence model. Scale bar, 50 µm for large FOV images, 10 µm for bordered zoomed inserts.

In the zoomed insets, the predicted distributions of two AD-hallmark proteins in the region of interest match well with the ground truth. The Figure 13 shows the vascular wall $A\beta_{42}$ deposit prediction with a negatively labeled lumen, and the Figure 14 shows various pS396-Tau deposits. In general, using immunofluorescence-stained image as the ground truth yields an accurate prediction for $A\beta_{42}$ and pS396-Tau deposit distribution. The specific signals in the actual histopathology image can also be identified in the transformed image. For instance, we found correspondence in the ground truth image for both the recovered $A\beta_{42}$ signal pattern in Figure 12a and the transformed pS396-Tau in OPL image in Figure 12b.

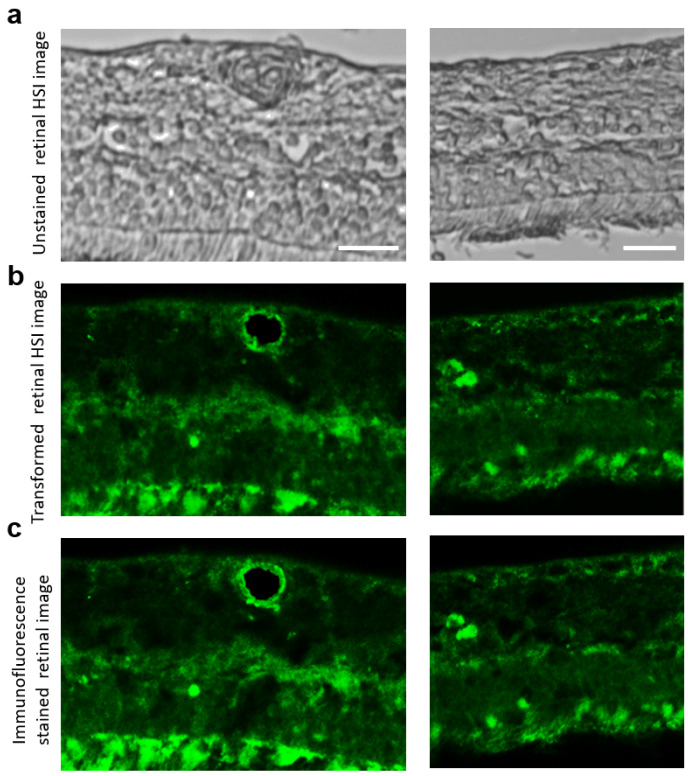

Figure 13. Histopathology prediction of hyperspectral images with the immunofluorescence-Aβ_{42} model.

Left and right columns: two different FOVs. Scale bar, 50 μm.

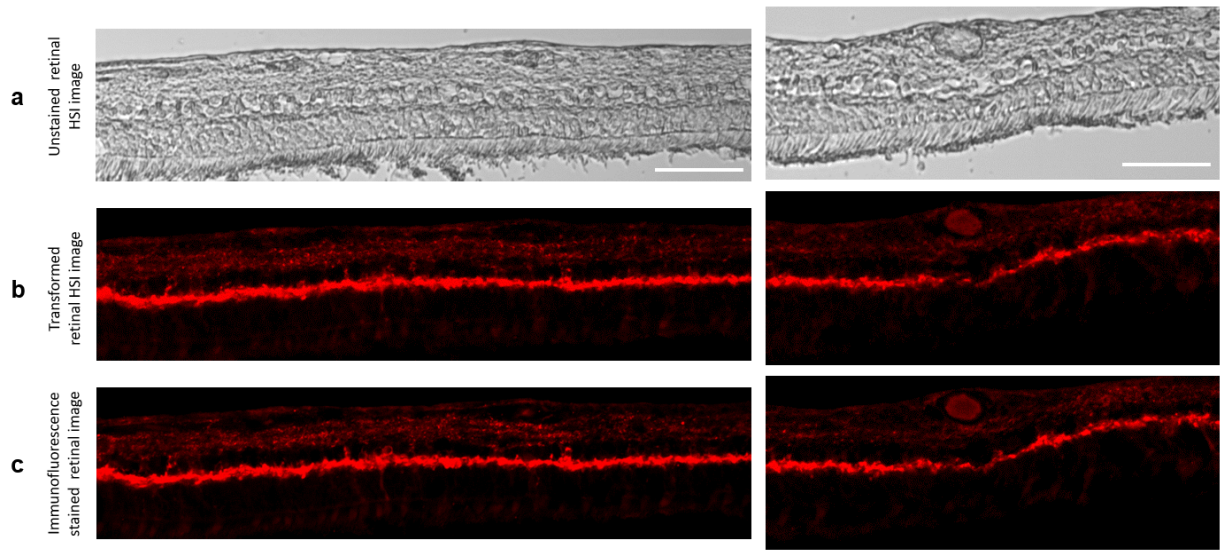

Figure 14. HSI histopathology prediction with the immunofluorescence-pS396-Tau model.

Left and right columns: two different FOVs. Scale bar, 100 μm.

Besides immunofluorescence staining, we also stained the retinal cross-sections with the same primary monoclonal antibodies and using a highly sensitive immunoperoxidase-based DAB substrate [6], [9]. The DAB-stained retinas have only one channel for the specific labeled protein, and we imaged them using a bright field microscope. The image so obtained has accurate single protein contrast and provides a better view of tissue structures. For DAB image transformation, the networks were trained to assign classification values to pixels and learn the color scheme that appeared in DAB images.

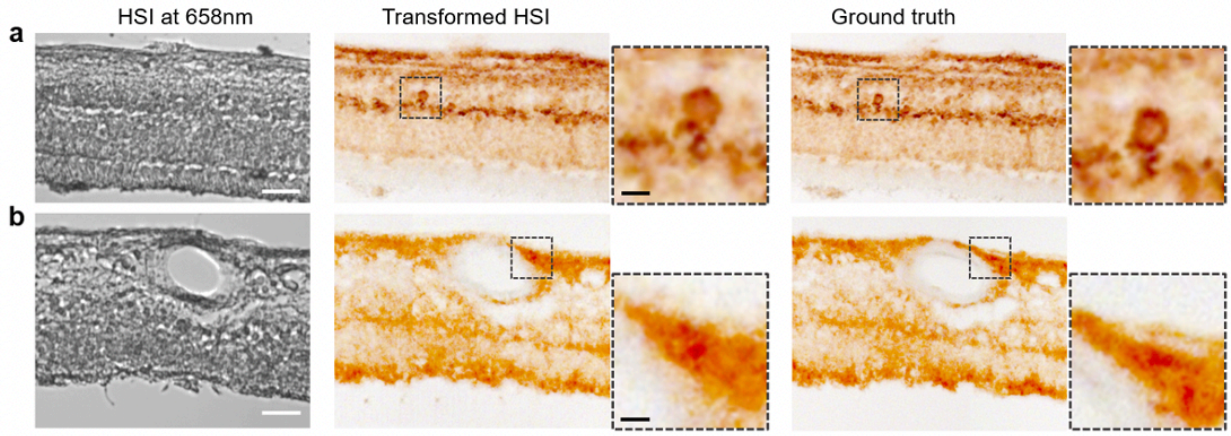

Figure 15. Stitched ROIs of the trained GAN models output.

(a). pS396-Tau DAB model, with a focus on a retinal NFT structure. (b). $A\beta_{42}$ DAB model. Scale bar, 50 μm for large FOV images, 10 μm for bordered zoomed inserts.

The trained DAB models can map the extent of Aβ and pTau deposits in a broad range with the DAB brown-color scheme. In Figure 15a, the transformed DAB-pS396-Tau image clearly shows layers of pTau deposits from the innermost layers to the OPL. In the OPL region, the structure of NFTs can be identified and visualized by our model (zoomed insert). There is also a signature band in the transformed DAB-pTau image, highlighting the pS396-Tau aggregation in the OPL with

apparent deposit patterns. In some regions or patients, the inner retina has comparable pS396-Tau aggregates to that in the OPL, appearing in dark brown spots and most connected, as shown in Figure 15a and Figure 16.

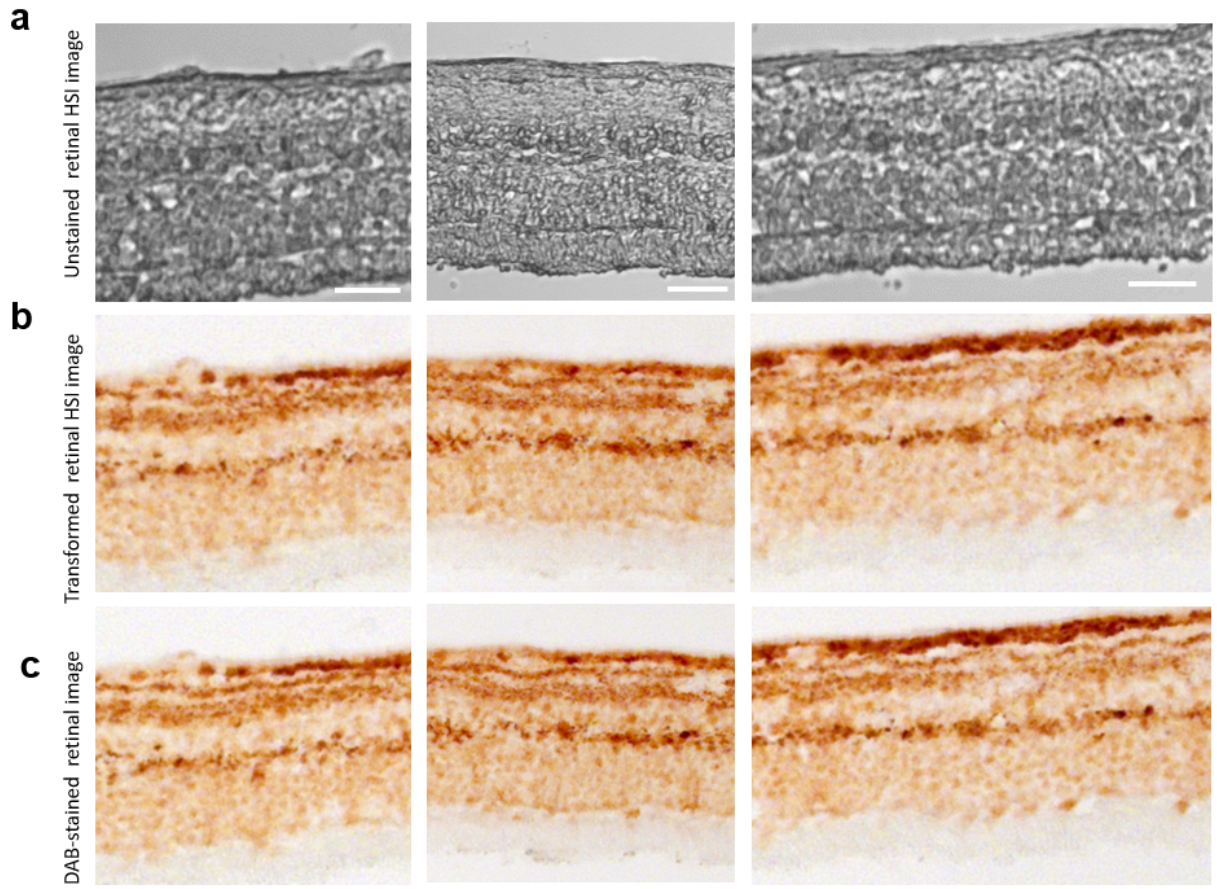

Figure 16. Histopathology prediction of hyperspectral images with the DAB-pS396-Tau model.

(a). Unstained HSI. (b). Transformed DAB- pS396-Tau image. (c). Real DAB-stained pS396-Tau retinal images. Left, middle, and right columns: three different FOVs. Scale bar, 50 μm.

On the other hand, the DAB-Aβ (12F4 mAbs clone) images show that $A\beta_{42}$ deposits appear in most retinal cell layers of cross-sections, a distribution that differs from pTau. The zoomed insert image in Figure 15b shows the predicted NFL/perivascular $A\beta_{42}$ accumulation, a location where

prominent $A\beta_{42}$ signals have been found in our previous studies [6], [9]. Additionally, $A_{\beta 42}$ distributes in NFL and GCL to a large extent, which can be seen in other FOVs as well (Figure 17b and 17c, right). In this human cohort, $A\beta_{42}$ deposits have also been found in the outer retina, especially in the ONL close to the outer limiting membrane, including the photoreceptor layer. Overall, $A\beta_{42}$ in confirmed AD dementia patients usually presents in both the inner and outer layers of retinal cross-sections.

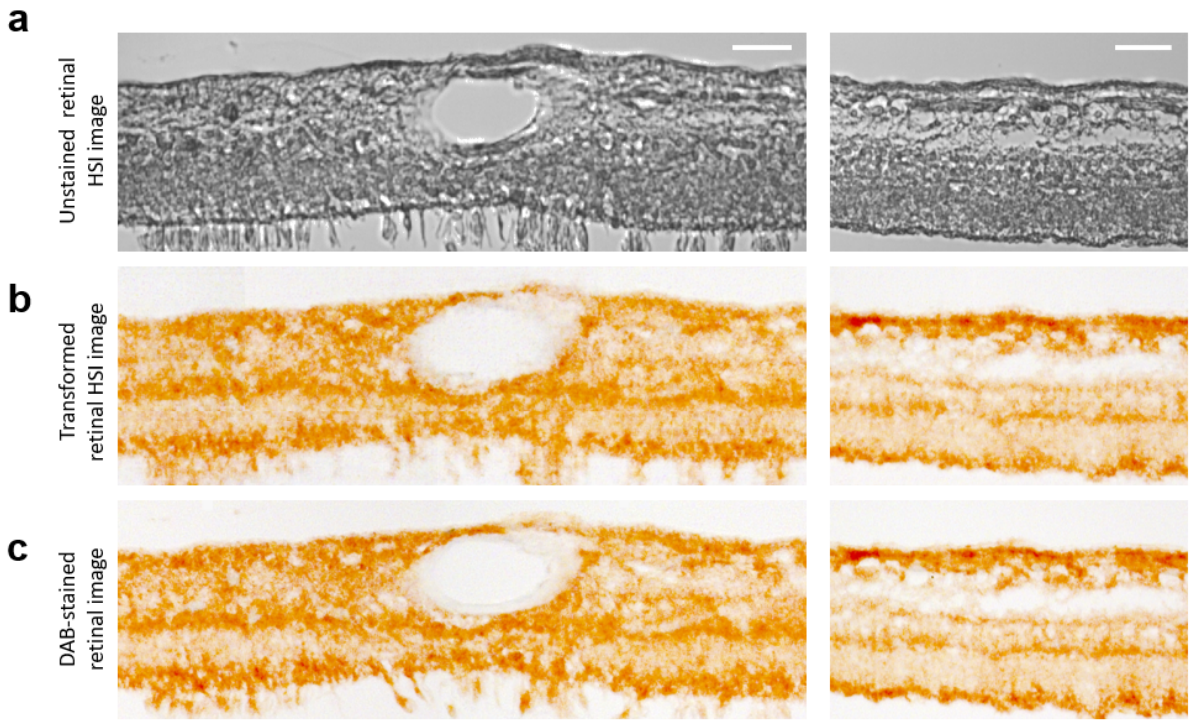

Figure 17. Histopathology prediction of hyperspectral images with the DAB-$A\beta_{42}$ model.

(a). Unstained HSI. (b). Transformed DAB-$A\beta_{42}$ labeled retinal image. (c). Real DAB-stained $A\beta_{42}$ retinal images. Left, middle, and right columns: three different FOVs. Scale bar, 50 μm.

The GAN network is essential for learning the complex spectrum difference and distinguishing biomarkers in the microenvironment of retinal tissues, assessing their distributions, and potentially generating histopathology-like images to facilitate AD diagnosis. To build the model, we excluded the regions to be analyzed when preparing the training datasets. Also, to avoid inaccurate classification caused by the overlay of channels in immunofluorescence staining, we trained the network with the $A\beta_{42}$ and pS396-Tau channels separately. We enlarged all datasets by data augmentation, mimicking the registration error between HSI and ground truth images, which, in turn, made the network more robust. The output prediction, a transformed histopathology-like image, correlates well with the ground truth. Compared with other spectral-based algorithms that take all spectral bands into training, our method requires less extensive computation, reduces network complexity, and makes training more efficient.

2.5 Evaluation metrics

The model output transformation images are compared to the corresponding ground truth using SSIM index and PSNR as similarity and quality measures. SSIM compares the transformed image with ground truth images in three measurements: luminance, contrast, and structure. PSNR is a common tool to assess the image reconstruction quality and it is used to assess the compression ratio of the transformed image. For each output image patch, an SSIM value and a PSNR value were calculated. The average and standard deviations values were calculated for each model group.

SSIM

We adopted a structural similarity index measure (SSIM) to assess the similarity between the transformed histopathology images by the GAN network and the actual stained images. SSIM is a

perception-based image quality metric [68], which has been widely used to evaluate the structural similarities between synthesized images in deep learning based methods. SSIM equals one means a perfect match, whereas close to zero indicates hardly similar images. The SSIM metric is calculated between the transformed image i and the ground truth image j as:

$$SSIM(i,j) = \frac{(2\mu_i\mu_j + c_1)(2\sigma_{ij} + c_2)}{(\mu_i^2 + \mu_j^2 + c_1)(\sigma_i^2 + \sigma_j^2 + c_2)}$$

where μ_i and μ_j are the averages of i and j; σ_i and σ_j are the standard deviations of i and j; σ_{ij} is the covariance of i and j; and c_1 and c_2 are regularization constants to avoid instability when the other variables are close to zero.

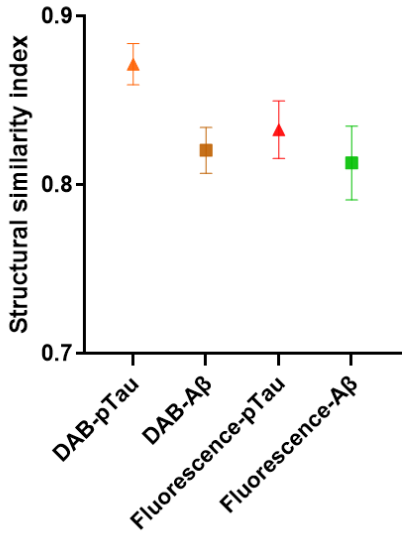

Figure 18. Averaged structural similarity index plot of the four models with error bars (standard deviation).

Figure 18 shows the averaged SSIM values for the four trained models: DAB-pTau, DAB-Aβ, immunofluorescence-pTau, and immunofluorescence-Aβ. DAB-pTau has the highest SSIM value of 0.8714 (+/−0.0122), while immunofluorescence-Aβ has the lowest SSIM value of 0.8128 (+/−0.0219).

Overall, the DAB models have a higher transformation performance than immunofluorescence models in our study when predicting the same biomarker deposits, and $A\beta_{42}$ histopathology images have lower transformation accuracies than pS396-Tau in both stains. This is possibly due to the fact that $A\beta_{42}$ is more abundant in the retina of AD patients than pS396-Tau, and it is highly dependent on disease development and assembly types, while pS396-Tau is found to be more layer-specific. Due to sample deformation during immunofluorescence staining, the HSI images could not be precisely registered to the immunofluorescence images, a fact that also lowers the SSIM values of immunofluorescence models.

The quantitative evaluation implies that the deep learning framework can transform the HSI images to histopathology images in high accuracy with a minimum SSIM of 0.8128. For the DAB-pTau model, we obtained an SSIM of 0.8714, which indicates the network can successfully recover the immunostaining color scheme and discriminate retinal pS396-Tau deposits. For comparison, a previous study that used a GAN network to transform quantitative phase images to H&E images achieved an SSIM value of only 0.80 [69].

PSNR

In addition to SSIM, the peak signal-to-noise ratio (PSNR) was used as the second metric to evaluate the image quality of the transformed histopathology images (Figure 19). The images

generated by the immunofluorescence-pTau model have the highest PSNR of 32.9626 (+/−1.03) dB. The immunofluorescence-Aβ images have the second-highest PSNR of 26.3196 (+/−1.63) dB. The DAB-pTau and DAB-Aβ models have a PSNR value of 23.3136 (+/−1.27) dB and 21.1323 (+/−1.29) dB, respectively.

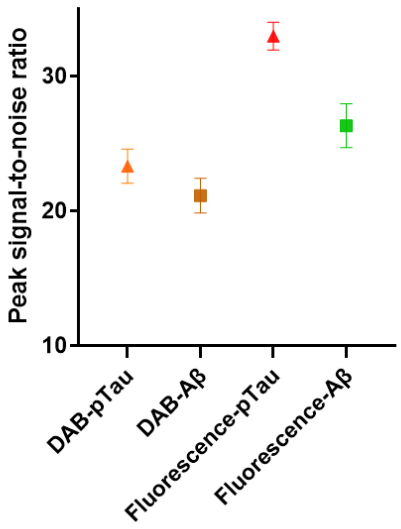

Figure 19. PSNR (in dB) of the four models with error bars (standard deviation).

All four models provide a PSNR value greater than 20 dB, indicating a high image quality. The immunofluorescence models have better image transformation quality than DAB models regarding PSNR. This might be because immunofluorescence-stained images have a less complex color assignment and a black background compared with DAB staining. Notably, the two pTau transformation models still outperform Aβ models like that in the SSIM metric. All SSIM and PSNR values were summarized in Table 1.

Table 1. Evaluation statistics by structural similarity (SSIM) index and peak signal-to-noise ratio (PSNR).

Model	SSIM		PSNR	
	Average	Standard deviation	Average	Standard deviation
DAB-pS396-Tau	0.8714	0.0122	23.3136	1.2700
DAB-Aβ_{42}	0.8203	0.0136	21.1323	1.2910
Fluo-pS396-Tau	0.8326	0.0171	32.9626	1.0297
Fluo-Aβ_{42}	0.8128	0.0219	26.3196	1.6265

2.6 Data and sample processing techniques

2.6.1 Image registration and data augmentation

The retinal HSI cross-sectional images were co-registered with the immunofluorescence/DAB-stained images of the same tissue section, for the purpose of analyzing the spectral signature and forming training pairs as the ground truth images for the transformation framework training. One spectral channel image with the most contrast was selected and registered with immunostained images using affine transformation. The intensity values of immunofluorescence images (8-bit) were subtracting 255 from each image pixel to get a complement image. First, apparent tissue features such as blood vessels and edges were used to crop the corresponding immunostained images to the same FOV of HSI images. Then rotation, translation, and scaling operations are applied on immunostained images to produce a nonreflective similarity transformation. In cases that the affine registration is not sufficient by visual inspection, an optional control-point registration is applied using control point pairs selected from the tissue, such as blood vessel edges. The control point registration is implemented by a local weighted mean of inferred second-degree polynomials from each neighboring control point pair to create a transformation mapping. Local

misalignment errors in registration due to the deformation during post-processing of imaged tissue are addressed in the training data preparation.

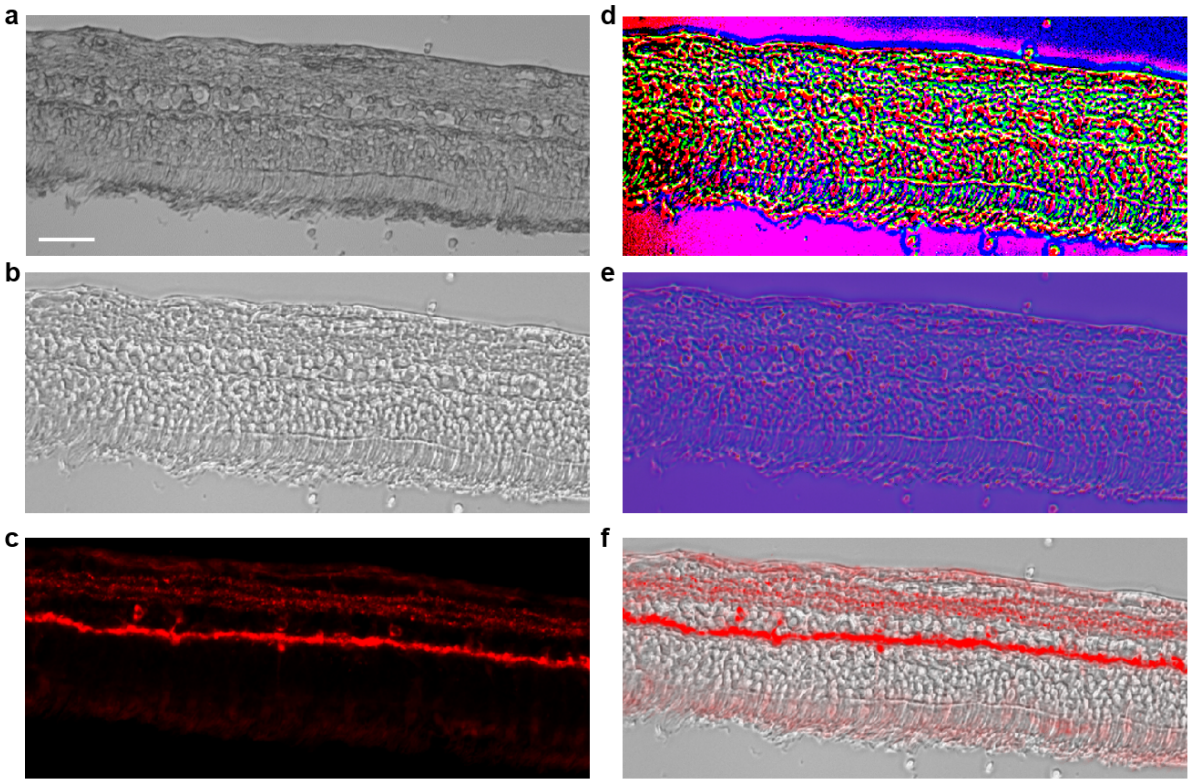

Figure 20. Hyperspectral image processing pipeline.

(a). Raw hyperspectral image. (b). Normalized hyperspectral image. (c). Corresponding ground truth image with pS396-Tau labeling. (d). Principal component analysis (PCA) processed image through normalized image b. (e). PCA-HSI retinal image after shifting and stretching the first three principal components. (f). Hyperspectral image with pS396-Tau labeling by image registration (b and c). Scale bar, 50 µm.

We implemented the traditional data augmentation techniques to enlarge our data size and make the network more robust to accommodate the offset that remained after the image registration. The operations include translation, rotation, flipping, scaling, and stretching, most of which were also

applied in the registration process. These similar transformations make the network adapt to the registration offset. By generating data under those conditions, we increased our dataset size by a factor of 12 and improved the spatial criteria confidence.

The input format of our GAN network is an image pair consisting of one compressed HSI image and the corresponding ground truth image in 8-bit. The HSI image slices were cropped to only keep a small portion of the background next to the retinal tissue, to ensure most HSI training data contained tissue spectral information. The first three principal components representing the spectral information were fed. The HSI image was cropped out as 256-pixel × 256-pixel × 3 patches, the corresponding ground-truth patches were cropped from the previous co-registered immunostained images. The selected analyzed regions of stained tissue were left and cropped as test image patches, with 1/3 to 1/2 overlap. This is to avoid the discontinuous intensities when stitching back the transformed patches. The other parts of image were cropped and separated into training and validation set. Validation data was randomly selected from training data. The numbers of image pairs used for the four models training are given in a Table in Appendix B. The patches containing damaged tissue regions and severely deformed staining tissue that led to an unreliable registration during the staining process were discarded

We stitched the output images from the trained GAN models with a self-derived algorithm. The algorithm iterates to find the best connective coordinate by scanning the corresponding overlap region of the two adjacent image patches, then stitches the images at this position. For the several cases when images have connective artifacts, we averaged the intensities of neighboring columns of the connective coordinate. As for the raw HSI retina images, we chose one image slice at one well-contrasting wavelength and stitched all connected FOVs using the Image Composite Editor software.

2.6.2 GAN training parameters

The GAN network used in our study is adapted from a conditional GAN [70]. The generator network is based on a U-net using Pytorch. We incorporated a structural similarity index (SSIM) component into the generator loss function as $-\nu \times \log\left[(1 + SSIM(G(x), y))/2\right]$. Mean absolute error ($L_1$) loss is used to regularize the generator to transform the input image accurately and in high resolution. SSIM is used to balance the L_1 loss of learning correct features rather than the pixel accuracies.

The network utilizes both spatial and spectral information to classify Aβ/pTau. The transformed histopathology images output from the generator were evaluated by a three-layer discriminator. We trained the compressed HSI images of Aβ and pTau and the two corresponding immunostainings separately and obtained four trained models. The four models were used to transform the test HSI images to Aβ and pTau stained immunofluorescence and DAB images. The weights for the loss function components were set as 100 for L_1 loss and 100 for SSIM term. We achieved optimal results with learning rates of 5×10^{-6} for the immunofluorescence models and 1×10^{-5} for the DAB models using the adaptive moment estimation (Adam) optimizer. The batch size was set to one under the instance normalization. The epoch number was in between 120 and 150, with 50 epochs for decayed learning rate. Training time was approximately 47 h for immunofluorescence models and 82 h for DAB models. The network was implemented with one GTX TITAN graphical processing unit (GPU) using Pytorch 1.6.0, and Python version 3.6.8 on a desktop installed with Ubuntu 16.04 operating system. The desktop is equipped with CPU Intel Core i7-6900K@3.20 GHz and 64 GB RAM.

2.6.3 AD confirmed human retina cross-sections

Postmortem human eyes were obtained from the Alzheimer's Disease Research Center (ADRC) Neuropathology Core in the Department of Pathology (IRB protocol HS-042,071). Histological studies at Cedars-Sinai Medical Center were performed under IRB protocols Pro00053412 and Pro00019393. For the histological examination, 12 retinas were collected from deceased patient donors. The retinas from 10 donors with clinically and neuropathologically confirmed AD (n = 2), MCI (n = 3), and cognitively normal (CN; n = 5) were used in the early stage of the training phase of immunostaining (demographic data on human donors are given in the table in Appendix). Additionally, n = 3 neuropathologically confirmed AD dementia patients were used for histological and HSI analyses followed by network training; donors' age, gender, ethnic background, premortem and final diagnosis, Braak stage, Clinical Dementia Rating (CDR) and/or Mini-Mental State Examination (MMSE) score, and postmortem interval (PMI) of tissue collection are detailed in Appendix A.

Cognitive testing scores from evaluations made closest to the patient's death were used for this analysis. Two global indicators of cognitive status were used for clinical assessment: the CDR scores (0 = normal; 0.5 = very mild dementia; 1 = mild dementia; 2 = moderate dementia; or 3 = severe dementia) [71] and the MMSE scores (normal cognition = 24–30; MCI = 20–23; moderate dementia = 10– 19; or severe dementia $\leqslant$ 9) [72]. In this study, the composition of the clinical diagnostic group (AD, MCI, or CN) was determined by source clinicians based on findings of a comprehensive battery of tests including neurological examinations, neuropsychological evaluations, and the aforementioned cognitive tests.

Fresh-frozen eyes and eyes preserved in Optisol-GS were dissected with anterior chambers removed to create eyecups. Vitreous humor was thoroughly removed manually. Retinas were dissected out, detached from the choroid, and flatmounts were prepared [9]. By identifying the macula, optic disc, and blood vessels, the geometrical regions of the four retinal quadrants were defined with regard to the left and the right eye. Flatmount strips (2 to 3 mm in width) were dissected along the retinal quadrant margins to create four retinal quadrants: superior-temporal (ST), inferior-temporal (TI), inferior-nasal—IN, and superior- nasal—NS, and were fixed in 2.5% PFA for cross-sectioning. Previous studies show that both retinal Aβ and pTau are primarily distributed in peripheral superior and inferior retinal quadrants [2], [6], [8], [15]. Therefore, the retina cross-sections were sectioning from ST and TI strips (Figure 21).

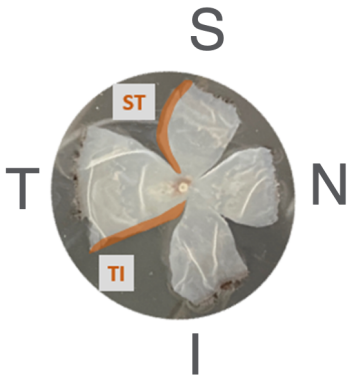

Figure 21. Donor eye fixation, neurosensory retina isolation to flatmounts, creating four retinal quadrants (S: superior, T: temporal, I: inferior, N: nasal), and sectioning of superior-temporal (ST) and inferior-temporal (IT) strips.

Each strip was approximately 2 to 2.5 cm long from the optic disc to the ora serrata and included the central, mid, and far retinal areas. All the above stages were performed in cold phosphate-buffered saline (PBS) with 1 × Protease Inhibitor cocktail set I. As described above, a set of

flatmount strips, Superior Temporal (ST), Inferior Temporal (IT), Inferior Nasal (IN) and Nasal Superior (NS), was dissected (2–3 mm in width), washed in 1x PBS, and processed for retinal cross-sectioning.

2.6.4 Immunostaining validation

Immunofluorescence-stained retinal cross-sections

Retinal cross-sections were treated with primary antibody of the following combination: mouse anti-Aβ 1–42 antibody, 12F4 (1:500, BioLegend #805,502), and rabbit anti-pTau antibody, pSer396 (1:2500, AS-54,977). The 12F4 antibody is specific to the detection of amyloid beta x-42, without cross reacting with amyloid beta x-40 or amyloid beta x-43. Retinal sections were then incubated with secondary antibodies (1:200; Cy5 conjugated donkey anti mouse and Cy3 conjugated donkey anti rabbit, Jackson ImmunoResearch Laboratories). After rinsing with 1× PBS, sections were mounted with Prolong Gold antifade reagent with DAPI (Thermo Fisher #P36935). Fluorescence images were repeatedly captured at the same focal planes with the same exposure time. Tiling mode and post-acquisition stitching were used to capture and analyze large areas. Multichannel image acquisition was used to create images with multiple channels. Images were captured at 20 x, 40 x, and 63 x objectives for different purposes. Routine controls were processed using identical protocols while omitting the primary antibody to assess nonspecific labeling.

Peroxidase-based immunostained retinal cross-sections

Retinal cross-sections after deparaffinization were treated with target retrieval solution and washed with 1× PBS. For a list primary antibodies and dilutions, see above Immunofluorescent staining. Following the treatment with formic acid, the tissues were washed with wash buffer 1× (Dako

S3006) and adding 0.2% Triton X-100 (Sigma, T8787), then were treated with 3% H_2O_2 washed. Each primary antibody was diluted with background reducing components (Dako S3022) and incubated separately with the tissues overnight in 4◦C. Tissues were rinsed with wash buffer on a shaker, then incubated separately at 37◦C with secondary Ab (anti-mouse ab HRP conjugated, DAKO Envision K4001 or anti-rabbit ab HRP conjugated, K4003). Liquid DAB+ Substrate Chromogen System (DAKO K3467) was used, then slides were immersed in dH_2O and washed. Tissues were mounted with Faramount aqueous mounting medium (Dako, S3025). Routine controls were processed using an identical protocol while omitting the primary antibodies to assess nonspecific labeling. Brightfield images were repeatedly captured at the same focal planes with the same exposure time. Images were captured at 20 x, 40 x, and 63 x objectives for different purposes. Tiling mode and post-acquisition stitching were used to capture and analyze large areas.

2.7 HSI Discussion

We demonstrated a hyperspectral imaging platform that enables label-free, high-resolution structural, and molecular imaging of Aβ and pTau deposits in human retinas. The advantage of HSI is its label-free imaging ability by capturing tissue spectrum across a broad spectral range. Our system illuminates the sample using a simple broadband halogen lamp and scans the sample wavelength using a liquid crystal filter. The quantified intensity values from the spectral channels imply the optical characteristics of the AD biomarkers, Aβ and pTau. The discovered $Aβ_{42}$ and pS396-Tau spectral signatures are highly consistent in various regions of retinal cross-sections and among the patients. We also examined the consistence of the HSI data by reimaging the samples in an extended period of time (14 d), and we found that the spectral signatures of both $Aβ_{42}$ and pS396-Tau remain the same. More importantly, we are the first to report the pS396-Tau in the

human retina and its spectral signature. We further visualize pS396-Tau with a label-free imaging technique. Our method, which can probe pTau deposits, has the potential to advance AD quantification and diagnosis. Seeing its label-free imaging ability and system simplicity, we also anticipate the presented HSI method will become an alternative or complementary approach to histopathological analysis of Aβ and pTau in CNS organs and other tissues.

We imaged the entire strips of the retinal cross-sections of AD patients, followed by immunofluorescence labeling. The AD characteristic deposits of $A\beta_{42}$ and pTau were found to occur at specific locations of the strip. Selected regions without signals for $A\beta_{42}$ or pS396-Tau, which we refer to as "lack of signal" regions, served as internal controls; this should be considered more rigor than using another subject's tissue. The main goal of this feasibility study is not to differentiate between populations with or without AD, rather, it is to identify for the first time the spectral signatures of retinal $A\beta_{42}$ and pS396-Tau and compare to previous signatures of retinal Aβ deposits. The strip portions with little deposits can be reasonably considered as normal $A\beta_{42}$ and pTau deposits in the aging development like in a non-AD patient, as our previous results show that the amount of normal accumulation significantly differs from the AD characteristic deposits [9], [15]. In future studies, we aim to scan variety of strips in attempt to quantify and possibly distinguish between individuals with high and low AD pathology.

In the current study, because the samples are optically thin and directly accessible to the microscope, we normalized the spectral intensities at each wavelength with respect to the value at the peak emission. For in vivo patient imaging, the normalization process is complex because spectral transmission of the ocular lens is generally unpredictable in the elderly population. Because previous studies show that both retinal Aβ and pTau are primarily distributed in peripheral

superior and inferior retinal quadrants [2], [6], [8], [15], a possible solution for in vivo spectral normalization is to use a control area in the nasal retinal quadrant of the same subject.

Our findings on the spectral signature of Aβ echo many pioneer works in the field. For example, Xavier Hadoux et al. [20] discovered a significant difference in ocular reflectance among patients with and without moderate-to-high Aβ levels, and they confirmed their findings through imaging the paired brain samples. As another example, More's group [50], [51], [52] reported the spectral signature of $A\beta_{42}$ in both retina and brain tissues in human and transgenic mouse. Nonetheless, all these previous studies lack a direct validation through immunostaining. Moreover, because the measurements were performed in the widefield imaging mode, the distribution of Aβ in retinal cross-sections remains elusive. Our findings presented herein, therefore, provides the basis for the previous research.

In addition, we developed a framework to facilitate the classification of the spectral signatures of retinal $A\beta_{42}$ and pS396-Tau and transformed the unstained HSI images to histopathology-like images. Our GAN network is robust to local misalignments in registration and staining overflow because we created augmented training data to mimic those influences. This is especially useful for immunofluorescent image transformations because the staining process is more complex and less specific than the DAB-staining. The inaccuracies in the staining and image acquisition processes must be taken into consideration to avoid confusing the network. Another benefit of using the transformation framework is that it can be trained to generalize the variations of the histopathology stained tissues across different sections and patients with sufficient datasets.

The $A\beta_{42}$ and pS396-Tau in the two standard staining techniques, DAB and immunofluorescence, were trained separately as four models. Multichannel immunofluorescence transformed images of a single tissue region can be achieved by combining the generated $A\beta_{42}$ and pS396-Tau images in

green and red channels. An advantage of training separately, especially for immunofluorescence stains, is avoiding overlapping between two channels. With a well-trained transformation model, the histopathology images can be generated instantaneously, without the need for tedious pathological processing.

In conclusion, we developed a label-free HSI method as a tool to report $A\beta_{42}$ and pS396-Tau spectral signatures and a deep learning based framework to transform the unstained HSI image to a histopathology-like image. Our method thus democratizes the immunofluorescence/DAB staining and makes them accessible to general labs. Also, our entire workflow (Figure 10) is time efficient. Scanning the sample and computing the transformed images take less than 30 min for the whole process, which is only a fraction of the time typically needed when the sample undergoes the conventional pathological processing (2 to 4 days). We expect our method will lay the foundation for future label-free AD screening and diagnosis using HSI approaches.

Chapter 3 Light Field Endoscopic Imaging

Current optical endoscopes are mostly limited by two-dimensional views or very small number of three-dimensional (3D) views of pathological sites. We built a flexible light field endoscopy (Flex-LFE) imaging system for high-resolution 3D imaging based on a fiber bundle. The intrinsically low resolution of the fiber-based light field imaging was significantly improved by training a deep neural network. The resulting sub-image resolution is close to the free-space light field setup. We demonstrate the depth imaging capability of Flex-LFE with fluorescence tissue paper. The calculated depth information helps in assessment of the 3D tissue lesions. Implementing the deep learning model with the light field system can achieve real-time and high-resolution visualization of the reconstructed scene.

3.1 Fiber-based optical endoscopy

Optical endoscopy has been extensively employed worldwide by physicians to diagnose or treat disease. These probes are inserted into the body through small incisions or natural body openings to provide high-resolution images of internal organs and tissue. Depending on whether the image is transmitted through lenses alone or optical fibers, optical endoscope are generally classified into two categories, rigid and flexible [73], [74], [75]. Compared with the rigid counterparts, flexible endoscopes feature a lower rate of complications, increased patient comfort, and a lack of requirement for general anesthesia [75]. Moreover, the flexible endoscopes allow the visualization of the entire gastrointestinal tract, such as esophagus, stomach, and duodenum, which are generally inaccessibly by rigid endoscopes.

Despite widespread use, conventional flexible optical endoscopes have crucially limited to two-dimensional (2D) views of pathological sites. Because most tissue lesions manifest themselves as abnormal three-dimensional (3D) structural changes [76], the lack of depth information frequently jeopardizes the diagnostic usefulness. Depth imaging is critically needed in medical diagnostics and intervention. In particular, effective in situ endoscopic assessment relies precise 3D volume measurement and shape characterization of tissue lesion. For instance, the 3D volume of the tumor is an established metric for the diagnosis and choice of treatment for early-stage gastric tumors [77]. Currently, this is evaluated either by manipulation with forceps or by visual inspection alone, which is qualitative and prone to human errors. Another striking example impacts approximately 20 million people in the US who undergo minimally invasive surgery (MIS) annually. As an enabling tool of MIS, laparoscopy provides high definition 2D images of the surgical site. However, the surgeons are unable to perceive depth, impairing their hand-eye coordination and therefore decreasing their abilities to tap into the benefits of this new technology space [78]. Astoundingly, it was reported that 97% of surgical accidents during laparoscopic intervention are attributed to the visual misperceptions [79].

Except for the 2D imaging limitations, most flexible optical endoscopes also suffer from low resolution, causing by the intrinsic gap structures of the fiber cores in an imaging fiber bundle. Figure 22 illustrates the imaging surface of a fiber bundle and the fiber core arrangement. Moreover, because of limited core numbers, a trade-off must be made between the spatial resolution and the number of 3D views. This further limit the image quality when apply the flexible optical endoscopes in 3D scenario. We proposed a flexible optical imaging system combined a fiber bundle with light field imaging. A balanced number of views and sub-image pixel numbers were designed to build the reconstructed object image with depth information. In addition, the low

resolution of the raw light-field image caused by the limited number of fiber cores and artifacts introduced by the fiber bundle structure are handled by imaging post-processing based on deep learning.

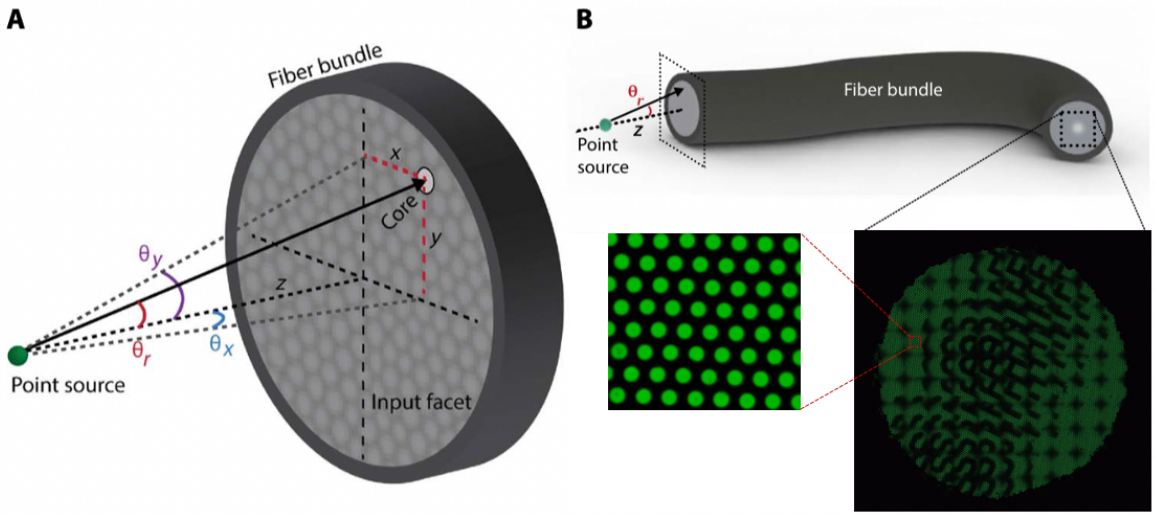

Figure 22. Illustration of fiber-based imaging.

(a) Cross-section of an imaging fiber bundle. (b) The imaging surface of the fiber bundle in the proposed light-field mode. Adapted from [80].

3.2 Light-field imaging fundamentals

The light field camera, or plenoptic camera, is a new generation of depth imaging technology that captures an incoming light ray's spatial as well as angular information in one shot [81], [82], [83]. The data obtained by the light field camera enables computational reconstruction of a depth map of the imaging object and even allows for refocusing the image at different depths. Light field cameras are typically classified into two main categories: the unfocused light field (ULF) camera

and the focused light field (FLF) camera. Figures 23a–c give the schematics of a ULF camera and two types of FLF cameras, namely the Keplerian and Galilean configurations [84], respectively. The main difference between these three configurations is the distance between the microlens array (MLA) and the detector array. The detector in the ULF setup is to image the pupil by placing at the back focal plane of the MLA. In the FLF configurations, the detector captures a sharp image of the object by placing before or after the formed intermediate image plane.

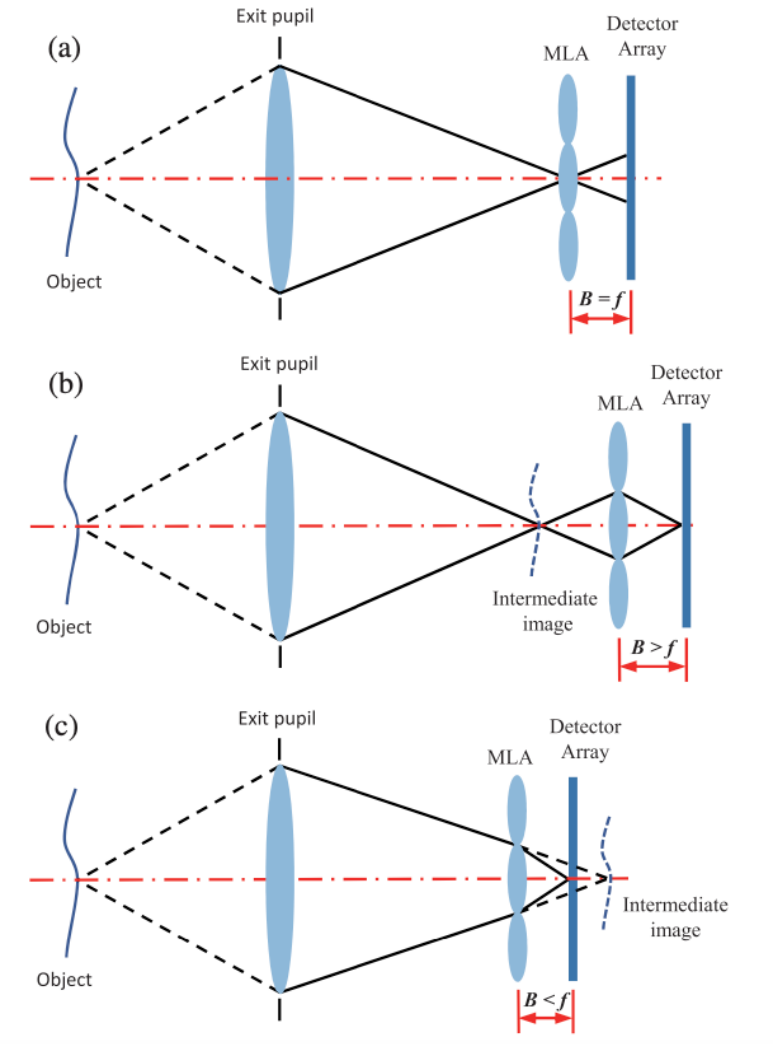

Figure 23. Schematics of (a) ULF and FLF light field cameras of (b) Keplerian (c) Galilean configurations [85].

We adopt the Galilean configuration for the flexible light-field endoscope design. The system is shown in Figure 24. We built a free-space FLF camera at first, then transformed it into a fiber-based detection. The free-space FLF camera was also used for acquiring high-resolution light-field images as part of the training data in the later deep learning approach.

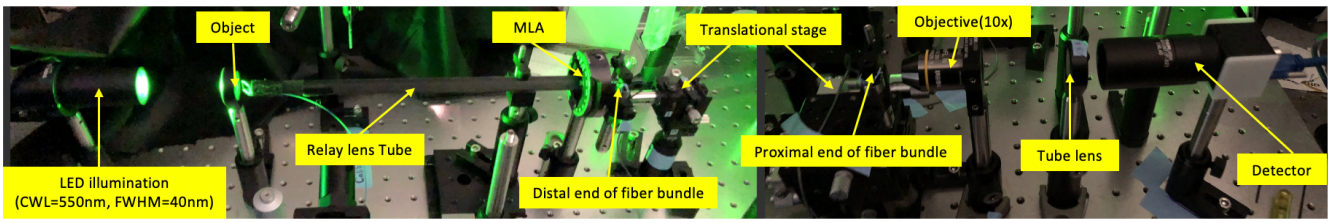

Figure 24. Galilean configuration focused LF system.

3.3 Flexible light-field endoscopy (Flex-LFE)

To address the limitations of current optical endoscopes, we integrate the light field camera with a flexible optical imaging bundle, for 3D endoscopic imaging, which we term flexible light field endoscopy (Flex-LFE). The Flex-LFE system is flexible, compact, and fast, with the millimeter-sized micro-lens array and fiber bundle. Design parameters are shown in Table 2 and 3. It provides approximately 70 views for accurate depth estimation, overcoming the common obstacles encountered by other depth imaging techniques. We believe that the Flex-LFE imaging technique will be versatilely useful in various clinical and surgical applications including the identification of a variety of tissue lesions, real-time monitoring of laparoscopic interventions, and accurate assessment of the 3D tissue structure.

The Flex-LFE system was built based on a standard focused LF imaging system by utilizing a SCHOTT Leached Fiber Bundle. As given in Table 2, the imaging diameter of the fiber bundle is

900 μm, with an outer diameter of 1.05mm. The bundle comprises 18,000 fiber cores, each functioning as an individual imaging pixel.

Table 2. Parameters of the fiber bundle.

Parameter	Value
Outer diameter	1.05 mm
Imaging diameter	900 μm
Number of fiber cores	18,000
Diameter of fiber core	7.6 μm
Length	760 mm

Table 3. Microlens array parameters.

Parameter	Value
Dimension	10 x 10
Pitch	100 μm
f-number	7.8

The Flex-LFE schematic is shown in Figure 25. In fiber imaging mode, each fiber core serves as an image pixel, and the pixel size is 7.6 μm in diameter. The sample end of the endoscope adopts a compact design by utilizing the micro-lens array (MLA) directly as the objective lens to collect the light from the sample. The MLA (RPC photonics, MLA-S100-f8) has a pitch of 100 μm and a f-number of 7.8. A broad-band halogen lamp was used for illumination. For better image sharpness, a bandpass filter (BPF) with central wavelength of 550 nm (FWHM=40nm) was applied to the

illumination light before the sample. Because the fiber bundle only transmits light intensity, we use the focused light field imaging scheme with the MLA focusing the collected light from sample onto the surface of the fiber bundle proximal end. The sub-category of the focused light field imaging mode which we applied in Flex-LFE is Galilean configuration [86], which means the distance between the MLA and the surface of the fiber bundle is smaller than the focal length of the MLA.

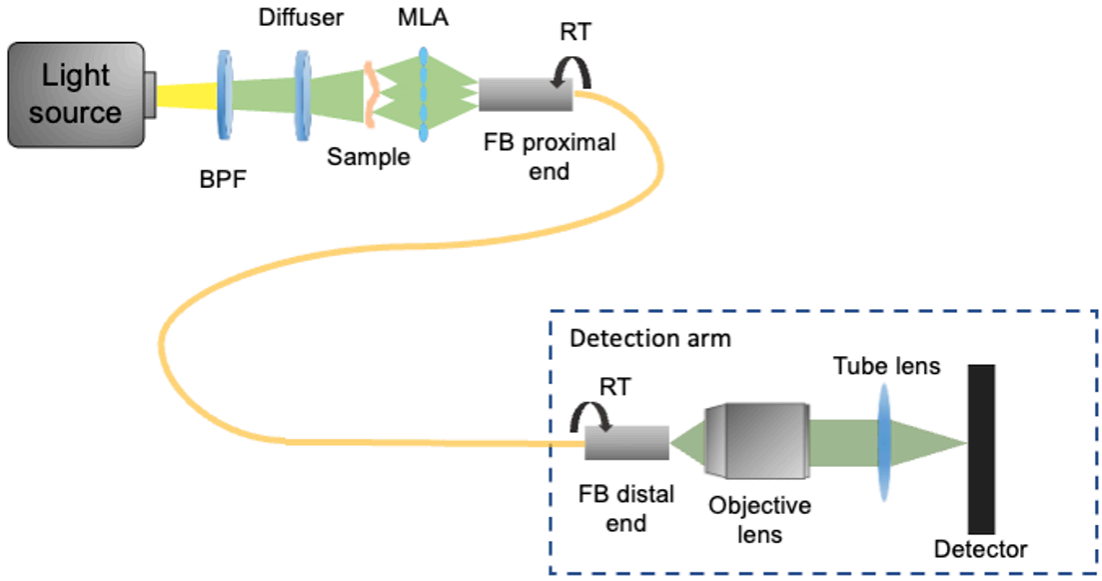

Figure 25. System schematic of the Flex-LFE. BFP: band pass filter. MLA: microlens array. FB: fiber bundle.

For the detection arm of the system, an 10X microscope objective lens (Olympus, 0.25 NA, 10.6 mm WD) was used after the distal end of the fiber bundle to efficiently collect the light and magnify the transmitted light field image. A tube lens with 100 mm focal length was utilized to relay the magnified sample image onto the detector. Because of the flexibility of the fiber bundle, a rotation mount was used for the MLA to tune the orientation of the microlens matrix with respect to the

detector, which is to fit the arbitrary 'twisting' between the distal and proximal ends of the fiber bundle while imaging. A well aligned raw Flex-LFE image should contain an 8×7 sub-image array that can be fully used in the image processing.

Unlike free-space image transmission in the air, Flex-LFE can lead the light in a directed manner through a large number of closely arranged optical fibers. However, the gaps among the fiber cores needed to be removed from the raw images before further processing. Gaussian filter achieved the best results in removing these uniform distributed 'dark-space' between the informative fiber cores. The kernel size needs elaborate choosing to avoid further blurring of the fiber-bundle image, or in other hands it can cause remained fiber-core patterns that will affect the subsequent reconstruction. Same object of USAF target was imaged in Figure 26. It shows sub-images from a free-space LF camera in high resolution while the resolution of fiber-based LF is plagued by the limited imaging pixels and the pattern removal process. This resulting issue of image quality is solved by computational methods described in the next section.

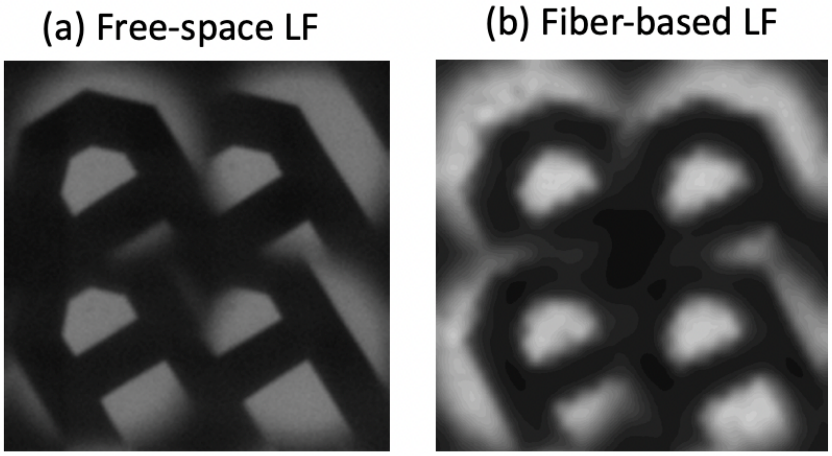

Figure 26. Sub-image of (a) Free-space LF camera and (b) Fiber bundle based LF (after gap-pattern removal).

3.4 Super resolution

The fiber bundle intrinsically reduced the image resolution with very limited pixel numbers (~120) for each microlens image, or sub-image. The inherent gap structures between the fiber cores within the imaging fiber bundle also cause the flexible optical endoscope to suffer from low resolution. Moreover, the light field camera reconstruction process will further reduce the resolution. Therefore, we process the image after the fiber-pattern removal with a super-resolution technique powered by deep learning. We applied a pix2pix GAN network [70] by defining a new loss function specified for the study, which can be written as followed:

Generator:

$$L(G;D) = -logD\big(G(x)\big) + \lambda \times MSE(G(x),y) - \upsilon \times \log\left[\frac{1+SSIM(G(x),y)}{2}\right]$$

Discriminator:

$$L(D;G) = -logD(y) - \log\left[(1 - D\big(G(x)\big)\right]$$

where x is the low-resolution image, y is the high-resolution image (ground truth), and G/D denotes the forward pass of the generator/discriminator network, λ and υ are weights to govern the loss terms in training. To prepare the training dataset, we built a standard focused LF system with the same optics without the imaging fiber bundle. A 1.0X telecentric lens ((Edmund, 58430) is used to image the sample and relay the sample image onto the MLA. The field of view of the telecentric lens is 8.8 mm × 6.6 mm. This maximized the light throughput and its tunable f number (6~22) is set to match the NA of the MLA.

A variety of objects with diverse feature types were imaged to train the network. Each normal light field shot has 260 sub-images. To crop out the sub-images, we first imaged a white scene and locate the central points of the sub-images by finding the brightest pixels. The cropped sub-images were undergone feature detection to select ones that have over 1/4 areas containing features to ensure the learning efficiency of the network. These captured real high-resolution light field (HR-LF) images serve as the ground truths in the training. Also, the real HR-LF images help the network understand the natural blurring of the aperture shape in each sub-image. To prepare the low-resolution (LR) images, we applied the same type of filter used in the pattern removal process for fiber-based LF, which is a Gaussian-type filter, to blur the raw images to a competitive level with the Flex-LFE images. The processed LR images and the real HR-LF images were resized to 256 × 256 pixels and form into image pairs (256 × 512 pixels) to feed into the training networks. Based on training experiments, a U-net was chosen as the generator network, and a three-layer discriminator network outperforms a five-layer one in the test results. The results were not improved by applying more layers in the discriminator network, in turn it slowed down the convergence. The network was implemented based on Pytorch with one graphical processing unit (GPU) RTX 3090, on a desktop installed with Ubuntu 18.04 operating system. The desktop is equipped with CPU AMD Ryzen 9 5950X. For the model training, the weights for the loss function components were set as 50 for both MSE loss and SSIM term. We used the adaptive moment estimation (Adam) optimizer and achieved optimal results with learning rates of 2×10^{-5}. Training time was approximately 5 h with batch size set to one. The network workflow is shown in Figure 27.

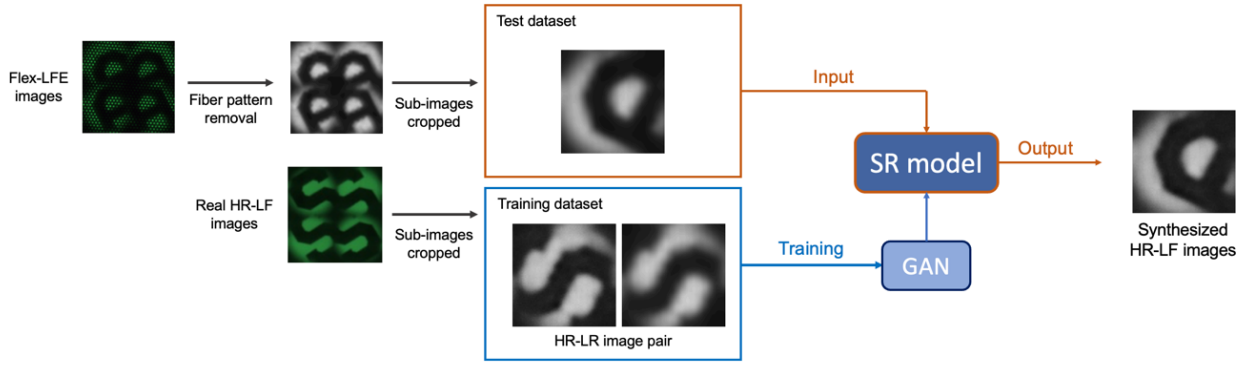

Figure 27. Data processing and deep learning training workflow with SR-GAN.

The optimal model identified during the training process was applied to the cropped Flex-LFE sub-images. Each LR sub-image was cropped out from the Flex-LFE raw image (Figure 27) after pattern removal process. They were cropped out around the central point matrix which was determined using a pre-imaged white scene. After cropping, the sub-images were resized to individual 256 × 256 pixels each and processed through the model to generate the synthesized HR-LF images. Then, the synthesized HR-LF images were stitched back according to the saved coordinates of the central points (Figure 28c). The HR Flex-LFE image will then be used to reconstruct the HR object image (Figure 29b).

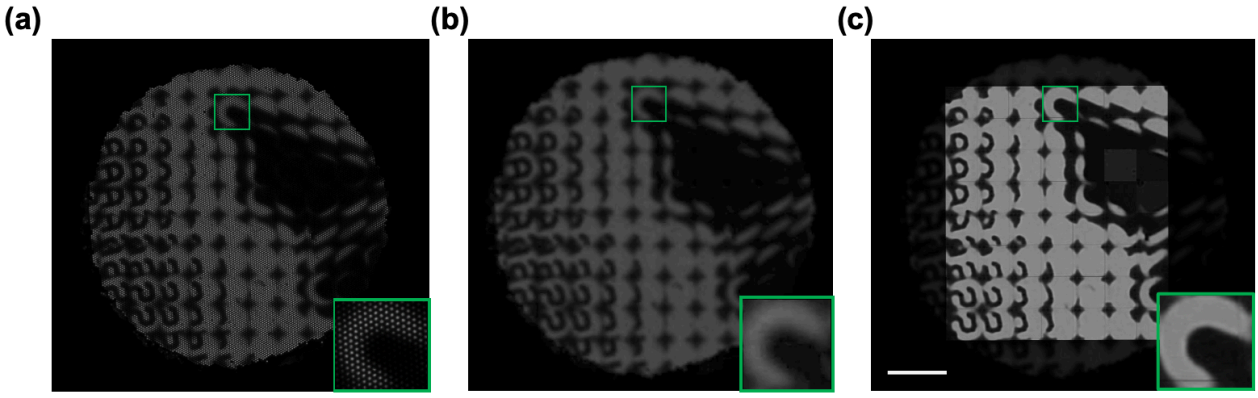

Figure 28. Data processing and SR-GAN Model inference results.

(a) Flex-LFE raw image. (b) Flex-LFE image after fiber pattern removal. (c) HR Flex-LFE image after stitching back the synthesized HR sub-images. Bottom right boxed images are the magnified sub-images of the box areas. Scale bar: 200 μm.

A butterfly phantom was imaged with a letter object in one scene in Figure 28, and the imaging data followed the designed processing pipeline. The sub-images in Figure 28c were synthesized using the pre-trained SR-GAN model. From the bottom right sub-image, it can be seen that the outline of the object feature, wing tip, has a significant improvement compared to Figure 28b. Measurements on the resolution improvements are provided and discussed in the evaluation section. Figure 29a and 29b present the final reconstructed object image. The application of the SR-GAN model enables clear visualization of the corner and turning points of the feature.

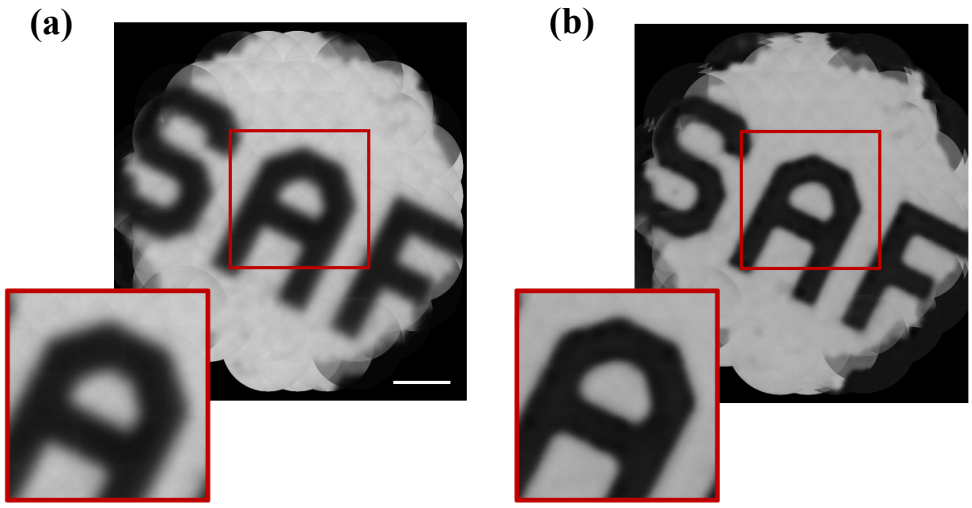

Figure 29. Reconstructed Flex-LFE results.

(a) LR reconstructed image of Flex-LFE. (b) Synthesized HR reconstructed result of Flex-LFE. Bottom left boxed images are two magnified subfields of the reconstructed images. Scale bar: 200 μm.

3.5 Depth reconstruction

Currently, only a few methods are available for 3D endoscopic imaging, such as stereoscopy [87], [88], [89], structured light [90], [91], and optical coherent tomography (OCT) [92], although given the vital importance. Stereo endoscopes simplicity, stereo endoscopes suffer from depth ambiguity due to a limited number of views. The structured-light endoscopes employ two sub-systems to project a pattern onto the tissue and image the back reflected light, respectively. The depth map is then computed by measuring the deformation of the illumination patterns. Although structured-light endoscopes can recover depths with high fidelity, the requirement for specialized illumination usually leads to a bulky setup. Lastly, the OCT endoscope acquire high-resolution 3D images of tissue based on interferometry. However, because of the reliance on mechanical scanning, the OCT endoscopes face a fundamental trade-off between imaging speed and field-of-view, restricting their use in imaging dynamics in 3D.

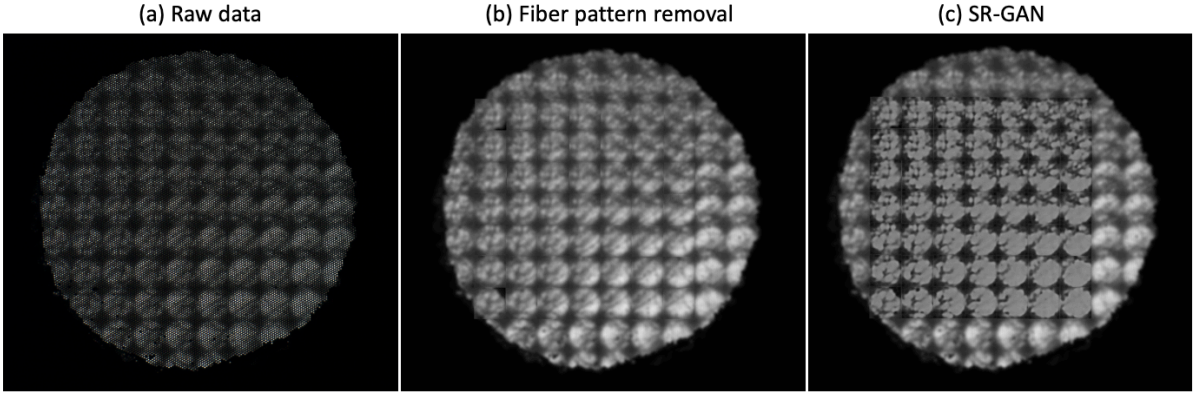

Figure 30. Fluorescence tissue fiber imaging using Flex-LFE.

The Flex-LFE system can image the object scene at one single shot. To balance the resolution for object and depth reconstruction, we selected the MLA matched to the fiber bundle in order to

generate 79 field of views, shown in Figure 30a. We demonstrated the 3D imaging capability of the Flex-LFE system by imaging a tissue paper. The tissue fiber was stained with yellow fluorescence. When imaging the tissue fiber, the illumination was changed to a diode-pumped solid-state laser (MGL-III-532) at 532nm under reflection mode for excitation, then the emitted fluorescence beam passed through a 50 nm BPF at 590 nm (Chroma, ET590/50m) to filter out any excitation or ambient light. The tissue paper was positioned in a tilted manner to create a depth volume. The raw imaging data undergone the fiber pattern removal process (Figure 30b) and the SR-GAN model processing (Figure 30c). Then, the tissue image was reconstructed used the HR sub-images and is shown in Figure 31a. We calculated the depth map of the imaged tissue fiber by deriving the disparities between every two sub-images [93], [94] and labeled the object feature at different depths with pseudo colormap (Figure 31b). The 3D view of tissue paper with depth information is visualized in Figure 32.

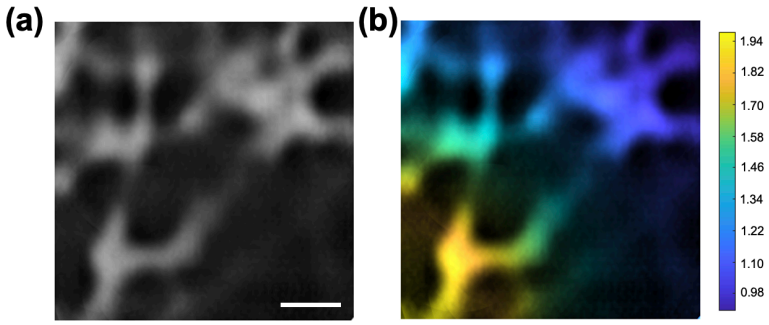

Figure 31. Fluorescent tissue fiber imaging and depth map.

(a) Reconstructed tissue fiber image (cropped). (b) 2D Depth map. Scale bar: 200 μm.

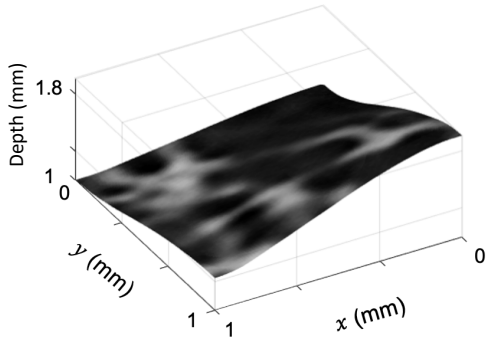

Figure 32. Depth map 3D visualization.

3.6 Evaluation and summary

The reconstruction process also reduces the resolution to a small extent. We measured the resolution of the LR and synthesized HR sub-images, the resolution before and after reconstruction, the resolution of reconstructed object images with and without the super resolution processing by the trained GAN model, and compared the resolution to the free-space light field system with the same paradigm. It is found that the resolution of Flex-LFE sub-image improved more than twice, from 45.11 μm to 20.36 μm by applying the SR model, close to the resolution of HR-LF sub-image which is 15.58 μm.

Table 4. Resolution comparisons of free-space (normal), fiber-based LF (Flex-LFE) systems and fiber-based LF combined with SR-GAN.

Resolution (μm)	Normal LF	Fiber LF	Fiber LF (SR-GAN)
LF sub-image	15.58	45.11	20.36
Reconstructed image	18.30	53.49	27.74

In terms of reconstructed object image, without applying SR model, the object imaged by the fiber bundle only has a resolution of 53.49 μm. This can be considered very low when compared to the reconstructed free-space LF image which has a resolution of 18.30 μm. With the well-trained SR-GAN model, the big resolution gap (~35 μm) can be effectively reduced, in real time. The resulted Flex-LFE reconstruction image reduced the resolution difference to 9.44 μm, less than 1/3 of the initial gap.

In summary, we developed the Flex-LFE imaging system with high resolution and 3D imaging capability for endoscopic imaging. The intrinsic limitation of fiber bundle which is low in imaging pixel numbers was solved by training a deep neural network, SR-GAN. Flex-LFE system can retrieve the depth information by acquiring 70 views of the imaged sample. These advantages make Flex-LFE versatilely useful in 3D assessment of tissue lesions in real time. Although the current system has been developed on a benchtop setup, the proposed method has the potential to be adapted for use in clinical endoscopic applications, such as gastroscopy and enteroscopy.

Chapter 4 Optical Coherence Tomography

Optical coherence tomography (OCT), a noninvasive three-dimensional (3D) imaging tool, has been widely used in both basic and translational biomedical sciences [95], [96], [97], [98]. Despite significant advances, to acquire 3D images, most current OCT devices require extensive scanning, either in the spatial domain or the spectral domain [99], [100]. The scanning mechanism introduces a trade-off between the imaging speed and image signal-to-noise ratio (SNR), which is particularly problematic for dynamic imaging where the motion of the object can easily blur the image [101], [102], [103], [104], [105].

4.1 Spectral-domain OCT

OCT generates cross-sectional images of a sample by measuring backscattered light using interferometry. The foundation of optical signal detection is low-coherence interferometry (LCI). Interferometry involves measuring the electric field of light backscattered from two paths that interfere with each other. Michelson interferometer is a classic type of interferometry, illustrated in Figure 33a. In this setup, a beam splitter divides the light source into two paths: the reference arm, which has a known time delay, and the sample arm, which contains the sample or tissue. Using low-coherent light (Figure 33b), interference occurs only when the optical path length difference between the reference and sample arms matches the coherence length of the light source. There are two main types of OCT: time-domain OCT (TD-OCT) and Fourier-domain OCT (FD-OCT).

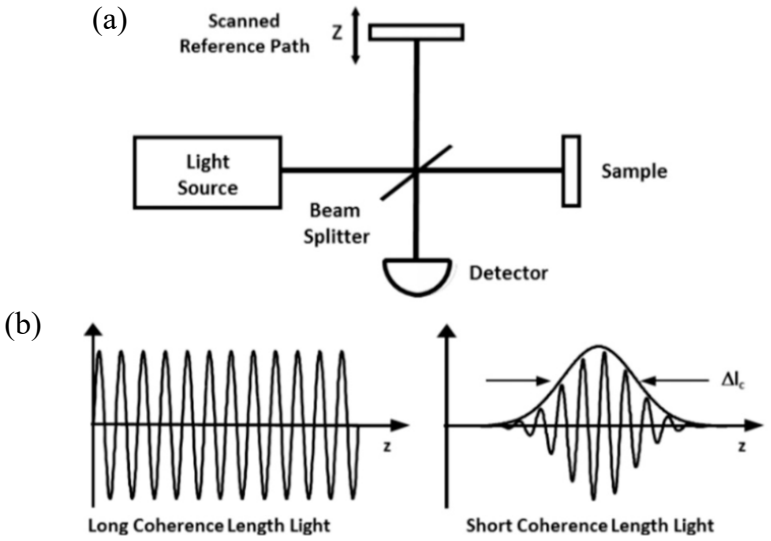

Figure 33. (a) Illustration of a Michelson interferometer. (b) Comparison of perfectly coherent light and low-coherent light. Δl_c is coherence length of light. Adapted from [49].

Spectral-domain OCT is one category of FD-OCT that capable of collecting signals from all depth of the sample throughout the entire acquisition and inherently more sensitive than a time-domain OCT [106], [107], [108]. We previously demonstrated snapshot full-field spectral-domain OCT based on image mapping spectrometry (IMS) which enables high-speed 3D microscopic imaging [109], [110], [111]. By slicing a two-dimensional (x-λ) OCT interferogram in the spatial domain using a custom multifaceted micromirror array followed by dispersing the line images as a spectrum, our proof-of-concept device can capture a 200 μm× 200 μm × 10 μm volume at a rate up to 5 Hz. However, built on a fixed optical architecture, this device suffers from a low spectral resolution—given 480 spatial samplings, the number of spectral bins is limited to 40, leading to a ~ 5 nm spectral resolution and only a 10 μm depth range in the OCT image. The shallow imaging

depth restricts the system from imaging biological tissues. Moreover, the multifaceted micromirror array in the IMS is costly to fabricate, hindering its accessibility to general labs.

4.2 Spatial light modulator (SLM)

Rather than using an optically fabricated micromirror array [104], [105], [109], we used a phase-only spatial light modulator (SLM) to modulate the incident wavefront in a programmed manner. For example, by displaying a 1D array of linear phase patterns, we can make the SLM act as flat mirrors with varied tilts (Figure 34a), resembling the micromirror array in the original IMS [112], [113], [114].

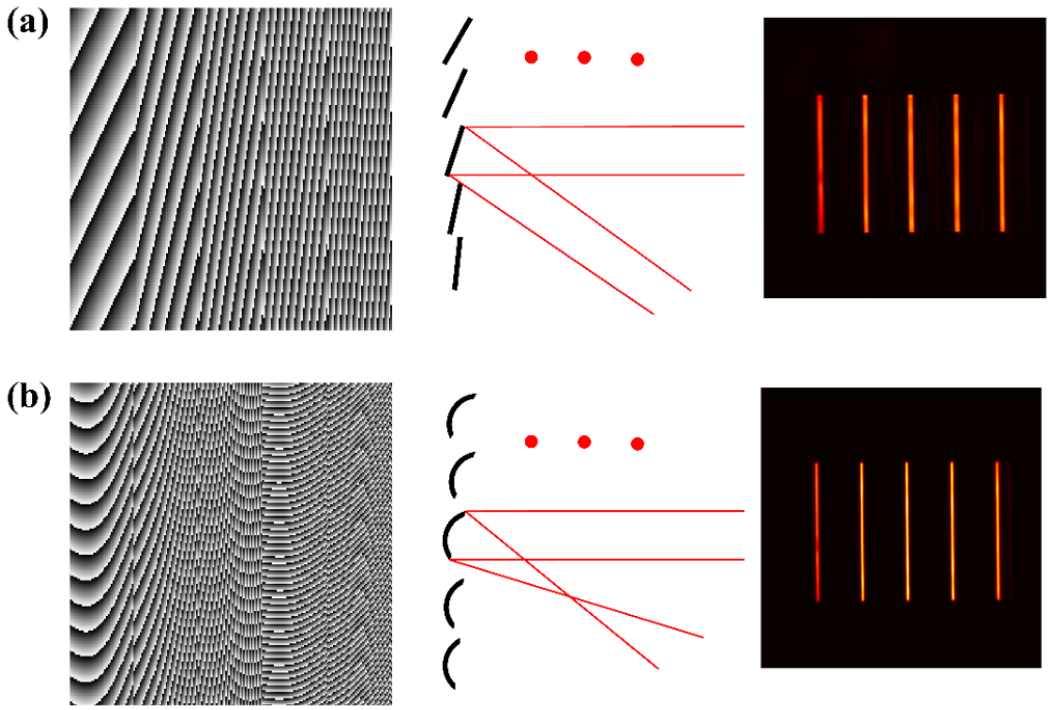

Figure 34. Programmable light guidance using a spatial light modulator (SLM).

(a) SLM acts as a 1D flat mirror array with varied tilts, (b) SLM acts as a 1D concave mirror array with varied tilts. From left to right, phase pattern displayed on the SLM, equivalent mirror array configuration, resultant image slices on the camera.

Alternatively, when displaying a 1D array of linear phase patterns superimposed with quadratic phase patterns, the SLM functions as an array of tilted concave mirrors, focusing the sliced images and redirecting them to varied directions (Figure 34b). Such a programmable ability allows the SLM to provide a balanced resolution along the spatial, spectral, and temporal dimensions. When combining with OCT, the resultant system can image a 3D volume with either a high lateral resolution or a high axial resolution in a snapshot. The system can also achieve a high resolution along all spatial dimensions through a multi-shot acquisition strategy.

We developed a tunable image-mapping optical coherence tomography (TIM-OCT) by integrating the phase-only SLM with a full field spectral-domain OCT to address the current technical challenges, which can provide tailored imaging performance for a given application. The system design is presented in detail in the following section.

4.3 Tunable image-mapping optical coherence tomography (TIM-OCT)

The optical setup of TIM-OCT is shown in Figure 35. It consists of two sub-systems: a full-field spectral-domain OCT system and a tunable IMS based on SLM. In the OCT sub-system, we use a supercontinuum source (SuperK Fianium FIU-15, NKT Photonics) with a tunable wavelength selection unit as a light source. The illumination light is selected within the visible light range, for the later target ophthalmology imaging. We pass the light through a custom rotating diffuser and illuminate the sample to reduce the speckle noise from laser.

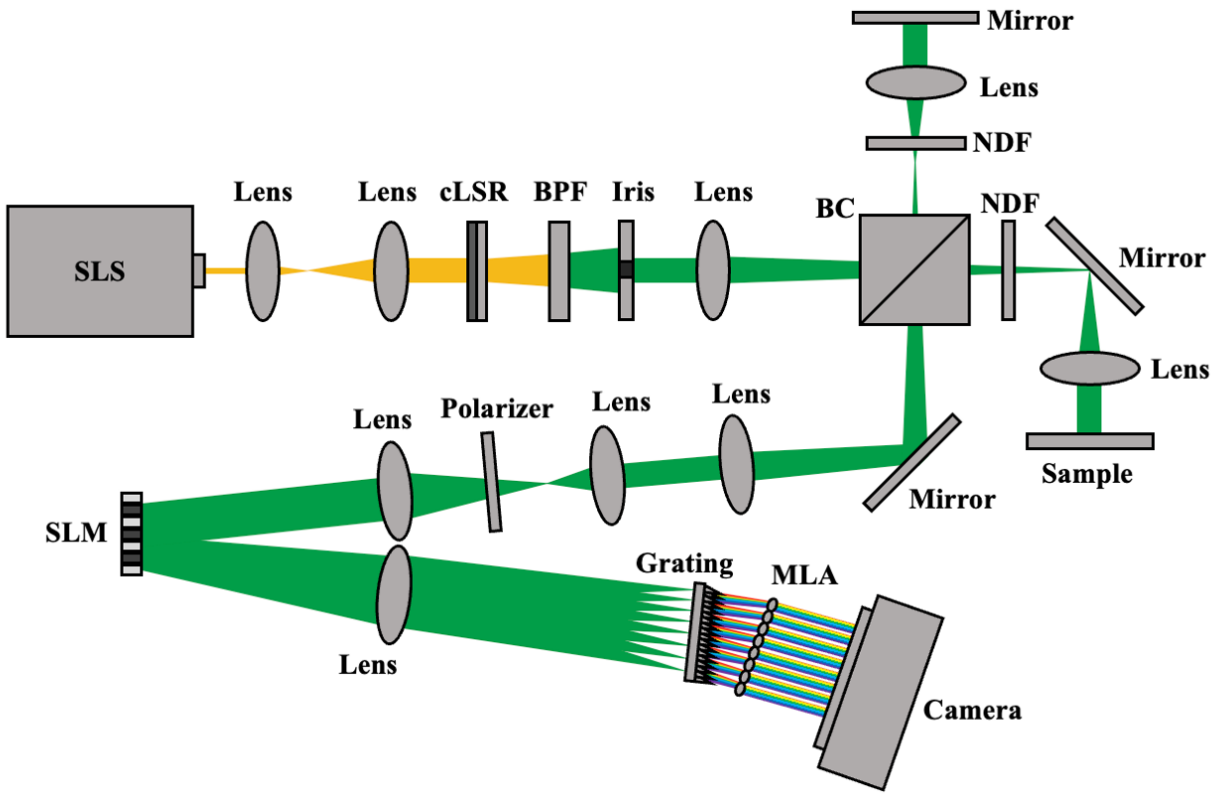

Figure 35. System configuration of TIM-OCT.

SLS: supercontinuum laser source; AL: aspherical lens; cLSR: customized laser speckle reducer; BPF: bandpass filter; BC: beam combiner; NDF: neutral density filter; SLM: spatial light modulator; MLA: microlens array.

The scattered light from the sample is collected by an achromatic doublet lens (focal length, 50 mm) and interfered with the light reflected from the reference arm mirror. The OCT interferogram is then passed to the tunable IMS sub-system. We first filter the light with a polarizer, and then project the image onto the phase-only SLM (HSP1920-488-800, Meadowlark Optics, USA), which has a resolution of 1920 × 1152 pixels and a sensor array size of 17.6 mm × 10.6 mm.

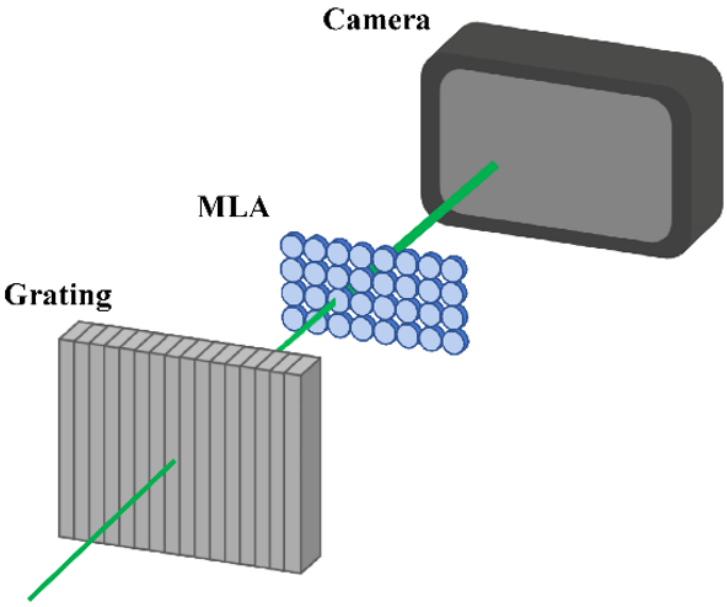

Figure 36. Optical setup of the grating, MLA, and camera.

We display various phase patterns on the SLM to make it function as an image mapper, analogous to that in the original IMS system. The light reflected from the SLM is then spectrally dispersed by a diffraction grating (GT50-03, ThorLabs, USA; 300 grooves/mm) and imaged by a custom micro-lens array (MLA) (4×8 microlenses; pitch 3 mm; focal length 30 mm), as shown in Figure 36. The final dispersed image slices (Figure 37) are captured by a CCD camera (hr455MCX, SVS-VISTEK, Germany).

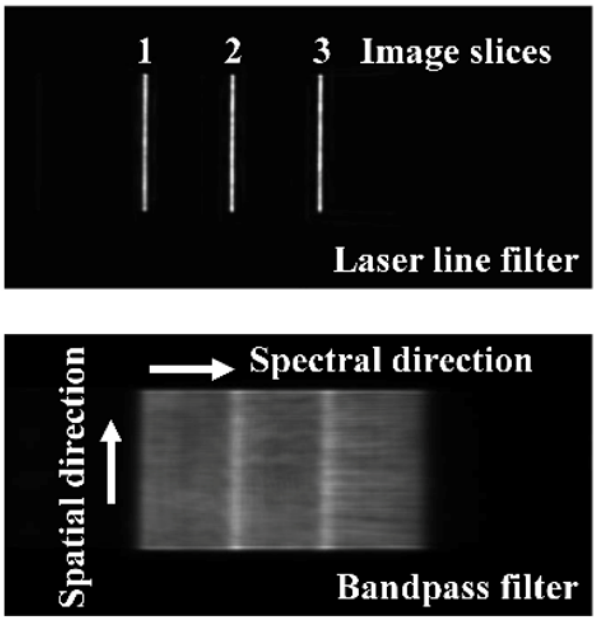

Figure 37. Dispersed image slices under monochromatic (top) and broadband illumination (bottom).

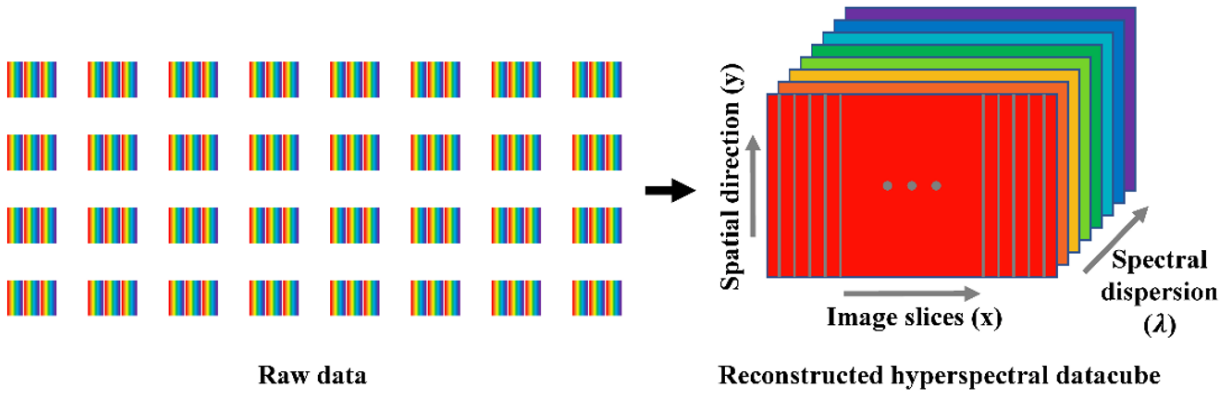

Figure 38. Construction of a hyperspectral datacube.

The raw data is a matrix of 2D image with x and λ dimensions on the detector screen. After the OCT data acquisition, we run a dimension rearrangement program based on the coordinates saved during the SLM calibration process to crop out all the MLA images and assemble them into a single 3D file, referred to as a datacube, as illustrated in Figure 38.

4.4 Tunable imaging capability

In TIM-OCT, the SLM acts as a mirror facet array, slicing the image into lines and redirecting them towards different microlenses on the array. We operate the SLM in three primary working modes:

Mode 1:

Snapshot high-lateral-resolution mode, where the SLM is programed to work as a flat mirror array with varied tilts (Figure 39a). The encoding scheme results in anisotropy in spatial samplings. The x-directional resolution is varied by the slit width on the SLM whereas the y-directional resolution remains the same. We divide the SLM into 192 narrow rectangular regions, each having an area of 92 μm (width) × 10.6 mm (length) and displaying a linear phase pattern along a specific direction. We group these SLM regions into six periodic blocks, each block having 32 linear phase patterns with varied orientations, as shown in Figure 39a and 39b.

The light reflected from each SLM region is superimposed with the corresponding phase pattern, which essentially directs the light beam towards a microlens on the array. Because phase patterns are repeated across periodic blocks, each microlens on the array collects light from a total of six SLM regions. The spacing between two adjacent reimaged SLM regions is equal to 32 × the width of a SLM region, leading to an effective spectral sampling of 32 after spectral dispersion. Within a single snapshot, the system can capture a spectral datacube (x, y, λ) of dimensions 192 × 155 × 32 (pixel × pixel × effective spectral sampling).

To avoid the crosstalk between the adjacent dispersed SLM region images, we filter the illumination using a 10 nm bandwidth filter centered at 550 nm. Given a 270 μm × 170 μm field-

of-view (FOV), the resultant OCT image has a lateral resolution of 2.8 μm and an axial resolution of 13.3 μm in air. The volumetric acquisition speed in the snapshot mode is solely dictated by the required exposure time and the camera frame rate (18 frames per second).

Mode 2:

Snapshot high-axial-resolution mode, where the SLM is programed to work as a concave mirror array with varied tilts Figure 39c. We divide the SLM into 32 wide rectangular regions, each having an area of 552 μm (width) × 10.6 mm (length) and displaying a linear phase pattern along a unique orientation and being superimposed with a quadratic phase. The light reflected from a SLM region is first focused into a narrow line (202 μm wide) and then redirected towards a microlens on the array. Because each microlens collects light from only one reimaged SLM region, the corresponding spectrum occupies the entire underlying space, leading to an effective spectral sampling of 160. This allows measurement of a spectral datacube (x, y, λ) of dimensions 32 × 155 × 160 (pixel × pixel × effective spectral sampling) in Figure 39c and 39d. The resultant system can acquire a much broader spectral bandwidth (80 nm) with a 0.46 nm spectral resolution. This combination with the OCT subsystem yields a lateral resolution of 16.8 μm (y-direction) and an axial resolution of 3.4 μm.

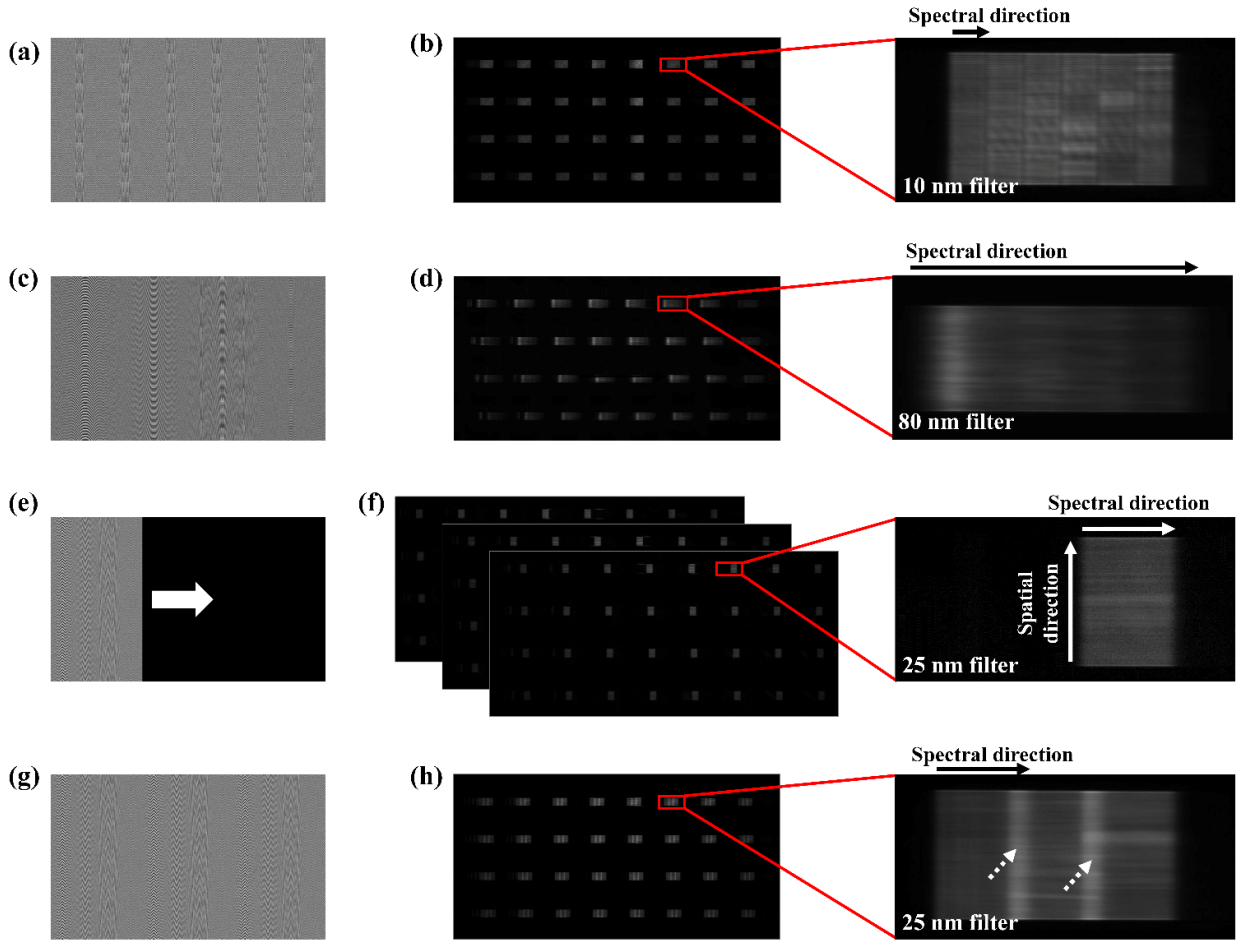

Figure 39. SLM patterns and respective raw camera images in different imaging modes.

(a)-(b) Mode 1: Snapshot high-lateral-resolution mode with 192 image slices and a 10 nm spectral bandwidth, (c)-(d) Mode 2: Snapshot high-axial-resolution mode with 32 image slices and a 80 nm spectral bandwidth, (e)-(f) Mode 3: Multi-shot acquisition mode with 96 image slices and a 25 nm spectral bandwidth, (g)-(h) Snapshot acquisition of 96 image slices with spectral crosstalk (arrow-pointed regions).

Mode 3:

Multi-shot acquisition mode. Mode 1 and 2 allow one to tune the spatial resolution along the lateral and axial directions for snapshot acquisition. In Mode 3, one can trade in the temporal resolution

for high spatial resolution through multi-shot acquisition. Rather than simultaneously functionalizing all SLM regions, we turn on a subset at a time and capture the resultant spectra in sequence. This increases the spacing between adjacent reimaged SLM regions per acquisition, thereby allowing measurement of a broader spectral range.

Figure 39e and 39f illustrates an example of a three-shot acquisition sequence of 96 SLM regions, with each shot capturing 32 line-spectra. This mode allows measurement of a spectral datacube (x, y, λ) of dimensions 96 × 155 × 54 (pixel × pixel × effective spectral sampling), leading to a 3D resolution of 5.6 μm × 3.4 μm × 10.6 μm in the OCT image. The volumetric imaging speed is 6 frames per second, one-third of the camera frame rate. The illuminating laser power varies by imaging targets from 160 μW (in-vivo mouse cornea) to 1.4 mW (ex-vivo standard target). The resolutions of the current system are limited by the pixel sampling of the SLM rather than the optical diffraction. The pixel sampling rate can be further improved by using high-resolution SLMs [115], [116], [117].

Table 5. Comparison of imaging parameters of TIM-OCT under three primary modes.

	Mode 1	Mode 2	Mode 3
Image slices	192 (6x32)	32	96
Slice dimension	92 μm × 10.6 mm	552 μm × 10.6 mm	184 μm × 10.6 mm
Datacube (x, y, λ)	**192** × 155 × 32	32 × 155 × **160**	**96** × 155 × **54**

Another mode for snapshot acquisition involves 96 image slices with a 25 nm bandpass filter (Figure 39g and 39h). The arrow-indicated regions highlight the crosstalk regions of spectral dispersion. In this case, the snapshot OCT imaging cannot utilize the whole 25 nm spectral range.

4.5 Imaging results

To demonstrate the system's performance in Mode 1 and 2, we imaged a 1951 negative USAF target (group 5, element 2-3) in air. The reconstruction of a spectral $I(x, y, \lambda)$ datacube from the raw measurement utilized a re-mapping algorithm that is described elsewhere [118], [119], [120]. Once the $I(x, y, \lambda)$ datacube is correctly assembled, we apply a non-uniform discrete Fourier transform (NUDFT) [109] to generate the desired image of 3D sample structure $I(x, y, \lambda)$, as illustrated in Figure 38. In TIM-OCT, we use NUDFT to correct for the nonlinearity of the spectral dispersion with a limited number of spectral samplings and alleviate the sensitivity roll-off at depths [121], [122]. Each location on the sample surface is associated with a separate interferogram, $I(x_i, y_j, \lambda)$, with i and j corresponding to pixel indices in the x- and y-dimensions. Conversion of interferograms to A-lines will require re-sampling of raw data from the wavelength λ to the wavenumber k domain ($k = 2\pi/\lambda$) before Fourier transformation to z-space. Repeating the procedure above at each transverse location yields a volumetric image $I(x, y, \lambda)$.

Figure 40a and 40b show the *en-face* and cross-sectional OCT images in the high-lateral-resolution imaging mode, where the *en-face* image presents a high quality while the cross-sectional image is pixelated due to a lack of spectral sampling. The lateral and axial resolutions are measured to be 2.8 μm and 13.3 μm, respectively. In contrast, when the system is operated in the high-axial resolution mode, it yields a reduced-quality *en-face* image (Figure 40c) but a sharp cross-sectional image as can be seen in Figure 40d. The resultant lateral and axial resolutions are 16.8 μm and 3.4 μm, respectively. It is worth noting that we can switch between the two snapshot working modes simply by changing the phase patterns on the SLM without moving parts.

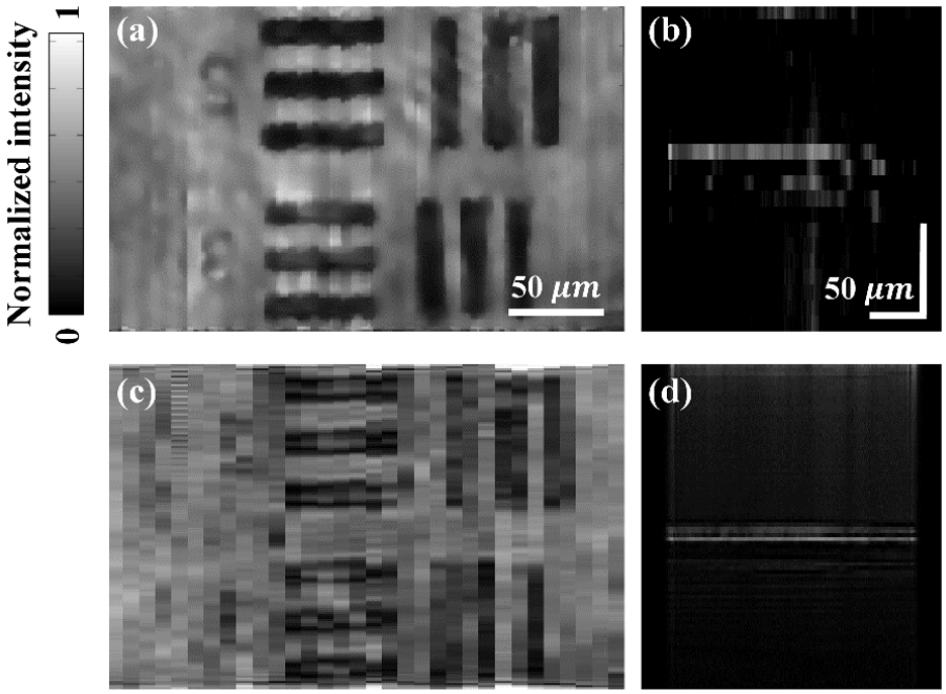

Figure 40. TIM-OCT of a negative USAF target with tunable resolutions. (a) *En-face* image, and (b) cross-sectional image in the high-lateral-resolution mode. (c) *En-face* image, and (d) cross-sectional image in the high-axial-resolution mode.

Figure 41a shows the depth-directional intensity profile along the vertical axis of Figure 40b, while Figure 41b depicts the depth-directional intensity profile along the vertical axis of Figure 40d. A comparison of these profiles reveals that TIM-OCT achieves a significantly higher axial resolution in the mode 2 snapshot imaging.

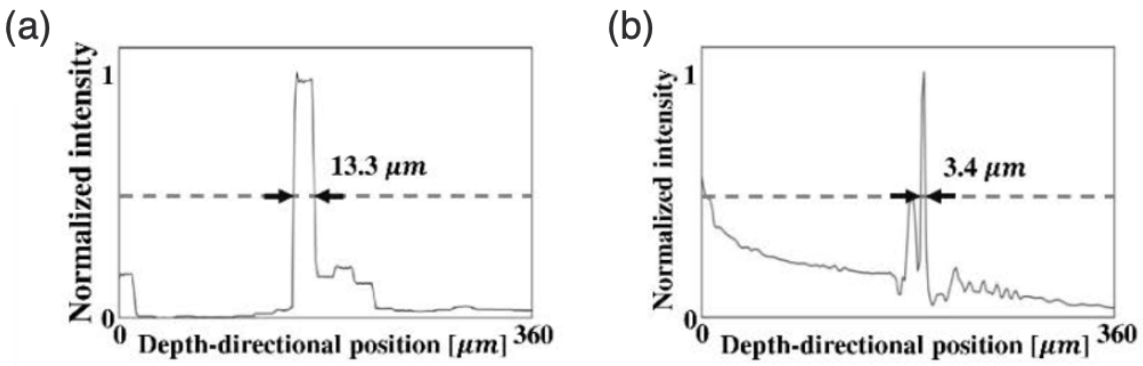

Figure 41. Depth-directional intensity profile in the high-lateral-resolution mode (a) and in the high-axial-resolution mode (b).

4.6 Mouse imaging

We further evaluated TIM-OCT by performing in vivo imaging of mouse corneal structures in both snapshot and multi-shot modes. The mouse experiment in this study was conducted in accordance with the guidelines of the UCLA Institutional Animal Care and Use Committee (No. ARC-2021-130) under an approved protocol. A Balb/c mouse (8 weeks old, female) was anesthetized using 0.8% isoflurane delivered at 1 L/min via a snout covering nozzle, as posed in Figure 42b. The mouse was placed on an electronic heating pad to maintain body temperature (Figure 42a), and the mouse condition was constantly monitored during the experiment. A three-axis translational stage combined with two rotational stages is used to precisely control the positioning of the mouse eye.

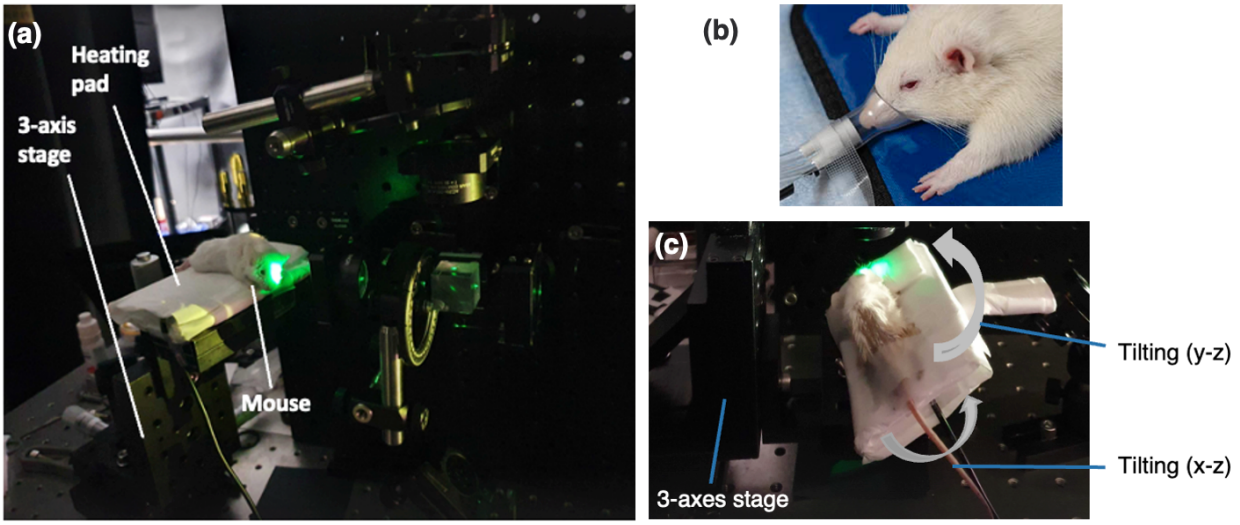

Figure 42. TIM-OCT mouse cornea imaging setup.

(a) Mouse during imaging. (b) Anesthesia using isoflurane via a snout covering nozzle. (c) Illustration of the degree of mouse eye position control.

Figure 43 illustrates three different working modes of TIM-OCT in mouse cornea imaging. We first acquired a corneal image in the snapshot high-lateral-resolution mode, which allows only a 10 nm spectral bandwidth. The snapshot acquisition freezes the motion, making it particularly useful for eye imaging. However, in the corresponding cross-sectional image (Figure 43a), the epithelium and stromal layers are hardly visible due to a low axial resolution.

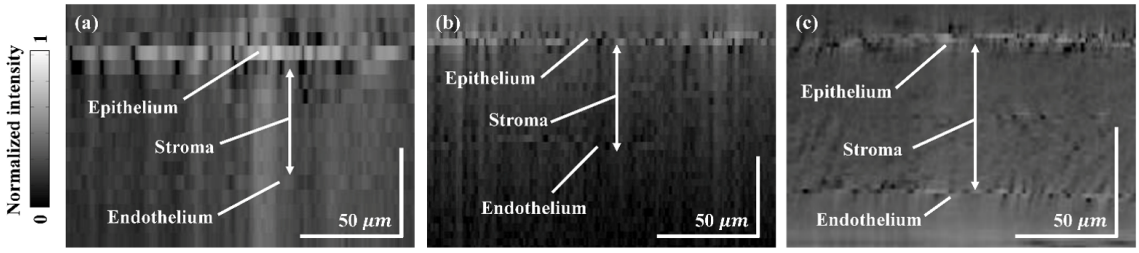

Figure 43. In vivo mouse cornea imaging using snapshot and multi-shot TIM-OCT acquisition. (a) Snapshot OCT cross-section image, (b) Three-shot OCT cross-section image, (c) Slit-scan OCT cross-section image.

Next, we switched to the multi-shot acquisition mode by sequentially capturing the dispersed image slices in three periodic blocks. This increased the spectral bandwidth to 25 nm. The resultant cross-sectional intensity image is shown in Figure 43b, showing an increased visibility of the corneal layers. Finally, we sequentially scanned a "slit" region on the SLM across the FOV, mimicking the conventional push-broom imaging spectrometers. This led to more extensive scanning but allowed for capturing the full spectral range of 80 nm. The resultant cross-sectional image of the epithelium and stromal region is shown in Figure 43c. In the slit-scanning mode, it provides the most resolving power for imaging the corneal layers. Although the slit-scan mode takes more time for data collection compared to the snapshot mode, it still demonstrates superior efficiency over point-scanning OCTs. Figure 44 presents four *en-face* images captured at different depths in Figure 43c. The observed in vivo corneal structure is consistent with previous literatures [123], [124], [125].

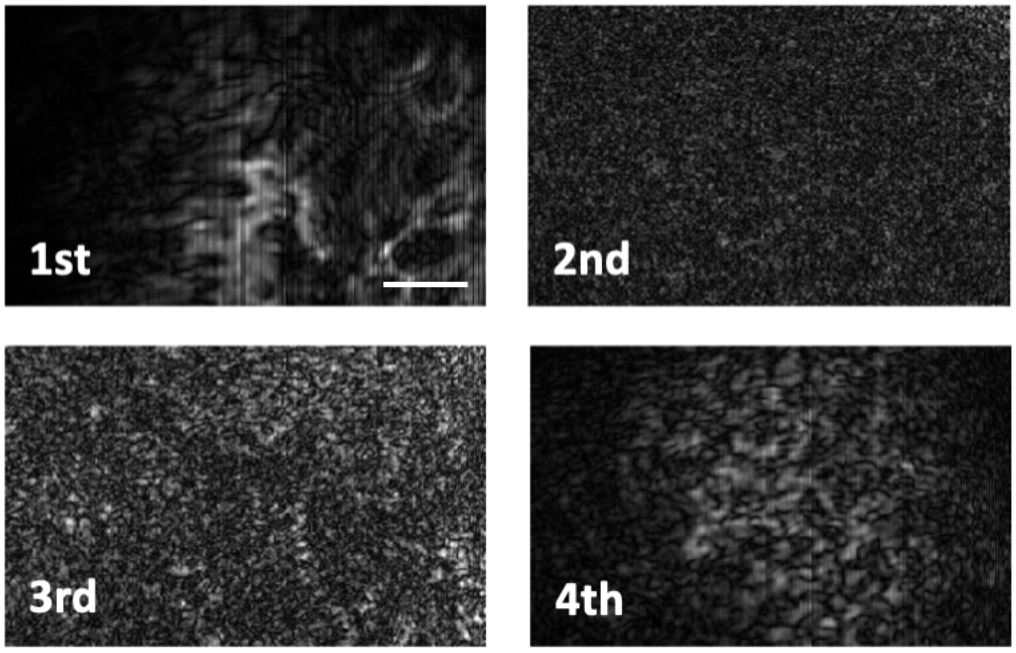

Figure 44. *En-face* images at four depths of Figure 22c. Scale bar: 50 μm.

4.7 TIM-OCT discussion

We present tunable image-mapping optical coherence tomography (TIM-OCT), which can provide optimized imaging performance for a given application by using a programmable phase-only spatial light modulator in a low-coherence full-field spectral-domain interferometer. The resultant system enables high lateral or a high axial resolution in a snapshot without requiring moving hardware components. Alternatively, the system can achieve high resolution across all dimensions through a multiple-shot acquisition. We evaluated TIM-OCT by imaging both standard USAF targets and mouse cornea in vivo.

Compared to our previously developed full-field spectral-domain OCT based on IMS, the SLM can effectively display a variety of reflection patterns without altering the mapping mirrors. Therefore, the SLM-based TIM-OCT offers high versatility, enabling the optimization of spectral channels and spatial pixel numbers for high-speed 3D snapshot imaging across various applications. We did a translational study on applying the TIM-OCT system to the human retina imaging. By virtue of its depth imaging capability, the human retina wad prepared as flatmount slides rather than cross-sections in the hyperspectral imaging, as shown in Figure 45. The red circle indicates the imaging region near the optic disc (OD).

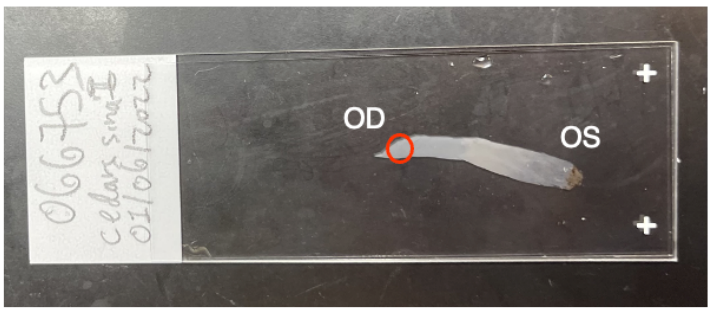

Figure 45. The human retina flatmount slide in spectral OCT imaging.

Spectroscopic OCT (SOCT) analysis was conducted after imaging the retina flatmount with TIM-OCT. By applying the short-time Fourier transform to the interferogram $I(x, y, \lambda)$, the spectral content can be computed through software without the need to modify the OCT system. The cross-sectional image of retina is reconstructed in Figure 46a. An NFT structure was identified at a depth of approximately 50 μm under the tissue surface. The computed spectrogram is shown in Figure 46b. The red plot in Figure 46d represents the corresponding NFT spectra. A control region was plotted by averaging the spectra information at the black arrow pointed area. The spectral difference of the plot is consistent with our findings in hyperspectral imaging.

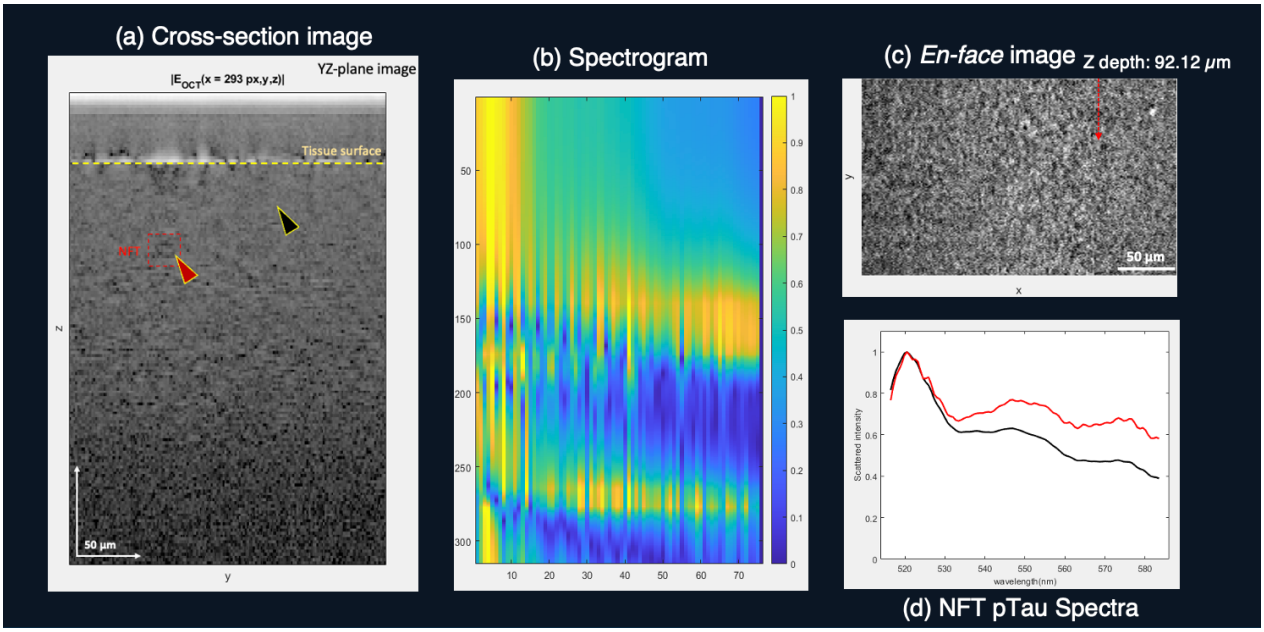

Figure 46. Human retina imaging using TIM-OCT and spectroscopic OCT analysis.

In conclusion, TIM-OCT represents a novel category of OCT devices that can be operated in multiple imaging modes, offering tailored imaging performance for specific objects. The snapshot acquisition modes effectively freeze motion, making it particularly advantageous for eye imaging.

The resolution of the current system is limited by the pixel sampling of the SLM rather than optical diffraction. This limitation can be addressed by utilizing high-resolution SLMs to enhance the pixel sampling rate.

Chapter 5 Summary

Although optical imaging technologies have witnessed remarkable advancements over the past decades, there remains significant potential for AI-driven approaches to further enhance their performance and broaden their applicability. By integrating artificial intelligence with state-of-the-art imaging systems, it is possible to overcome many of the inherent limitations of conventional optical designs. This dissertation explores the synergy between computational methods and optical imaging modalities, demonstrating how AI can serve as a transformative tool to elevate high-dimensional imaging data analysis, imaging resolution, and diagnostic utility.

One of primary objectives of this work is to develop a deep learning based imaging platform capable of addressing critical challenges in the detection and classification of Alzheimer's disease (AD) biomarkers, specifically amyloidogenic 42-residue long ($A\beta_{42}$) alloform and phosphorylated tau (pTau). Hyperspectral imaging (HSI) is employed as a label-free imaging modality to identify and characterize the spectral signatures of $A\beta_{42}$ and pTau in human retinal tissues. The scattering spectral signature of Aβ was first identified ex vivo by More and Vince in 2015 [52], [126]. This work, to our knowledge, is the first report of the spectral signature of pTau in the human retina.

Our findings echo many pioneer works in the field. For instance, Xavier Hadoux et al. [20] discovered a significant difference in ocular reflectance among patients with and without moderate-to-high Aβ levels, and they confirmed their findings through imaging the paired brain samples.

However, all these previous studies lack a direct validation through immunostaining. Moreover, the distribution of $A\beta_{42}$ and pTau remains elusive in current imaging approaches. This research leverages generative adversarial networks (GANs) to transform the unstained hyperspectral data into histopathology-contrast images, offering an innovative approach and lay the groundwork to non-invasive, early-stage AD diagnosis [127].

The HSI prediction results are compared with two gold-standard methods, peroxidase-based immunostaining (DAB) and immunofluorescent staining, in quantifying Aβ and pTau deposits in retinal tissues. It demonstrates the feasibility of predicting their spatial distribution with high accuracy using deep learning. We anticipate that the proposed deep learning platform will serve as an alternative or complimentary approach, offering the significant advantage of substantially reducing the processing time required for histological analysis.

The second optical system presented in this dissertation is tunable image-mapping optical coherence tomography (TIM-OCT). OCT is a noninvasive three-dimensional imaging modality that has been widely used in translational biomedical sciences [94]. However, most OCT devices rely on extensive scanning in spatial or spectral domain to achieve depth-resolved visualization. The proposed TIM-OCT system integrates a phase-only SLM with spectral-domain OCT[128] to enable tailored imaging performance of several snapshot and multi-shot modes. Its snapshot imaging capability effectively mitigates the challenges associated with rapid eye motion, making it suitable for dynamic assessments. Consequently, TIM-OCT represents a step closer to the goal of translating our findings in AD by facilitating in vivo retinal imaging.

Additionally, a flexible light field endoscope (Flex-LFE) is introduced for depth-resolved endoscopic imaging. By leveraging deep learning based super-resolution techniques[129], the

system addresses the inherent hardware limitations of fiber imaging, enabling high-resolution image reconstruction within a compact and adaptable framework.

This work highlights the transformative potential of AI-driven imaging systems in addressing the data complexities of optical imaging. The integration of computational techniques and advanced imaging modalities lays the groundwork for innovations in precision diagnostics, particularly in the early detection and management of neurodegenerative diseases like Alzheimer's. Future work will focus on further optimization of the imaging systems, including the scanning of diverse retinal strips to quantify and potentially differentiate individuals with high and low levels of AD pathology. Additional efforts will involve imaging fresh brain tissues and developing spectroscopic OCT techniques for in vivo imaging of transgenic AD-model mice, with the aim of advancing our understanding of AD pathology and enhancing diagnostic capabilities.

Appendix A

The neuropathologically confirmed AD patients used for spectral signature analysis and transformation network training. Retina cross-sections stained for Amyloid beta 42 (Ab 12F4) and pS396-Tau (Ab PS396). Postmortem interval (PMI) values of tissue collection were also recorded.

Donor information	Patient #1	Patient #4	Patient #5
Age (year)	90	81	85
Gender	Female	Female	Female
Race	White	Hispanic	White
Premortem diagnosis	AD	AD	Dementia
MMSE score	9	None	None
CDR score	2	3	3
PMI (hour)	9	7.5	8.5
Final diagnosis	AD	AD	AD
Braak stage	V	VI	V
ADNC: Aβ plaque (A) score, NFT (B) stage and neuritic plaque (C) score	A2, B3, C3	A3, B3, C3	A3, B3, C3
HSI imaged slide #	#05	#12	#04
Fluorescent stained slide #	12F4 & PS396: #06	12F4 & PS396: #13, #12	12F4 & PS396: #03
DAB stained slide #	12F4: #05, #08 PS396: #04	12F4: #11 PS396: #14	12F4: #05 PS396: #04, #01
Transformation model	DAB-$A\beta_{42}$	Fluo-$A\beta_{42}$ Fluo-pS396-Tau	DAB-pS396-Tau

The neuropathologically confirmed patients used for validation of immunofluorescence and DAB imaging:

Neuropathological diagnosis	Patient #	Age (year)	Gender	Race
AD	#1	90	Female	White
AD	#2	92	Female	Hispanic
MCI	#1	93	Male	White
MCI	#2	87	Female	White
MCI	#3	88	Male	White
CN	#1	72	Male	White
CN	#2	84	Male	White
CN	#3	95	Female	White
CN	#4	77	Male	White
CN	#5	95	Female	White

Appendix B

The number of image patches used in training for the four transformation models.

Transformation model	DAB-pS396-Tau	DAB-Aβ_{42}	Fluo-pS396-Tau	Fluo-Aβ_{42}
# of training patches	16528	29630	13501	13706
# of validation patches	360	650	300	300
# of test patches	398	713	324	330

Chapter 6 References

[1] S. Chen *et al.*, "The global macroeconomic burden of Alzheimer's disease and other dementias: estimates and projections for 152 countries or territories," *Lancet Glob Health*, vol. 12, no. 9, pp. e1534–e1543, Sep. 2024, doi: 10.1016/S2214-109X(24)00264-X.

[2] M. Koronyo-Hamaoui *et al.*, "Identification of amyloid plaques in retinas from Alzheimer's patients and noninvasive in vivo optical imaging of retinal plaques in a mouse model," *Neuroimage*, vol. 54 Suppl 1, no. SUPPL. 1, Jan. 2011, doi: 10.1016/J.NEUROIMAGE.2010.06.020.

[3] U. Habiba *et al.*, "Age-Specific Retinal and Cerebral Immunodetection of Amyloid-β Plaques and Oligomers in a Rodent Model of Alzheimer's Disease," *Journal of Alzheimer's Disease*, vol. 76, no. 3, pp. 1135–1150, Jan. 2020, doi: 10.3233/JAD-191346.

[4] A. Toosi, A. G. Bottino, B. Saboury, E. Siegel, and A. Rahmim, "A Brief History of AI: How to Prevent Another Winter (A Critical Review)," *PET Clin*, vol. 16, no. 4, pp. 449–469, Oct. 2021, doi: 10.1016/j.cpet.2021.07.001.

[5] Y. Sun *et al.*, "Real-time three-dimensional histology-like imaging by label-free nonlinear optical microscopy," *Quant Imaging Med Surg*, vol. 10, no. 11, pp. 2177190–2172190, Nov. 2020, doi: 10.21037/QIMS-20-381.

[6] Y. Koronyo *et al.*, "Retinal amyloid pathology and proof-of-concept imaging trial in Alzheimer's disease," *JCI Insight*, vol. 2, no. 16, Aug. 2017, doi: 10.1172/JCI.INSIGHT.93621.

[7] A. Grimaldi *et al.*, “Neuroinflammatory Processes, A1 Astrocyte Activation and Protein Aggregation in the Retina of Alzheimer’s Disease Patients, Possible Biomarkers for Early Diagnosis,” *Front Neurosci*, vol. 13, p. 925, Sep. 2019, doi: 10.3389/FNINS.2019.00925/BIBTEX.

[8] J. den Haan *et al.*, “Amyloid-beta and phosphorylated tau in post-mortem Alzheimer’s disease retinas,” *Acta Neuropathologica Communications 2018 6:1*, vol. 6, no. 1, pp. 1–11, Dec. 2018, doi: 10.1186/S40478-018-0650-X.

[9] H. Shi *et al.*, “Identification of early pericyte loss and vascular amyloidosis in Alzheimer’s disease retina,” *Acta Neuropathol*, vol. 139, no. 5, pp. 813–836, May 2020, doi: 10.1007/S00401-020-02134-W/FIGURES/6.

[10] “2021 Alzheimer’s disease facts and figures,” *Alzheimers Dement*, vol. 17, no. 3, pp. 327–406, Mar. 2021, doi: 10.1002/ALZ.12328.

[11] H. Shi *et al.*, “Retinal Vasculopathy in Alzheimer’s Disease,” *Front Neurosci*, vol. 15, Sep. 2021, doi: 10.3389/FNINS.2021.731614.

[12] O. M. Dumitrascu *et al.*, “Retinal Venular Tortuosity Jointly with Retinal Amyloid Burden Correlates with Verbal Memory Loss: A Pilot Study,” *Cells*, vol. 10, no. 11, Nov. 2021, doi: 10.3390/CELLS10112926.

[13] N. J. Hart, Y. Koronyo, K. L. Black, and M. Koronyo-Hamaoui, “Ocular indicators of Alzheimer’s: exploring disease in the retina,” *Acta Neuropathologica 2016 132:6*, vol. 132, no. 6, pp. 767–787, Sep. 2016, doi: 10.1007/S00401-016-1613-6.

[14] C. Schön *et al.*, “Long-Term In Vivo Imaging of Fibrillar Tau in the Retina of P301S Transgenic Mice,” *PLoS One*, vol. 7, no. 12, p. e53547, Dec. 2012, doi: 10.1371/JOURNAL.PONE.0053547.

[15] C. La Morgia *et al.*, “Melanopsin retinal ganglion cell loss in Alzheimer disease,” *Ann Neurol*, vol. 79, no. 1, pp. 90–109, Jan. 2016, doi: 10.1002/ANA.24548.

[16] S. Lee *et al.*, “Amyloid Beta Immunoreactivity in the Retinal Ganglion Cell Layer of the Alzheimer’s Eye,” *Front Neurosci*, vol. 14, p. 758, Jul. 2020, doi: 10.3389/FNINS.2020.00758/BIBTEX.

[17] N. Schultz, E. Byman, and M. Wennström, “Levels of Retinal Amyloid-β Correlate with Levels of Retinal IAPP and Hippocampal Amyloid-β in Neuropathologically Evaluated Individuals,” *Journal of Alzheimer’s Disease*, vol. 73, no. 3, pp. 1201–1209, Jan. 2020, doi: 10.3233/JAD-190868.

[18] Y. Qiu, T. Jin, E. Mason, and M. C. W. Campbell, “Predicting Thioflavin Fluorescence of Retinal Amyloid Deposits Associated With Alzheimer’s Disease from Their Polarimetric Properties,” *Transl Vis Sci Technol*, vol. 9, no. 2, pp. 47–47, Jan. 2020, doi: 10.1167/TVST.9.2.47.

[19] K. J. Cao *et al.*, “ARCAM-1 Facilitates Fluorescence Detection of Amyloid-Containing Deposits in the Retina,” *Transl Vis Sci Technol*, vol. 10, no. 7, Jun. 2021, doi: 10.1167/TVST.10.7.5.

[20] X. Hadoux *et al.*, “Non-invasive in vivo hyperspectral imaging of the retina for potential biomarker use in Alzheimer’s disease,” *Nature Communications 2019 10:1*, vol. 10, no. 1, pp. 1–12, Sep. 2019, doi: 10.1038/s41467-019-12242-1.

[21] U. Habiba *et al.*, "Detection of retinal and blood Aβ oligomers with nanobodies," *Alzheimer's & Dementia: Diagnosis, Assessment & Disease Monitoring*, vol. 13, no. 1, p. e12193, Jan. 2021, doi: 10.1002/DAD2.12193.

[22] A. Grimaldi *et al.*, "Inflammation, neurodegeneration and protein aggregation in the retina as ocular biomarkers for Alzheimer's disease in the 3xTg-AD mouse model," *Cell Death Dis*, vol. 9, no. 6, Jun. 2018, doi: 10.1038/S41419-018-0740-5.

[23] J. Ngolab *et al.*, "Feasibility study for detection of retinal amyloid in clinical trials: The Anti-Amyloid Treatment in Asymptomatic Alzheimer's Disease (A4) trial," *Alzheimer's & Dementia: Diagnosis, Assessment & Disease Monitoring*, vol. 13, no. 1, p. e12199, Jan. 2021, doi: 10.1002/DAD2.12199.

[24] O. M. Dumitrascu *et al.*, "Sectoral segmentation of retinal amyloid imaging in subjects with cognitive decline," *Alzheimer's & Dementia: Diagnosis, Assessment & Disease Monitoring*, vol. 12, no. 1, p. e12109, Jan. 2020, doi: 10.1002/DAD2.12109.

[25] C. R. Jack *et al.*, "NIA-AA Research Framework: Toward a biological definition of Alzheimer's disease," *Alzheimers Dement*, vol. 14, no. 4, pp. 535–562, Apr. 2018, doi: 10.1016/J.JALZ.2018.02.018.

[26] A. Sidiqi *et al.*, "In vivo Retinal Fluorescence Imaging With Curcumin in an Alzheimer Mouse Model," *Front Neurosci*, vol. 0, p. 713, Jul. 2020, doi: 10.3389/FNINS.2020.00713.

[27] K. Tadokoro *et al.*, "Retinal Amyloid Imaging for Screening Alzheimer's Disease," *Journal of Alzheimer's Disease*, vol. 83, no. 2, pp. 927–934, Jan. 2021, doi: 10.3233/JAD-210327.

[28] F. Chibhabha *et al.*, "Non-invasive optical imaging of retinal Aβ plaques using curcumin loaded polymeric micelles in APPswe/PS1ΔE9 transgenic mice for the diagnosis of Alzheimer's disease," *J Mater Chem B*, vol. 8, no. 33, pp. 7438–7452, Aug. 2020, doi: 10.1039/D0TB01101K.

[29] S. M. Barton *et al.*, "Inhalable Thioflavin S for the Detection of Amyloid Beta Deposits in the Retina," *Molecules*, vol. 26, no. 4, Feb. 2021, doi: 10.3390/MOLECULES26040835.

[30] J. P. Vit *et al.*, "Color and contrast vision in mouse models of aging and Alzheimer's disease using a novel visual-stimuli four-arm maze," *Scientific Reports 2021 11:1*, vol. 11, no. 1, pp. 1–19, Jan. 2021, doi: 10.1038/s41598-021-80988-0.

[31] Y. Koronyo, B. C. Salumbides, K. L. Black, and M. Koronyo-Hamaoui, "Alzheimer's disease in the retina: imaging retinal aβ plaques for early diagnosis and therapy assessment," *Neurodegener Dis*, vol. 10, no. 1–4, pp. 285–293, Apr. 2012, doi: 10.1159/000335154.

[32] A. M. Siddiqi *et al.*, "Use of hyperspectral imaging to distinguish normal, precancerous, and cancerous cells," *Cancer Cytopathol*, vol. 114, no. 1, pp. 13–21, Feb. 2008, doi: 10.1002/CNCR.23286.

[33] S. V. Panasyuk *et al.*, "Medical hyperspectral imaging to facilitate residual tumor identification during surgery," *http://dx.doi.org/10.4161/cbt.6.3.4018*, vol. 6, no. 3, pp. 439–446, 2007, doi: 10.4161/CBT.6.3.4018.

[34] K. Masood, N. Rajpoot, M. N.-Ann. BMVA, and undefined 2008, "Spatial analysis for colon biopsy classification from hyperspectral imagery," *Citeseer*, vol. 2008, no. 4, pp. 1–16, 2008.

[35] D. T. Dicker *et al.*, “Differentiation of normal skin and melanoma using high resolution hyperspectral imaging,” *Cancer Biol Ther*, vol. 5, no. 8, pp. 1033–1038, 2006, doi: 10.4161/CBT.5.8.3261.

[36] T. E. Renkoski, U. Utzinger, and K. D. H. M.D., “Wide-field spectral imaging of human ovary autofluorescence and oncologic diagnosis via previously collected probe data,” *https://doi.org/10.1117/1.JBO.17.3.036003*, vol. 17, no. 3, p. 036003, Mar. 2012, doi: 10.1117/1.JBO.17.3.036003.

[37] H. Akbari *et al.*, “Hyperspectral imaging and quantitative analysis for prostate cancer detection,” *https://doi.org/10.1117/1.JBO.17.7.076005*, vol. 17, no. 7, p. 076005, Jul. 2012, doi: 10.1117/1.JBO.17.7.076005.

[38] D. M. Roblyer *et al.*, “Multispectral optical imaging device for in vivo detection of oral neoplasia,” *https://doi.org/10.1117/1.2904658*, vol. 13, no. 2, p. 024019, Mar. 2008, doi: 10.1117/1.2904658.

[39]. Ja F H Goetz *et al.*, “Detecting brain tumor in pathological slides using hyperspectral imaging,” *Biomedical Optics Express, Vol. 9, Issue 2, pp. 818-831*, vol. 9, no. 2, pp. 818–831, Feb. 2018, doi: 10.1364/BOE.9.000818.

[40] S. Kiyotoki *et al.*, “New method for detection of gastric cancer by hyperspectral imaging: a pilot study,” *https://doi.org/10.1117/1.JBO.18.2.026010*, vol. 18, no. 2, p. 026010, Feb. 2013, doi: 10.1117/1.JBO.18.2.026010.

[41] E. L. P. Larsen, L. L. Randeberg, A. Aksnes, L. O. Svaasand, E. Olstad, and O. A. Haugen, “Hyperspectral imaging of atherosclerotic plaques in vitro,”

https://doi.org/10.1117/1.3540657, vol. 16, no. 2, p. 026011, Feb. 2011, doi: 10.1117/1.3540657.

[42] K. J. Zuzak, M. T. Gladwin, R. O. Cannon, and I. W. Levin, "Imaging hemoglobin oxygen saturation in sickle cell disease patients using noninvasive visible reflectance hyperspectral techniques: Effects of nitric oxide," *Am J Physiol Heart Circ Physiol*, vol. 285, no. 3 54-3, Sep. 2003, doi: 10.1152/AJPHEART.00243.2003/ASSET/IMAGES/LARGE/H40932538006.JPEG.

[43] Y. Tong *et al.*, "Hyperspectral Autofluorescence Imaging of Drusen and Retinal Pigment Epithelium in Donor Eyes with Age-Related Macular Degeneration," *Retina*, vol. 36, no. Suppl 1, p. S127, 2016, doi: 10.1097/IAE.0000000000001325.

[44] T. Ben Ami *et al.*, "Spatial and Spectral Characterization of Human Retinal Pigment Epithelium Fluorophore Families by Ex Vivo Hyperspectral Autofluorescence Imaging," *Transl Vis Sci Technol*, vol. 5, no. 3, pp. 5–5, May 2016, doi: 10.1167/TVST.5.3.5.

[45] B. Khoobehi *et al.*, "Using Hyperspectral Imaging to Investigate Oxygen Saturation in ONH Tissue in Primate's Eyes during the Development of Experimental Early Phase Glaucoma," *Invest Ophthalmol Vis Sci*, vol. 50, no. 13, pp. 5804–5804, Apr. 2009.

[46] L. Giannoni, F. Lange, and I. Tachtsidis, "Hyperspectral imaging solutions for brain tissue metabolic and hemodynamic monitoring: past, current and future developments," *Journal of Optics*, vol. 20, no. 4, p. 044009, Mar. 2018, doi: 10.1088/2040-8986/AAB3A6.

[47] S. D. Konecky *et al.*, "Hyperspectral optical tomography of intrinsic signals in the rat cortex," *https://doi.org/10.1117/1.NPh.2.4.045003*, vol. 2, no. 4, p. 045003, Nov. 2015, doi: 10.1117/1.NPH.2.4.045003.

[48] P. A. Valdés, F. Leblond, V. L. Jacobs, B. C. Wilson, K. D. Paulsen, and D. W. Roberts, "Quantitative, spectrally-resolved intraoperative fluorescence imaging," *Scientific Reports 2012 2:1*, vol. 2, no. 1, pp. 1–7, Nov. 2012, doi: 10.1038/srep00798.

[49] N. S. Samel and H. Mashimo, "Application of OCT in the Gastrointestinal Tract," *Applied Sciences 2019, Vol. 9, Page 2991*, vol. 9, no. 15, p. 2991, Jul. 2019, doi: 10.3390/APP9152991.

[50] S. S. More, J. M. Beach, and R. Vince, "Early Detection of Amyloidopathy in Alzheimer's Mice by Hyperspectral Endoscopy," *Invest Ophthalmol Vis Sci*, vol. 57, no. 7, pp. 3231–3238, Jun. 2016, doi: 10.1167/IOVS.15-17406.

[51] S. S. More, J. M. Beach, C. McClelland, A. Mokhtarzadeh, and R. Vince, "In Vivo Assessment of Retinal Biomarkers by Hyperspectral Imaging: Early Detection of Alzheimer's Disease," *ACS Chem Neurosci*, vol. 10, no. 11, pp. 4492–4501, Nov. 2019, doi: 10.1021/ACSCHEMNEURO.9B00331.

[52] S. S. More and R. Vince, "Hyperspectral Imaging Signatures Detect Amyloidopathy in Alzheimer's Mouse Retina Well before Onset of Cognitive Decline," *ACS Chem Neurosci*, vol. 6, no. 2, pp. 306–315, Feb. 2014, doi: 10.1021/CN500242Z.

[53] J. K. H. Lim *et al.*, "Retinal hyperspectral imaging in the 5xFAD mouse model of Alzheimer's disease," *Sci Rep*, vol. 11, no. 1, Dec. 2021, doi: 10.1038/S41598-021-85554-2.

[54] L. Moons and L. De Groef, "Multimodal retinal imaging to detect and understand Alzheimer's and Parkinson's disease," *Curr Opin Neurobiol*, vol. 72, pp. 1–7, Feb. 2022, doi: 10.1016/J.CONB.2021.07.007.

[55] M. Vandenabeele *et al.*, “The App NL-G-F mouse retina is a site for preclinical Alzheimer’s disease diagnosis and research,” *Acta Neuropathol Commun*, vol. 9, no. 1, pp. 1–16, Dec. 2021, doi: 10.1186/S40478-020-01102-5/FIGURES/5.

[56] S. Lemmens *et al.*, “Combination of snapshot hyperspectral retinal imaging and optical coherence tomography to identify Alzheimer’s disease patients,” *Alzheimers Res Ther*, vol. 12, no. 1, Dec. 2020, doi: 10.1186/S13195-020-00715-1.

[57] N. Mirzaei *et al.*, “Alzheimer’s Retinopathy: Seeing Disease in the Eyes,” *Front Neurosci*, vol. 14, Sep. 2020, doi: 10.3389/FNINS.2020.00921.

[58] L. Jin *et al.*, “Investigating the inhibitory effects of entacapone on amyloid fibril formation of human lysozyme,” *Int J Biol Macromol*, vol. 161, pp. 1393–1404, Oct. 2020, doi: 10.1016/J.IJBIOMAC.2020.07.296.

[59] K. Zhang, W. Zuo, L. Z.-I. T. on Image, and undefined 2018, “FFDNet: Toward a fast and flexible solution for CNN-based image denoising,” *ieeexplore.ieee.org*, Available: https://ieeexplore.ieee.org/abstract/document/8365806/

[60] M. Tassano, J. Delon, and T. Veit, “FastDVDNet: Towards real-time deep video denoising without flow estimation,” *Proceedings of the IEEE Computer Society Conference on Computer Vision and Pattern Recognition*, pp. 1351–1360, 2020.

[61] W. Hu, Y. Huang, L. Wei, F. Zhang, and H. Li, “Deep convolutional neural networks for hyperspectral image classification,” *J Sens*, vol. 2015, 2015, doi: 10.1155/2015/258619.

[62] Y. Chen, H. Jiang, C. Li, … X. J.-I. T. on, and undefined 2016, "Deep feature extraction and classification of hyperspectral images based on convolutional neural networks," *ieeexplore.ieee.org*, Available: https://ieeexplore.ieee.org/abstract/document/7514991/

[63] M. Halicek, J. V. Little, X. Wang, A. Y. Chen, and B. Fei, "Optical biopsy of head and neck cancer using hyperspectral imaging and convolutional neural networks," *J Biomed Opt*, vol. 24, no. 3, p. 1, Mar. 2019, doi: 10.1117/1.JBO.24.3.036007.

[64] M. Halicek *et al.*, "Hyperspectral Imaging of Head and Neck Squamous Cell Carcinoma for Cancer Margin Detection in Surgical Specimens from 102 Patients Using Deep Learning," *Cancers 2019, Vol. 11, Page 1367*, vol. 11, no. 9, p. 1367, Sep. 2019, doi: 10.3390/CANCERS11091367.

[65] H. Lee and H. Kwon, "Going Deeper with Contextual CNN for Hyperspectral Image Classification," *IEEE Transactions on Image Processing*, vol. 26, no. 10, pp. 4843–4855, Oct. 2017, doi: 10.1109/TIP.2017.2725580.

[66] B. Liu, X. Yu, P. Zhang, A. Yu, Q. Fu, and X. Wei, "Supervised deep feature extraction for hyperspectral image classification," *IEEE Transactions on Geoscience and Remote Sensing*, vol. 56, no. 4, pp. 1909–1921, Apr. 2018, doi: 10.1109/TGRS.2017.2769673.

[67] N. He *et al.*, "Feature extraction with multiscale covariance maps for hyperspectral image classification," *IEEE Transactions on Geoscience and Remote Sensing*, vol. 57, no. 2, pp. 755–769, Feb. 2019, doi: 10.1109/TGRS.2018.2860464.

[68] Z. Wang, A. C. Bovik, H. R. Sheikh, and E. P. Simoncelli, "Image quality assessment: From error visibility to structural similarity," *IEEE Transactions on Image Processing*, vol. 13, no. 4, pp. 600–612, Apr. 2004, doi: 10.1109/TIP.2003.819861.

[69] Y. Rivenson, T. Liu, Z. Wei, Y. Zhang, K. de Haan, and A. Ozcan, “PhaseStain: the digital staining of label-free quantitative phase microscopy images using deep learning,” *Light: Science & Applications 2019 8:1*, vol. 8, no. 1, pp. 1–11, Feb. 2019, doi: 10.1038/s41377-019-0129-y.

[70] P. Isola, J. Y. Zhu, T. Zhou, and A. A. Efros, “Image-to-image translation with conditional adversarial networks,” *Proceedings - 30th IEEE Conference on Computer Vision and Pattern Recognition, CVPR 2017*, vol. 2017-January, pp. 5967–5976, Nov. 2017, doi: 10.1109/CVPR.2017.632.

[71] J. C. Morris, “The Clinical Dementia Rating (CDR),” *Neurology*, vol. 43, no. 11, pp. 2412-2412-a, Nov. 1993, doi: 10.1212/WNL.43.11.2412-A.

[72] M. F. Folstein, S. E. Folstein, and P. R. McHugh, “‘Mini-mental state’. A practical method for grading the cognitive state of patients for the clinician,” *J Psychiatr Res*, vol. 12, no. 3, pp. 189–198, 1975, doi: 10.1016/0022-3956(75)90026-6.

[73] J. Popel, H. El-Hakim, and W. El-Matary, “Esophageal foreign body extraction in children: flexible versus rigid endoscopy,” *Surg Endosc*, vol. 25, no. 3, pp. 919–922, 2011, doi: 10.1007/S00464-010-1299-0.

[74] G. Unfried, F. Wieser, A. Albrecht, A. Kaider, and F. Nagele, “Flexible versus rigid endoscopes for outpatient hysteroscopy: a prospective randomized clinical trial,” *Hum Reprod*, vol. 16, no. 1, pp. 168–171, 2001, doi: 10.1093/HUMREP/16.1.168.

[75] C. C. Tseng, T. Y. Hsiao, and W. C. Hsu, “Comparison of rigid and flexible endoscopy for removing esophageal foreign bodies in an emergency,” *Journal of the Formosan Medical Association*, vol. 115, no. 8, pp. 639–644, Aug. 2016, doi: 10.1016/J.JFMA.2015.05.016.

[76] N. Roberts *et al.*, “Toward routine use of 3D histopathology as a research tool,” *Am J Pathol*, vol. 180, no. 5, pp. 1835–1842, May 2012, doi: 10.1016/J.AJPATH.2012.01.033.

[77] A. M. Blakely and T. J. Miner, “Surgical considerations in the treatment of gastric cancer,” *Gastroenterol Clin North Am*, vol. 42, no. 2, pp. 337–357, Jun. 2013, doi: 10.1016/J.GTC.2013.01.010.

[78] N. FUTAWATARI, S. KIKUCHI, S. SAKURAMOTO, M. KIDA, and M. WATANABE, “A New Diagnostic Method for Early Gastric Cancer: Volume Measurement by 3-Dimensional Endoscopic Ultrasonography in Early Gastric Cancer and Its Clinical Significance,” *Anticancer Res*, vol. 28, no. 5B, p. 2907, Sep. 2008, Available: http://ar.iiarjournals.org/content/28/5B/2907.abstract

[79] S. Kikuchi, N. Futawatari, M. Watanabe, M. Sasaki, K. Kubota, and M. Kida, “Gastrointestinal Tumors: Computed Tomography/Endoscopic Ultrasonography,” *Cancer Imaging*, pp. 407–411, Jan. 2008, doi: 10.1016/B978-012374212-4.50114-0.

[80] A. Orth, M. Ploschner, E. Wilson, I. Maksymov, and B. Gibson, “Optical fiber bundles: Ultra-slim light field imaging probes,” *Sci Adv*, vol. 5, p. eaav1555, Apr. 2019, doi: 10.1126/sciadv.aav1555.

[81] R. Ng, M. Levoy, M. Brédif, G. Duval, and M. Horowitz, “Light field photography with a hand-held plenoptic camera,” 2005.

[82] E. Y. Lam, “Computational photography with plenoptic camera and light field capture: tutorial,” *JOSA A, Vol. 32, Issue 11, pp. 2021-2032*, vol. 32, no. 11, pp. 2021–2032, Nov. 2015, doi: 10.1364/JOSAA.32.002021.

[83] I. Ihrke, J. Restrepo, and L. Mignard-Debise, “Principles of Light Field Imaging: Briefly revisiting 25 years of research,” *IEEE Signal Process Mag*, vol. 33, no. 5, pp. 59–69, Sep. 2016, doi: 10.1109/MSP.2016.2582220.

[84] A. Lumsdaine and T. Georgiev, “Full resolution lightfield rendering,” *Indiana University and Adobe Systems, Tech. Rep*, vol. 91, p. 92, 2008.

[85] L. Gao, K. Eaton, P. Jin, A. Lai, and S. Zhu, “On the fundamental comparison between unfocused and focused light field cameras,” *Applied Optics, Vol. 57, Issue 1, pp. A1-A11*, vol. 57, no. 1, pp. A1–A11, Jan. 2018, doi: 10.1364/AO.57.0000A1.

[86] A. Lumsdaine and T. Georgiev, “Full Resolution Lightfield Rendering.”

[87] N. J. Durr, G. González, and V. Parot, “3D imaging techniques for improved colonoscopy,” *Expert Rev Med Devices*, vol. 11, no. 2, pp. 105–107, Mar. 2014, doi: 10.1586/17434440.2013.868303.

[88] V. Parot *et al.*, “Photometric stereo endoscopy,” *J Biomed Opt*, vol. 18, no. 7, p. 076017, Jul. 2013, doi: 10.1117/1.JBO.18.7.076017.

[89] N. J. Durr *et al.*, “Mo1499 Imaging Colonic Surface Topography With Photometric Stereo Endoscopy,” *Gastrointest Endosc*, vol. 79, no. 5, p. AB459, May 2014, doi: 10.1016/j.gie.2014.02.676.

[90] N. T. Clancy, G.-Z. Yang, L. Maier-Hein, A. Groch, D. S. Elson, and D. Stoyanov, “Spectrally encoded fiber-based structured lighting probe for intraoperative 3D imaging,” *Biomedical Optics Express, Vol. 2, Issue 11, pp. 3119-3128*, vol. 2, no. 11, pp. 3119–3128, Nov. 2011, doi: 10.1364/BOE.2.003119.

[91] J. Lin, N. T. Clancy, D. Stoyanov, and D. S. Elson, “Tissue Surface Reconstruction Aided by Local Normal Information Using a Self-calibrated Endoscopic Structured Light System,” *Lecture Notes in Computer Science (including subseries Lecture Notes in Artificial Intelligence and Lecture Notes in Bioinformatics)*, vol. 9349, pp. 405–412, 2015, doi: 10.1007/978-3-319-24553-9_50.

[92] M. J. Gora, M. J. Suter, G. J. Tearney, and X. Li, “Endoscopic optical coherence tomography: technologies and clinical applications [Invited],” *Biomed Opt Express*, vol. 8, no. 5, p. 2405, May 2017, doi: 10.1364/BOE.8.002405.

[93] E. Y. Lam, “Computational photography with plenoptic camera and light field capture: tutorial,” *JOSA A, Vol. 32, Issue 11, pp. 2021-2032*, vol. 32, no. 11, pp. 2021–2032, Nov. 2015, doi: 10.1364/JOSAA.32.002021.

[94] C. Perwass and L. Wietzke, “Single lens 3D-camera with extended depth-of-field,” *https://doi.org/10.1117/12.909882*, vol. 8291, pp. 45–59, Feb. 2012, doi: 10.1117/12.909882.

[95] A. M. Zysk, F. T. Nguyen, A. L. Oldenburg, D. L. Marks, and S. A. B. M. D, “Optical coherence tomography: a review of clinical development from bench to bedside,” *J Biomed Opt*, vol. 12, no. 5, p. 051403, Sep. 2007, doi: 10.1117/1.2793736.

[96] D. Seong *et al.*, “Virtual intraoperative optical coherence tomography angiography integrated surgical microscope for simultaneous imaging of morphological structures and vascular maps in vivo,” *Opt Lasers Eng*, vol. 151, p. 106943, Apr. 2022, doi: 10.1016/J.OPTLASENG.2021.106943.

[97] J. G. Fujimoto, C. Pitris, S. A. Boppart, and M. E. Brezinski, “Optical Coherence Tomography: An Emerging Technology for Biomedical Imaging and Optical Biopsy,” *Neoplasia*, vol. 2, no. 1–2, pp. 9–25, Jan. 2000, doi: 10.1038/SJ.NEO.7900071.

[98] L. P. Hariri *et al.*, “Endobronchial Optical Coherence Tomography for Low-Risk Microscopic Assessment and Diagnosis of Idiopathic Pulmonary Fibrosis In Vivo,” *Am J Respir Crit Care Med*, vol. 197, no. 7, pp. 949–952, Sep. 2017, doi: 10.1164/rccm.201707-1446LE.

[99] G. L. Monroy, J. Won, D. R. S. Jr., R. Dsouza, and S. A. Boppart, “Clinical translation of handheld optical coherence tomography: practical considerations and recent advancements,” *J Biomed Opt*, vol. 22, no. 12, p. 121715, Dec. 2017, doi: 10.1117/1.JBO.22.12.121715.

[100] J. Lee *et al.*, “Identification of multi-dimensional thread geometry using depth-resolved swept-source optical coherence tomography for assessment of dental implant fabrication,” *Opt Lasers Eng*, vol. 127, p. 105951, 2020, doi: https://doi.org/10.1016/j.optlaseng.2019.105951.

[101] J. Moon, Y.-S. Lim, S. Yoon, and W. Choi, “Single-shot multi-depth full-field optical coherence tomography using spatial frequency division multiplexing,” *Opt Express*, vol. 29, no. 5, pp. 7060–7069, 2021, doi: 10.1364/OE.417950.

[102] S. Witte, M. Baclayon, E. J. G. Peterman, R. F. G. Toonen, H. D. Mansvelder, and M. L. Groot, “Single-shot two-dimensional full-range optical coherence tomography achieved by dispersion control,” *Opt Express*, vol. 17, no. 14, pp. 11335–11349, 2009, doi: 10.1364/OE.17.011335.

[103] R. F. Spaide, J. G. Fujimoto, and N. K. Waheed, “IMAGE ARTIFACTS IN OPTICAL COHERENCE TOMOGRAPHY ANGIOGRAPHY,” *RETINA*, vol. 35, no. 11, 2015.

[104] J. Park, X. Feng, R. Liang, and L. Gao, “Snapshot multidimensional photography through active optical mapping,” *Nature Communications 2020 11:1*, vol. 11, no. 1, pp. 1–13, Nov. 2020, doi: 10.1038/s41467-020-19418-0.

[105] T.-U. Nguyen, M. C. Pierce, L. Higgins, and T. S. Tkaczyk, “Snapshot 3D optical coherence tomography system using image mapping spectrometry,” *Opt Express*, vol. 21, no. 11, pp. 13758–13772, 2013, doi: 10.1364/OE.21.013758.

[106] J. F. de Boer, B. Cense, B. H. Park, M. C. Pierce, G. J. Tearney, and B. E. Bouma, “Improved signal-to-noise ratio in spectral-domain compared with time-domain optical coherence tomography,” *Opt Lett*, vol. 28, no. 21, p. 2067, Nov. 2003, doi: 10.1364/OL.28.002067.

[107] M. Choma, M. Sarunic, C. Yang, and J. Izatt, “Sensitivity advantage of swept source and Fourier domain optical coherence tomography,” *Opt Express*, vol. 11, no. 18, p. 2183, Sep. 2003, doi: 10.1364/OE.11.002183.

[108] R. Leitgeb, C. Hitzenberger, and A. Fercher, “Performance of fourier domain vs. time domain optical coherence tomography,” *Opt Express*, vol. 11, no. 8, p. 889, Apr. 2003, doi: 10.1364/OE.11.000889.

[109] R. R. Iyer, M. Žurauskas, Q. Cui, L. Gao, R. Theodore Smith, and S. A. Boppart, “Full-field spectral-domain optical interferometry for snapshot three-dimensional microscopy,” *Biomed Opt Express*, vol. 11, no. 10, pp. 5903–5919, 2020, doi: 10.1364/BOE.402796.

[110] Q. Cui, J. Park, R. Theodore Smith, and L. Gao, "Snapshot hyperspectral light field imaging using image mapping spectrometry," *Opt Lett*, vol. 45, no. 3, pp. 772–775, 2020, doi: 10.1364/OL.382088.

[111] Q. Cui *et al.*, "Development of a fast calibration method for image mapping spectrometry," *Appl Opt*, vol. 59, no. 20, pp. 6062–6069, 2020, doi: 10.1364/AO.395988.

[112] J. T. W. Yeow *et al.*, "Micromachined 2-D scanner for 3-D optical coherence tomography," *Sens Actuators A Phys*, vol. 117, no. 2, pp. 331–340, 2005, doi: https://doi.org/10.1016/j.sna.2004.06.021.

[113] Q. Hao, Y. Ning, Y. Hu, Y. Zhang, X. Tao, and X. Chang, "Simultaneous phase-shifting interferometer with a monitored spatial light modulator flexible reference mirror," *Appl Opt*, vol. 60, no. 6, pp. 1550–1557, 2021, doi: 10.1364/AO.414810.

[114] F. Schmieder, L. Büttner, and J. Czarske, "Adaptive laser-induced ultrasound generation using a micro-mirror array spatial light modulator," *Opt Express*, vol. 24, no. 20, pp. 22536–22543, 2016, doi: 10.1364/OE.24.022536.

[115] T. Lei *et al.*, "A high-resolution optically addressed spatial light modulator based on ZnO nanoparticles," *Light: Science & Applications 2015 4:3*, vol. 4, no. 3, pp. e259–e259, Mar. 2015, doi: 10.1038/lsa.2015.32.

[116] S.-Q. Li, X. Xu, R. Maruthiyodan Veetil, V. Valuckas, R. Paniagua-Domínguez, and A. I. Kuznetsov, "Phase-only transmissive spatial light modulator based on tunable dielectric metasurface," *Science (1979)*, vol. 364, no. 6445, pp. 1087–1090, Jun. 2019, doi: 10.1126/science.aaw6747.

[117] Y.-H. Kim *et al.*, “Development of high-resolution active matrix spatial light modulator,” *Optical Engineering*, vol. 57, no. 6, p. 061606, Feb. 2018, doi: 10.1117/1.OE.57.6.061606.

[118] L. Gao, R. T. Kester, and T. S. Tkaczyk, “Compact Image Slicing Spectrometer (ISS) for hyperspectral fluorescence microscopy,” *Opt Express*, vol. 17, no. 15, pp. 12293–12308, 2009, doi: 10.1364/OE.17.012293.

[119] J. F. de Boer, C. E. Saxer, and J. S. Nelson, “Stable carrier generation and phase-resolved digital data processing in optical coherence tomography,” *Appl Opt*, vol. 40, no. 31, pp. 5787–5790, 2001, doi: 10.1364/AO.40.005787.

[120] X. Shu, L. J. Beckmann, and H. F. Zhang, “Visible-light optical coherence tomography: a review,” *J Biomed Opt*, vol. 22, no. 12, p. 121707, Dec. 2017, doi: 10.1117/1.JBO.22.12.121707.

[121] J. Ke and E. Y. Lam, “Image reconstruction from nonuniformly spaced samples in spectral-domain optical coherence tomography,” *Biomed Opt Express*, vol. 3, no. 4, pp. 741–752, 2012, doi: 10.1364/BOE.3.000741.

[122] K. Wang *et al.*, “Development of a non-uniform discrete Fourier transform based high speed spectral domain optical coherence tomography system,” *Opt Express*, vol. 17, no. 14, pp. 12121–12131, 2009, doi: 10.1364/OE.17.012121.

[123] J. Luisi *et al.*, “Longitudinal Assessment of Alkali Injury on Mouse Cornea Using Anterior Segment Optical Coherence Tomography,” *Transl Vis Sci Technol*, vol. 10, no. 3, pp. 6–6, Mar. 2021, doi: 10.1167/TVST.10.3.6.

[124] J. Park *et al.*, "Biocompatibility evaluation of bioprinted decellularized collagen sheet implanted in vivo cornea using swept-source optical coherence tomography," *J Biophotonics*, vol. 12, no. 11, p. e201900098, Nov. 2019, doi: 10.1002/JBIO.201900098.

[125] P. Eugui *et al.*, "Three-dimensional visualization of opacifications in the murine crystalline lens by in vivo optical coherence tomography," *Biomed Opt Express*, vol. 11, no. 4, pp. 2085–2097, 2020, doi: 10.1364/BOE.387335.

[126] X. Du *et al.*, "Hyperspectral retinal imaging in Alzheimer's disease and age-related macular degeneration: a review," *Acta Neuropathol Commun*, vol. 12, no. 1, p. 157, 2024, doi: 10.1186/s40478-024-01868-y.

[127] X. Du *et al.*, "Label-free hyperspectral imaging and deep-learning prediction of retinal amyloid β-protein and phosphorylated tau," *PNAS Nexus*, vol. 1, no. 4, p. pgac164, Sep. 2022, doi: 10.1093/pnasnexus/pgac164.

[128] J. Lee *et al.*, "Tunable image-mapping optical coherence tomography," *Biomed Opt Express*, vol. 14, no. 2, pp. 627–638, 2023, doi: 10.1364/BOE.477646.

[129] X. Du, S. Zhu, and L. Gao, "Super-Resolution Fiber-Bundle Light Field Endoscopy," *Biophotonics Congress 2021 (2021), paper DTh1A.3*, p. DTh1A.3, Apr. 2021, doi: 10.1364/BODA.2021.DTH1A.3.